NOVEL CORE TECHNOLOGIES AND SYSTEMS FOR MAGNETIC RESONANCE COMPATIBLE ROBOTICS

A Dissertation

Presented to
the Faculty of the Department of Electrical and Computer Engineering
University of Houston

In Partial Fulfillment
of the requirements for the Degree
Doctor of Philosophy
in Electrical Engineering

by
Nicholas von Sternberg
December 2013

NOVEL CORE TECHNOLOGIES AND SYSTEMS FOR MAGNETIC RESONANCE COMPATIBLE ROBOTICS

_____

Nicholas von Sternberg

Approved:

_____

Chair of the Committee
Haluk Ogmen, Professor,
Electrical and Computer Engineering

_____

Co-Chair of the Committee
Nikolaos V. Tsekos, Associate Professor,
Computer Science

Committee Members:

_____

Jose L. Contreras-Vidal, Professor,
Electrical and Computer Engineering

_____

Yuhua Chen, Associate Professor,
Electrical and Computer Engineering

_____

R. Jason Stafford, Associate Professor,
Imaging Physics,
UT MD Anderson Cancer Center

_____

Suresh K. Khator, Associate Dean,
Cullen College of Engineering

_____

Badri Roysam, Professor and Chair,
Electrical and Computer Engineering

Acknowledgments

The majority of this work was supported by the National Science Foundation under Grant CNS-0932272. All opinions, findings, conclusions or recommendations expressed in this work are those of the authors and do not necessarily reflect the views of our sponsors.

I am grateful to Professor Nikolaos V. Tsekos for encouraging me to pursue academic research and for providing me with the resources and guidance I needed to complete this research. I would also like to thank Professor Haluk Ogmen for serving as my committee chair and advisor during my PhD studies in the electrical engineering department. As an exchange student, a portion of my studies were completed at National Tsing Hua University in Taiwan. I want to thank Professor Pei and Vice President Wang for creating this opportunity, and I will always be grateful to Professor Yeh and the students of the LDSC for treating me as family. Many thanks to the past and present students of the Medical Robotics Lab for their support, shared wisdom, and most of all, patience. I especially want to thank Yousef Hedayati and Eric Draper for their help during the design and construction of the motion phantom, and Habib Zaid for going above and beyond to assist me during the construction and execution of these experiments as part of his undergraduate research. Most of all I want to thank my family and close friends for their support and understanding during these trying times.

NOVEL CORE TECHNOLOGIES AND SYSTEMS FOR MAGNETIC RESONANCE COMPATIBLE ROBOTICS

An Abstract
of a
Dissertation

Presented to
the Faculty of the Department of Electrical and Computer Engineering
University of Houston

In Partial Fulfillment
of the requirements for the Degree
Doctor of Philosophy
in Electrical Engineering

by
Nicholas von Sternberg
December 2013

Abstract

This dissertation presents design and validation of several systems and technologies for magnetic resonance imaging (MRI) compatible positioning. The research began as the development of an MRI compatible actuated phantom, which required precise motion through remote actuation. The phantom, which operates from 18 remotely actuated stepper motors, provided motion inside the MRI scanner with submilimeter accuracy and minimal zipper artifacts induced to the images. The motion requirements lead of the phantom project led to the development of a closed-loop motor controller which enabled such accuracy. Maximum absolute error of the tracking a sigmoid function was 0.012 rad, four times the precision of the motor itself. Through the process of developing the actuated phantom, ideas for a flexible, intrinsically MRI compatible method of force transmission were transformed into the Solid Media Flexible Transmission (SMFT) technology presented which can provide force transmission to an end effector up to 4 meters away from the remote actuator without the use of electrically conductive or magnetically susceptible materials. A tool positioning robot was built to demonstrate the technology and SNR reduction of as little as 5% was achieved by filtering the motor drive signals. The methods and experiments provided within demonstrate that traditional electromagnetic motors can be used inside the MRI room with better kinematic results than pneumatic or hydraulic systems and higher force output than piezoelectric motors with the use of the novel SMFT force transmission method.

Table of Contents

List of Figures

List of Tables

1. Introduction

1.1 Overview

The purpose of this work is to present the research and validation of several enabling technologies for magnetic resonance imaging (MRI) compatible positioning. This research is necessary to address current limitations which prevent MRI guided robotic surgery from being a standard of clinical practice. The field of MRI compatible robotics is a direct result of the evolution of minimally invasive surgery (MIS), Robotic Assisted Surgery (RAS), MRI, and MRI guided interventions which are each reviewed in Chapter 1. MRI compatible robots are an enabling technology for MRI guided interventions which face many operational constraints which are analyzed in the first section of Chapter 2, followed by a survey of notable prior work relevant to the contributions presented in this dissertation, including MRI compatible actuation, MRI Compatible Surgical Robots, and the control of electric stepper motors. The first contribution of this research is the design and validation of an MRI compatible motion phantom presented in Chapter 3. Design and implementation of a high performance stepper motor controller, which provides the motion control for each of these contributions requiring motors, is presented in Chapter 4. The most notable contribution of this work is the development and validation of a novel method of linear force transmission presented in Chapter 5. An MRI compatible positioning robot, which has been developed using this new method of force transmission, is presented in Chapter 6 and detailed methods and experiments for MR image compatibility, including shielding and filtering of signals, are presented in Chapter 7. Final conclusions are presented in Chapter 8.

1.2 Minimally Invasive Surgery (MIS)

Minimally invasive surgery (MIS) is surgery performed through small incisions or orifices in the body to reduce the negative effects prevalent to traditional "open" surgery which required very large incisions exposing the internal anatomy. As early as 1987 publications demonstrated that by reducing the "damage that surgeons have inflicted in achieving their technical aim" recovery time can be reduced from weeks to hours [1]. Potential benefits of MIS are a decrease of all of the following: blood loss, postoperative pain, postoperative complication, surgical time, and length of hospital stay. Outcomes include reduced patient discomfort, faster healing time, reduced scarring, and decreased risk of infection or other complications [1-3].

To harness the benefits of MIS, however, certain challenges must be overcome. MIS requires special tools, procedures and training. Crucial drawbacks to MIS include the reduction of the surgeon's sensory perception and manipulation capabilities during the operation [4]. Tactile sensation is greatly inhibited by the instruments required for MIS because of the high force required to manipulate them. Most traditional laparoscopic interventions are performed using a small endoscope camera. Endoscopes provide only a "keyhole" two-dimensional appreciation of the area of operation and only partially compensate the loss of natural 3D vision [5]. MIS may also be performed using medical imaging guidance such as X-Ray Fluroscopy, CT, MRI, ultrasound or other modalities each with their own specific benefits and limitations [6]. Such surgeries are referred to as image guided interventions (IGI).

1.3 Robot Assisted Surgery

Robotic systems can be useful in assisting surgeons during interventions to provide a better surgical outcome. Though robots are inherently autonomous machines, surgical robots are currently being developed to automate certain tasks associated with surgery, not to automate the entire surgical procedure. Many commercially available systems already exist, 12 of which were reviewed by Ponnusamy et al. in 2011 [7]. These robotic systems manifest varying configurations, capabilities, and levels of autonomy. All currently available commercial robotic systems still require a surgeon for the procedure and those procedures with the highest risk or invasiveness actually have the least autonomy [8].

Some commercial systems such as the Da Vinci robot (Inuitive Surgical, Inc.), or Sensei Catheter System (Hansen Medical, Inc.) aim to make minimally invasive surgical operations more intuitive for surgeons by providing ergonomic controls and a 3d visualization interface without providing any automated positioning. Other image guided systems such as ROBODOC (Curexo Technology) [9] or Neuroarm [10] aim to increase accuracy by using precisely controlled motion planned from images collected from modalities such as CT or MRI. Sometimes haptic devices such as Omega.Medical (Force Dimension) are combined with surgical robots to provide tactile and force-feedback for increased sensory perception during MIS and robotic interventions. Clinicians [11-13] indicate that robotic surgery can provide better patient outcomes including reduced blood loss, decreased pain, and shorter hospital stay as well as benefits to the surgeon through ergonomics to reduce fatigue and enhanced visual perception. Also mentioned were greater abilities through enhanced precision and dexterity such as the increased ability to

tie knots and sutures and to perform more complex procedures even in small work environments. The clinical success of standard RAS systems demonstrates the potential success of the more sophisticated image guided RAS systems to come.

1.4 Magnetic Resonance Imaging (MRI)

Magnetic resonance imaging (MRI) is a tomographic imaging technique used to visualize internal structure in the body using magnetic resonance. The MRI image is obtained as follows [14]: The area of interest to be imaged is placed in a large static magnetic field. Atomic nuclei which hare sensitive to magnetic field (most commonly hydrogen) within the area will be aligned to the magnetic orientation of the static field to form equilibrium. Radiofrequency pulses are then used to create an oscillating field orthogonal to the static field which will temporarily excite the nuclei out of orientation. An electromagnetic signal, which is induced in a receiver coil as the nuclei return to equilibrium, can used through transformation algorithms to generate the image from the magnetic relaxation properties of the area of interest.

There are numerous imaging modalities currently be used for IGI. However, due to its unique image acquisition process, MRI provides information unavailable through other modalities. MRI characterizes tissues by their physical and biochemical content which provides excellent tissue contrast and even for tissues surrounded by bone. The design of MRI machines allows any image projection to be obtained without moving the patient. MRI is intriniscally multi-planar and multi-slice which allows for straightforward 2D, 3D, and even 4D reconstruction. MRI is the only emission topography modality which does not require radioactive injection for contrast [15] and unlike X-Ray and CT, MRI does not induce ionizing radiation because the signals used for MRI come directly

from the physical properties of the scanned object itself. These benefits make MRI the ideal imaging modality for IGI once we can overcome its technical disadvantages.

One major technical disadvantage of MRI is the slow image acquisition speed. Slow image acquisition can enable motion artifacts due to motion of the patient or even physiological motion. The magnetic relaxation properties of the tissue is a physical phenomenon which cannot be changed, however, RF pulse sequences are developed which can exploit the phenomena and increase scan time depending on the imaging information which is needed. For instance a T1 weighted MRI scan requires the longitudinal magnetization of the nuclei to return to 63.2% of equilibrium which takes between 250 to 2,500 ms for tissues in the body. Likewise, a T2 weighted scan requires transverse magnetization to return to 36.7% of equilibrium and requires between 25 to 250 ms. CINE is a pulse sequence used in real-time MRI to coordinate scans to evenly spaced frames of the cardiac cycle. Each image acquisition takes approximately 50 ms. Research will continue to improve the acquisition time of MRI in the years to come. The other technical disadvantages of MRI are the MRI environment itself. High magnetic fields of the MRI and space constraints prevent interventions to be performed inside the MRI using standard tools and equipment. These obstacles can be overcome with the use of special MRI compatible robotics which are the main research area of this work.

1.5 MRI guided Interventions

Magnetic resonance imaging (MRI) is a promising modality for image guided interventions (IGI) for many reasons not limited to its broad applicability, noninvasive nature, and ionizing-radiation-free operation [16]. The soft-tissue contrast of MRI, which is excellent in comparison to computer tomography (CT), X-ray, fluoroscopy and

ultrasound, is useful for diagnosis, guided therapy, and intervention. Multislice 3D imaging provides better visualization of the anatomy and can be used for planning interventions. Sufficient temporal and spatial contrast resolution, multiplanar scan plane, as well as temperature and flow sensitivity are consistent with the requirements of image guidance [17]. Modern systems allow for "on-the-fly" adjustment of imaging planes and volumes; such technology can be used to dynamically follow the intervention [18]. Since MRI imaging acquires data through the use of magnetic fields instead of ionizing radiation medical staff and patients do not have to worry about exposure as they do in the case of X-ray, CT, and fluoroscopy. These benefits along with the advancement of fast pulse sequences which allow quicker image acquisition make MRI an ideal modality for IGI. Several groups [11, 19-23] have documented the benefits of using MRI image guidance for a broad range of interventions including: cardiac, neuro, abdominal, prostate and breast interventions and gene therapy, but all of these interventions required the use of special MRI compatible tools and instruments due to the constraints of the MRI environment.

Although MRI has many benefits to offer, there are several challenges to be addressed before MRI can be used as a standard modality for interventions, most of which are intrinsic to the operation environment of MRI. MRI operation requires high strength magnetic fields which impose significant constraints on the instrumentation used in an MRI room. The MRI scanner itself imposes significant geometric constraints on the operating area as the patient must be placed within the cylindrical bore during imaging. These issues are critical impediments to using MRI for IGI. Robotic telemanipulation systems can be used not only to overcome the compatibility and space constraints of the

MRI environment, but also provide additional benefits such as accuracy and dexterity. Advanced systems can perform motion planning or real-time tracking using real-time MRI data.

2. Background and Literature Review

2.1. Constraints of the MR Environment

2.1.1 Patient Accessibility

Although patient accessibility depends on the scanner being used, it is limited for all MRI scanners due to the large magnets required for imaging. Traditional closed-bore MRI scanners (Figure 2.2.1.1) encompass the patient with a 60 cm or 70 cm diameter bore which prevents any open access to a patient except at either end. Since the imaging center is at the center of the bore, and a typical bore is 1.2 m to 2 m in length, most of the patient is inaccessible to a surgeon.

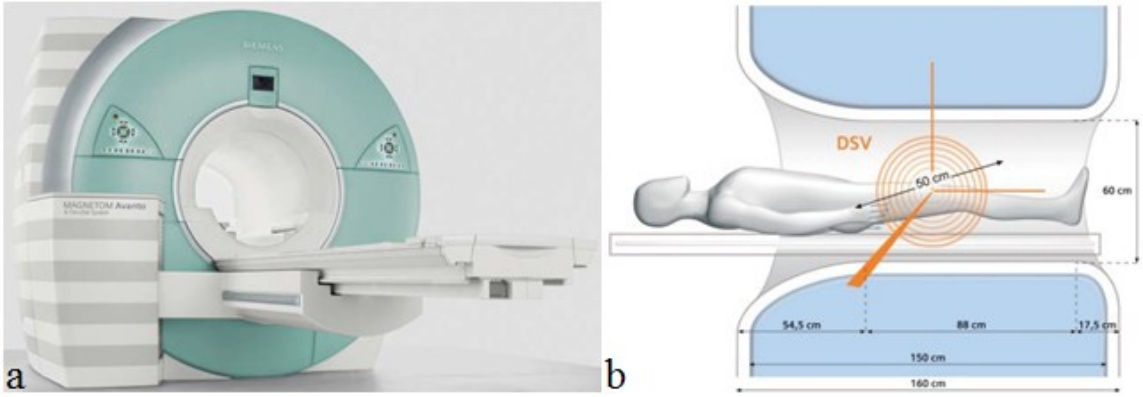

Figure 2.1.1.1 a) Traditional closed bore MRI machine and b) Closed-bore MRI cross-sectional dimensions. Source: Siemens MAGNETOM Avanto Catalog.

To increase access to patients during intervention, some Interventional MRI (IMRI) and low-field open-bore MRI systems have been developed which feature a "clamshell" or "double-donut" layout allowing open access to the patient from at least one direction. Most open-bore MRI systems have lower field strength such as the Panorama 1.0 T open MR (Phillips Medical Systems), or the UPRIGHT® Multi–Position™ 0.6 T open MRI (FONAR). However, closed-bore MRI scanners have better

field homogeneity, higher SNR, and faster image acquisition speed [24]. Typical field strengths of closed bore scanners are 1.5 T or 3.0 T. Typical field strength can be expected to increase in the future since higher field strengths between 4.0 T to 9.4 T are being evaluated in research [25]. Open-bore scanners do not provide the same quality of images and are just unacceptable for many interventions [26].To take advantage of the high contrast benefits of MRI we need to develop methods of performing interventions in closed-bore scanners with field strength of 1.5 T or greater.

2.1.2 MRI Compatibility

Though the benefits of using MRI for IGI are numerous, MRI compatibility is a significant limiting factor in equipment selection for an intervention. MRI compatibility of a robotic system is not clearly defined by any standard, but used throughout literature to designate robots which are capable of working within an MR environment [27]. Three main factors considered in MRI compatibility of a robotic system are safety, preserving image quality, and maintaining device functionality. As a result of high intensity static magnetic fields, rapidly changing magnetic field gradients, and radiofrequency sensitivity, most commonly used equipment and mechatronic systems are not suitable for MRI applications [18]. Although MRI is described as safe because it does not emit ionizing radiation, there are other intrinsic hazards present in the MR environment from the use of certain materials. Additionally image quality is sensitive to interference from materials or electromagnetic frequencies present in the MRI room. MRI compatibility is therefore a design optimization process to fully harness the benefits of MRI while protecting the patients, operators, and equipment in the MRI room.

Safety of a material in the MRI room mainly depends on the material's magnetic susceptibility and electrical conductance. Magnetically susceptible materials can be attracted to the very strong magnetic fields in the MRI room. Active shielding of an MRI scanner produces high spatial gradients near the scanner which could enable a sudden and strong attraction, known as the missile effect, to a magnetically attracted material [28]. Such an event could be very hazardous to a human caught between the object and the scanner, or damage equipment. Electrically conductive materials within the MRI's magnetic fields will induce a current from magnetic flux caused by either the switching field gradients, or movement of the material within the static field. Heat generated as a result of the induced eddy currents could potentially burn a human or cause thermal damage equipment. There are numerous documented cases of mishaps in the MRI environment that have resulted in injury and in some cases death [29]. For these reasons the safety of any piece of equipment entering the MRI room must be carefully analyzed.

Image distortion or artifacts reduces the effective benefit of MRI, and in the case of IGI could interfere with the accuracy or safety of the intervention. Since the MRI scanner uses RF pulses to gather imaging data, the imaging process is very susceptible to electromagnetic interference (EMI) from devices inside the MRI room. Conductive materials, even those which do not normally emit EMI, can still cause imaging artifacts via the generation of eddy currents [30]. For these reasons ideal materials for use in the MRI are magnetically inert and non-conductive. All equipment which will be used in an MRI room should undergo stringent compatibility testing to check for image distortion.

Consideration must also be made towards how the MR environment could affect the device itself. For instance certain devices which require magnetic force for operation

such as DC motors might not operate correctly in the high static magnetic field of the MRI. Reliability of components may be reduced by the exposure to magnetic fields. Electrical or electronic components could be permanently damaged or behave unexpectedly as a result of induced currents from changing field gradients. Sensor readings could be made inaccurate by EMI if the sensor or its wiring is sensitive to interference. The overall result of eddy currents or EMI induced to a mechatronic system may be temporary or premature failure, reduced lifetime, or undesired and possibly dangerous system response.

2.2 MRI Compatible Actuation

Due to the constraints outlined in the previous section, effective MRI compatible actuation is the primary impediment to the development of MRI-compatible robots. Several characteristics of an MRI compatible actuator must be considered including: magnetic properties, electrical properties, accuracy, and controllability. Gassert et al. [28] have originally categorized MR-compatible actuators into three suitable categories in order of MR compatibility: intrinsically MR-compatible, electric actuators, and electromagnetic actuators. Presented below is a review of all of the actuation methods used today organized by these three categories.

2.2.1 Intrinsically MR-compatible Actuators

Intrinsically MR-compatible actuation includes methods of actuation which do not introduce magnetically susceptible or electrically conductive materials into the MRI room. Examples include remote actuation methods which do not pass electrical signals into the MRI room such as fluidic actuations (hydraulic, pneumatic hydrostatic) and mechanical transmission systems (Bowden cables, driveshafts).

Fluidic actuators are attractive solutions to MR-compatible actuation because of the following characteristics: The fluids and end effectors can all be constructed of magnetically inert material, power can be transmitted from outside of the MRI room, actuators can provide sufficient force and range with a high force-to-mass ratio, and the transmission can be made flexible to adapt to the work environment [31]. Major drawbacks of fluidic transmission include a lack of stiffness, difficult control, and leaking. Fischer et al. [32] reported that the use of cylinder brakes to create stiffness during needle insertion. They also reported that the use of an MRI compatible controller and high-speed valves allowed shorter hose lengths so that the system was more easily controlled. However, the major drawback to fluidic systems is that the compressible fluids used to actuate them require non-linear control and a rigid and discrete form of actuation is preferred by most groups.

Two groups have developed methods of discrete motion using pneumatics. The resulting actuation is similar to that of a stepper motor but it uses using pneumatic for actuation instead of electromagnetics. These systems retain the intrinsic MRI compatibility of pneumatic systems, while eliminating some of the problems associated with non-linear pneumatic control and inability to hold position. Zemiti et al. [33] presented a sprocket wheel (Figure 2.2.2.1a) which is stepped forward and backward by two reciprocating pneumatic pistons. This method of actuation allows for discrete movements to be performed with very basic pneumatic control and provide good open loop accuracy. This basic system is capable of performing three impulses per second with a step size which is dependent on the sprocket used. A more sophisticated approach presented by Stoianovici et al. [34] is the PneuStep (Figure 2.2.2.1b) pneumatic stepper

motor. The motor actuation, which is controlled by three inlet air ports, has a maximum velocity of 300 steps/s or 16 mm/s. These motors are well suited for low speed precise positioning applications. However, a high-speed method of discrete pneumatic motion has not been demonstrated at this time.

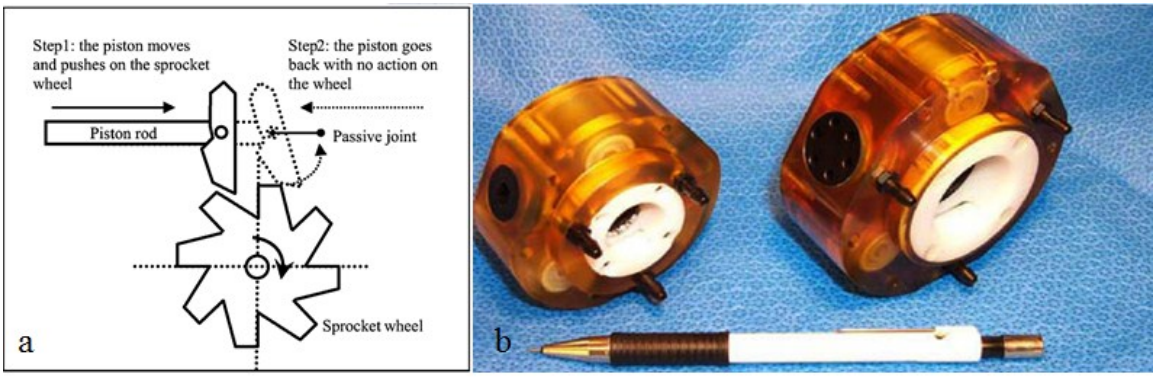

Figure 2.2.1.1 a) Sprocket wheel used for discrete pneumatic control. b) PneuStep pneumatic stepper motors.

2.2.2 Electric Actuators

Electric actuators do not contain ferromagnetic components therefore they are not in danger of being attracted to the MRI machine. These actuators are not intrinsically compatible, however, because they have electrically conductive materials which could induce eddy currents and potentially heating. Electric actuators may cause EMI either from the signals the carry, or signals they induce. Though they pose potential hazards, electric actuators are used in most MRI compatible robotic systems today because of their superior kinematic properties.

The most commonly used electric actuators are piezoelectric (ultrasonic) motors such as those manufactured by Shensei, Nanomotion, Squiggle, and Piezomotor. The motors are commercially available in a variety of configurations including rotary motion from two disks, linear motion from two plates, and rotary and linear combined motion

from vibrating a screw. Motion is the result of ultrasonic vibration of two piezoelectric surfaces so they may be also referred to as ultrasonic motors. The piezoelectric surfaces are manufactured in an interference fit so they offer inherent braking by design which is a feature for system rigidity. Inherent braking however also poses a safety risk in the case of power outages or machine failure, because the system cannot be moved by hand. Ultrasonic frequencies can cause motion which is predictable and repeatable and as well as incredibly precise. Piezoelectric motors offer many benefits including commercial availability, nanometer resolution, powerless braking, and long lifetime [35]. However, since they are not intrinsically compatible, several groups have reported noise as high as 40% to 60% [36-38] and artifacts [39] from operating these motors during MRI scanning. An example of this noise is shown in Figure 2.2.2.1 [36] below in which two piezoelectric motors, the Nanomotion, and Shinsei motors are compared to a pneumatic cylinder and a baseline by short-axis MRI scans of a bottle phantom.

Groups have attempted to reduce the SNR reduction in various ways. Tsekos et al. [16] have located the motors away from the MRI and used methods of remote actuation. Though noise was reduced, additional cost and performance reduction due to flexibility, backlash, or friction was noted. Goldenberg et al. [40] disabled the motors temporarily while scanning to avoid the interference, but this solution would not be suitable for situations which require continuous motion such as real-time tracking. Fischer et al. [41] proposed that the SNR degradation resulting from ultrasonic motors is actually induced from high frequency noise present in the motor drivers and is not a result of the ultrasonic

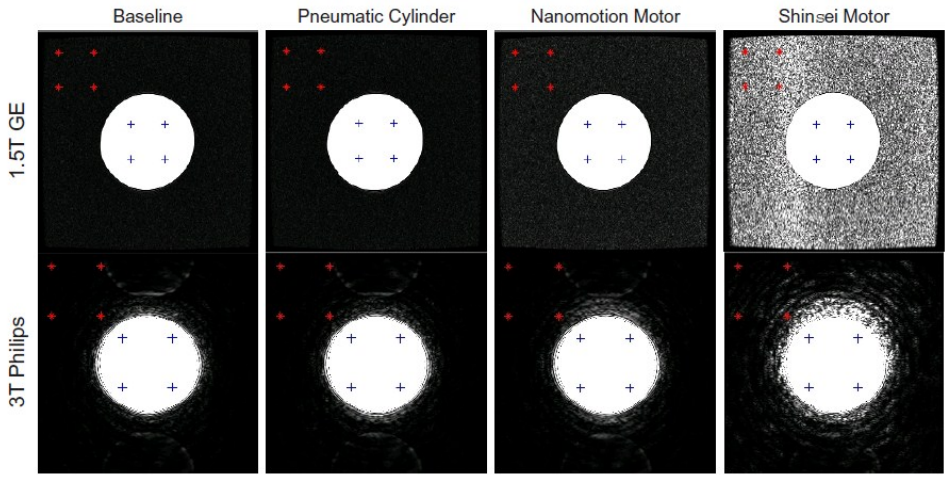

Figure 2.2.2.1. Comparison of MRI images acquired of a bottle phantom to compare noise induced by pneumatic actuation, a Nanomotion USM, and a Shensei USM.

frequency present in the motor itself. They created a filtered in-room piezoelectric motor driver which reduced SNR degradation from 40%-60% to 5-10%. Regardless of the steps taken to reduce noise, the motors are not intrinsically compatible and the associated problems of introducing these electric motors into the MRI room will always be present to some extent.

Recent research efforts have been made into several other forms of MR compatible electric actuation, but each has its significant drawbacks, as well as SNR reduction. Plante et al. [42] have attempted the use of dielectric elastomer actuators, but require better dielectric elastomer manufacturing technology in order to develop a system with adequate positioning accuracy. Yamamoto et al. [43] have developed MR compatible electrostatic film linear motors, but the systems require high voltage (over 1 kVAC) to provide adequate thrust. These voltage requirements are not only a potential safety hazard but are capable of generating an excessive amount of EMI. Vogan et al., [44] have demonstrated the MRI compatibility of electrostrictive polymers, however, these devices are limited to two stage "on/off" actuation which significantly limits

application. Although these technologies are not ideal as general purpose actuation solutions, they may be adequate to a future system with special requirements.

2.2.3 Electromagnetic Actuators

Electromagnetic actuators either operate by taking advantage of the magnetic field of the MRI or contain ferromagnetic materials. An example of a motor which takes advantage of the magnetic field of the MRI is presented by Roeck et al. [45] who have developed an an MRI compatible electromagnetic motor which operates by the same principles as a permanent magnet motor, but the static magnetic field of the MRI is used in place of the permanent magnet. SNR reduction from this device was reported to be 2%.

Standard permanent magnet motors such as DC motors, and stepper motors are also examples of electromagnetic actuators. Such devices have extreme magnetic susceptibility and must be kept a distance from the MRI both for image quality and safety. There is an inherent danger when bringing ferromagnetic devices into the MRI room so these items must be kept a safe distance away from the MRI and anchored appropriately. Permanent magnet devices have not been used in the MRI room in literature until our motion phantom [46] which will be discussed further in the next chapter. This device had several performance constraints for which traditional forms of MRI compatible actuation were not suitable so standard permanent magnet stepper motors were used to remotely provide actuation through driveshafts. The kinematic results of this device were excellent and it is adequately safe for a phantom used only for research purpose. However, it is not likely that a commercial device will ever be produced which uses ferromagnetic motors inside of the MRI room.

2.3 MRI Compatible Surgical Robots

2.3.1 Introduction

To address the many constraints of intervention within an MRI, several MRI compatible robotic systems are being developed. The benefits of using a robotic system are that the robot can be designed to operate within the constraints of the MRI. By use of teleoperation, the surgeon can control the robot from outside the MRI bore or even from the MRI control room. This allows the surgeon to perform interventions which would be otherwise impossible due to space constraints. The primary use of these robotic systems thus far is positioning to benefit from the improved accuracy of image guided robotic systems. Only very simple linearly actuated or manual actuated intervention tools have been used in MRI compatible robots to date. Due to the additional design constraints of MRI compatible robots, current technology falls behind compared to standard surgical robots where commercially available systems already have many dexterous manipulators. However, as positioning systems are improved and higher speed real-time tracking systems become a reality, manipulators will have to be improved accordingly. For now, systems are compared mostly by two performance metrics accuracy and MRI compatibility.

Most early MRI compatible robotic works use an open MRI such as the surgical assistant robot shown in Figure 2.3.1.1 below by Chinzei et al. [47]. However, due to the motivations to create systems which work in closed-bore MRI systems, recent research is focused solely on closed-bore compatible systems. All of the robots surveyed below are designed for use in IMRI and MRI closed-bore scanners with afield strength of 1.5 T or greater. Several of them have image guided capabilities using preoperatively collected

data. Currently only one robot, NeuroArm is capable of using intraoperative data. All of these robots have been designed to meet the needs of either general purpose positioning, prostatic-intervention, or neuro-interventions so they are organized accordingly.

Figure 2.3.1.1. Surgical assistant robot and "Double-Donut" style IMRI machine.

2.3.2 General Purpose

Gassert et al. [30] presented a very simple 1 DoF robot to demonstrate the concept of remote actuation for MRI compatible robots (Figure 2.3.2.1). The system uses hydraulic actuators to actuate a 1 DoF wrist from 10 m away. Reflective light sensors transmitted through fiber optic cables were used as force sensors. This early work indicated that remote hydraulic actuation and optical sensors could provide sufficient motion and feedback for MRI compatible robotic interventions and remote actuation as a method of MRI compatibility was used by many of the groups to follow.

The first commercialized MRI compatible robot is the INNOMOTION arm (Innomedic, Herxheim, Germany). The INNOMOTION is a 5 degree of freedom (DoF) positioning arm with an additional 2 manually actuated DoF Figure 2.3.2.2. This robot

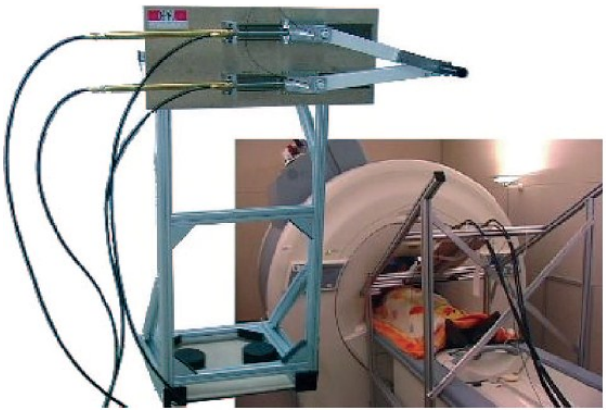

Figure 2.3.2.1. Single DOF hydraulic powered robot.

has been used clinically for many different interventions including sciatic pain and facet joint treatments, biopsies, drainages, and CT-guided osteosynthesis [48]. The first INNOMOTION design used piezoelectric motors, but they were eventually discarded in favor of pneumatic actuators due to problems with piezoelectric motors such as signal noise during scanning, risk of inductive heating, and gear backlash. All components including sensors and pneumatic cylinders were MRI compatible and designed out of polymers and or ceramic materials.

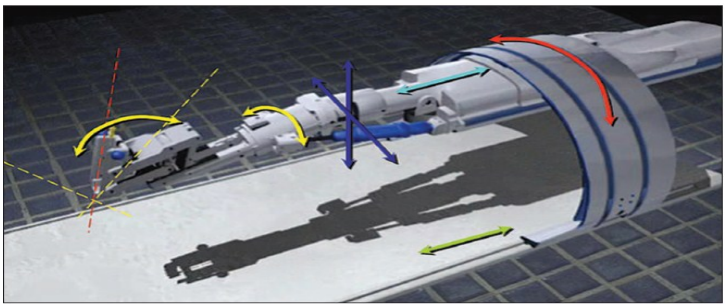

Figure 2.3.2.2. CAD drawing and schematic of the Innomotion Arm.

Kapoor et al. have adapted this device to perform transapical aortic valve implantation [49] by adding a 3 DOF MRI compatible valve delivery module to the end effector (Figure 2.3.2.3) as well as developing a cooperative hands-on interface [50] to

control the robot position. MRI compatibility experiments demonstrated an SNR loss of 8.2% when the system was in motion and absolute system error was measured to be 1.14 ± 0.33 mm over seven trials.

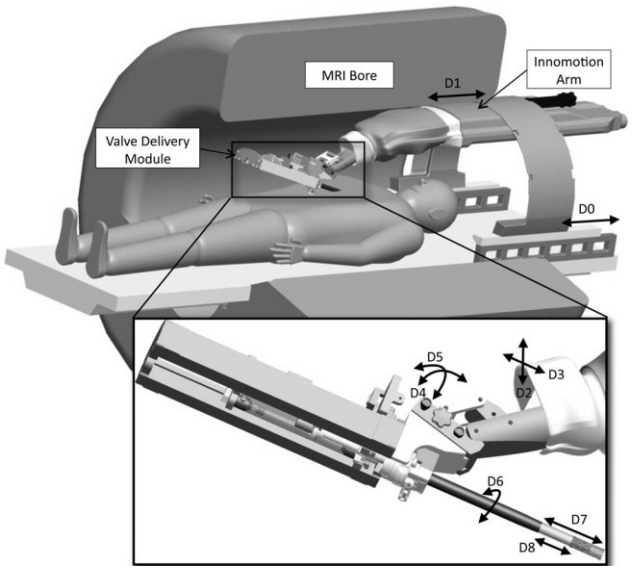

Figure 2.3.2.3. INNOMOTION arm with addition of valve delivery module.

Tsekos et al. [16] have also presented the general purpose image-guided MR-compatible robotic arm shown in Figure 2.3.2.4. Rather than MRI mounted like the INNOMOTION arm, the robot base sits on the floor outside of the MRI. In total the device has 7 DoF consisting of a 3 DoF Cartesian stage, which positions the arm inside the scanner, and the 3 rotational DoF and 1 translational DoF which make up the arm itself. Piezoelectric motors (Shinsei) are used for actuation but, unlike the original INNOMOTION design, all motors were located on the base of the robot, outside of the imaging plane to reduce interference. MRI compatible materials were used to construct the device including fiberglass, plastic, brass and aluminum. SNR results initially indicated a 82% reduction in SNR during operation, however, after shielding the wires SNR reduction was around 30%. Accuracy was measured to be ± 3.2 mm and ± 3˚.

This device is image-guided and capable of target positioning based upon preoperative image data, or manual control. When operated manually the device commands the MRI for on-the-fly adjustment of the imaging plane based upon the robots position and tool orientation and the commanded robot movements are continuously checked to avoid collision. On-the-fly adjustment and collision detection were two significant advancements for MRI robotic IGI.

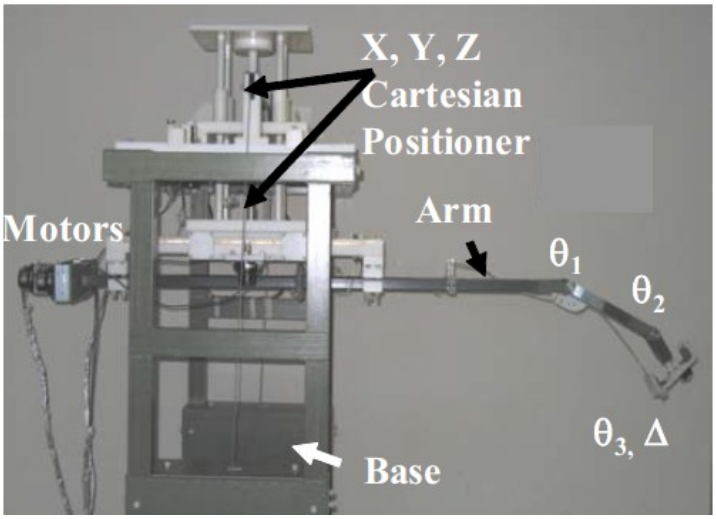

Figure 2.3.2.4. 7 DoF general purpose positioning robot.

The Light Puncture Robot (LPR) by Zemiti et al. [33, 51] is both CT and MRI compatible which uses non-metal pneumatic actuators (Figure 2.3.2.5). The pneumatic actuators are coupled with a sprocket gear so that they may be used to make discrete step motion with excellent open-loop accuracy and eliminate the non-linear dynamics intrinsic to pneumatic actuation. The LPR was also the first body supported MRI compatible robot since it is attached to the patient rather than the gantry to reduce the risk of trauma from unexpected patient motion. Within a work area of 30 mm horizontal and 2 mm vertical, the LPR demonstrated less than 2 mm

and 1˚ error. Outside of this work area the error is much larger and the robot requires adjustment.

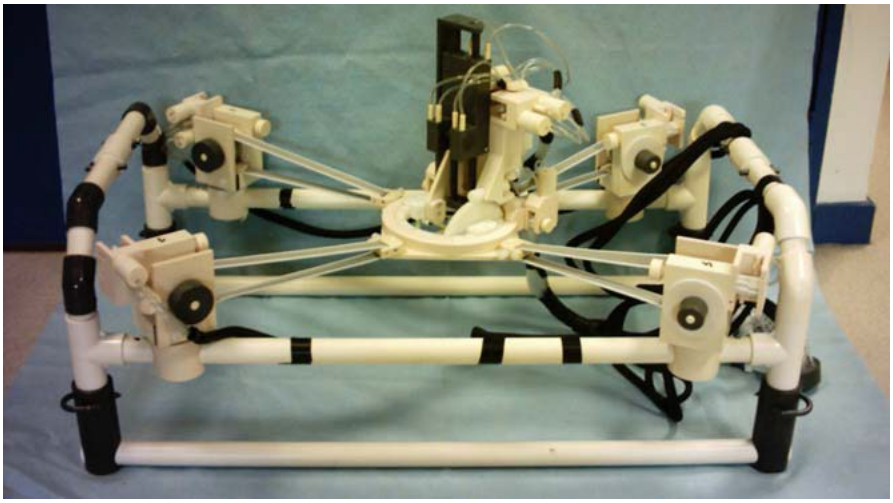

Figure 2.3.2.5. Lightweight Puncture Robot (LPR), a patient mounted robot.

2.3.4 Prostate

MRI-P [40] is a 6 DoF robot (Figure 2.3.4.1) designed for prostatic interventions including ablation, brachytherapy, and biopsy. DoF include translation in the 3 cartesian directions plus roll pitch and yaw of the end effector. This robot is directly actuated by piezo electric motors (Shensei) and as a result this robot demonstrated significant noise during MRI scanning. The robot also suffered problems with encoder signal interference which lead to incorrect readings. The robot motion was briefly disabled while scans were performed to attempt to allieviate these issues. The robot was almost entirely constructed of non-magnetic aluminum which is safe to use but caused some imaging artifacts in "non-critical" areas. Accuracy results indicated less than 2mm positioning error.

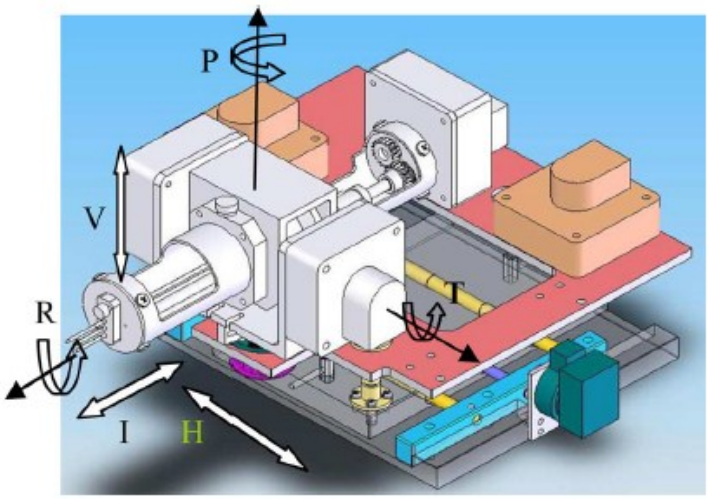

Figure 2.3.4.1. MRI-P a 6 DoF robot for prostatic intervention.

Krieger et al. have developed and tested a remotely-actuated manipulator for accessing prostate tissue under MRI guidance [52]. This device (Figure 2.3.4.2) provides three-dimensional guided needle placement (under physician control) with millimeter accuracy. The device can be used for needle biopsy, fiducial marker placement, and therapy delivery to the prostate. The robot kinematics consists of only 2 DoF: one translational DoF and one rotational. The device was constructed mostly of plastic however limited quantities of aluminum, brass, and bronze were used. The device uses remotely actuated piezo-electric motors (Nanomotion Inc., Yokneam, Israel). MRI testing

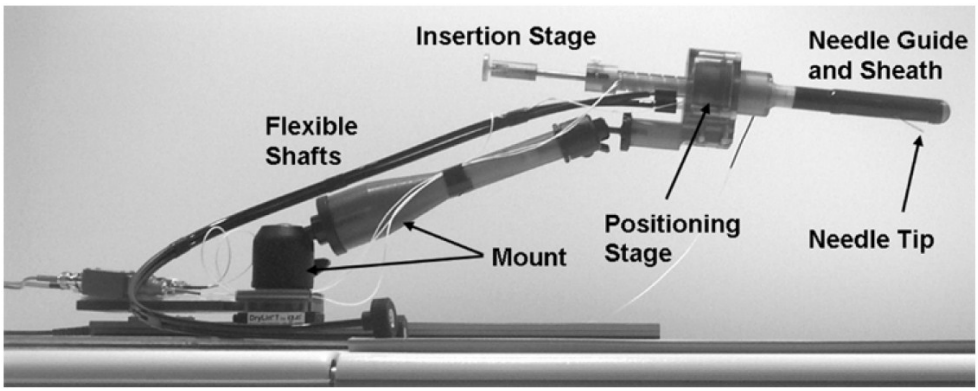

Figure 2.3.4.2. APT-MRI, a 2 DoF robot for prostatic intervention.

results show no reduction in SNR with the motors disabled, but 40% to 60% reduction in SNR with motors enabled [38]. Results from two human clinical trials were published in 2011 [53] demonstrated maximum targeting error of 1.8 mm and mean error of 1.1 mm.

Another recent system for guided prostatic interventions is presented by Fischer et al. [32]. This transperenial needle placement system (Figure 2.3.4.3) has 4 actuated positioning DoF, 2 prismatic, and 2 rotational. It also features one additional manual prismatic DoF for gross axial positioning and needle insertion is also manual. Actuation of this device is performed by custom non-metallic pneumatic cylinders. The robot support base, which also acts to isolate metallic components from the patient's body in case of heating, is mounted on the gantry of the MRI and the patient places his legs over the base. SNR reduction is limited to 5% for standard prostate imaging sequences, significantly less than that of the APT-MRI. Positioning error was measured to be better than .94 mm rms per axis.

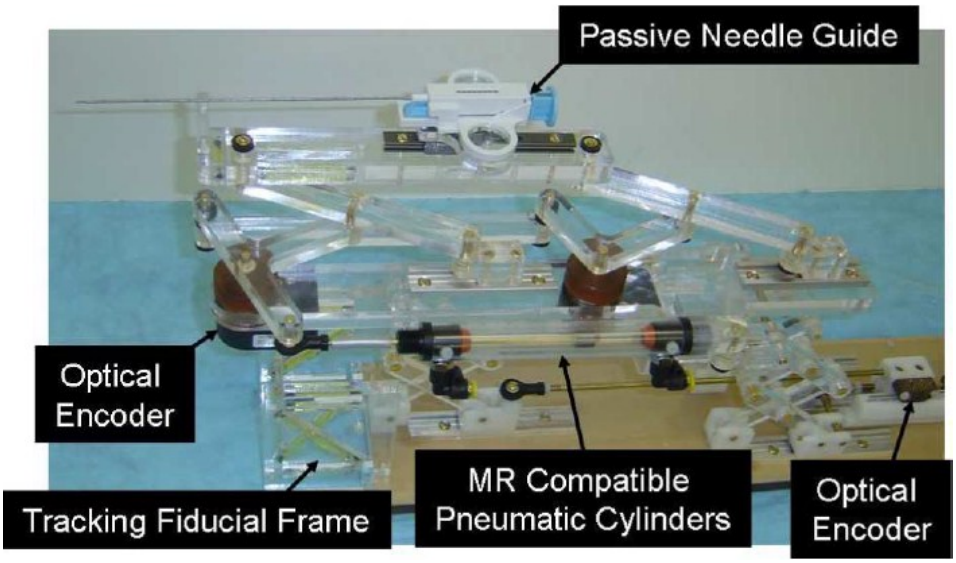

Figure 2.3.4.3. A pneumatic robot for prostatic interventions.

The MrBot [54] is yet another MRI compatible robot for prostate brachytherapy. This robot (Figure 2.3.4.4) features 5 DoF, 3 translational, and 2 rotational. The actuation configuration allows for automatic needle manipulation, insertion, and seed deployment and this is the only prostatic intervention robot with actuated needle insertion at this time. The system is actuated by custom designed pneumatic actuators known as the PneuStep which have similar kinematics to traditional stepper motors. Mean positioning error was measured to be 1.14 mm and SNR reduction was not analyzed.

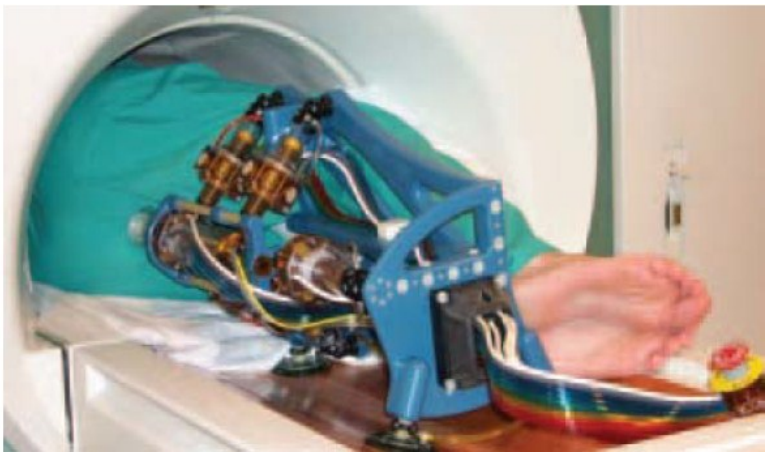

Figure 2.3.4.4. MR Bot - robot for automated brachytherapy in the prostate.

2.3.5 Neurosurgery

First published in 2003, the NeuroArm [10] is an MR-compatible image-guided ambidextrous robot capable of both microneurosurgery and stereotaxy and is designed to be seamlessly integrated with IMRI. The robot (Figure 2.3.5.1) has 8 DoF total from two arms which have 4 DoF each. The first 3 DoF are in a typical SCARA configuration which is commonly used in industrial robots for rigidity in the direction of gravity. At the end of the arm is an additional 1 DoF actuator to operate the surgical tool mechanisms. The robot is designed from titanium metal components and PEEK plastic which were

chosen amongst testing of aluminum, titanium, carbon, and glass composites for their structural stiffness and MRI compatibility. Piezo-electric motors were chosen as an actuation method because of their 20 kh lifetime, 1 nm resolution, and inherent braking [35]. First human testing was performed in 2008 when the NeuroArm helped surgeons remove a brain lesion from a human patient.

The Neuro-Arm is mounted on a moveable floor base which is positioned above the head outside of the MRI scanner. The robot is image-guided using images collected from the iMRI. Stereotactic procedures can be performed inside of the MRI bore using images acquired in "near real time" [35]. However it was a design decision that microsurgery be performed outside of the bore. During imaging for microsurgery the robot must be placed behind the 5 G line of the MRI.

Figure 2.3.5.1. NeuroArm uses preoperative data for operation.

2.4 Stepper Motor Control

Stepper motors are electromagnetic actuators widely used in industrial applications such as robotics, aerospace, medical, machine tools such as computer numerated control, printers, and scanners because of their many benefits including simple

brushless operation, high reliability, high torque, accurate, open loop stable positioning [55]. These properties provide that, under the right conditions, stepper motors can be positioned accurately without the need of feedback or complex control. These ideal conditions rely upon selection of a motor with the correct parameters for the system such as: torque, inductance, and rotor inertia, operation parameters (mainly acceleration), and external parameters such as: loading torque, disturbance torque, and system inertia.

Stepper motors convert discrete pulses to motion by making use of electromagnetic properties. The stepper motor stator is made up of at least two electromagnetic coils which have a selectable polarity and the rotor is made up of a permanent magnet. Due to the magnetic interaction, the rotor will find position at an equilibrium point depending on the polarity of the stator coils and holds position as long as the torque applied to the rotor is not greater than the holding force of the magnets. Simply switching the stator coil polarities will cause the rotor to change position to a new predictable equilibrium point and hold position again. This discrete and stable stepping phenomenon allows the stepper motor to be operated precisely without feedback as long as the dynamic properties of the motor do not interfere with the motion of the rotor to the new equilibrium point.

Even though the control signal moves discretely, a mechanical ringing occurs at each step and a settling time at the equilibrium point for the inertial forces to dissipate. This dynamic effects of this ringing and settling time, will cause the stepper motor to fail to execute step commands under high stepping rates, high load, spontaneous reversals, or operation at certain resonant frequencies [56-58]. For this reason, motor, driver, and operation parameters must be chosen carefully for the application. Furthermore it can be

concluded that open loop control of permanent magnet stepper motors are not ideal for dynamic systems which may be high in friction, loading torque, or for other systems which these parameters cannot intrinsically controlled.

Several methods have been explored to reduce or overcome these limitations. Mechanical damping added in the form of a damper to the motor, electrical damping introduce through control circuitry, and microstepping are three methods used to reduce the magnitude of ringing and resonance in stepper motors [57]. However, the dynamics of the system cannot be completely eliminated, or easily modeled. Therefore, to improve operation under such conditions, Many linear and nonlinear closed loop control techniques have been explored to improve the performance of stepper motors including proportional integral derivative control (PID) [55], passivity, feedback linearization, sliding mode control, and other methods (see [55, 59-62] and references therein).

2.4.1 Feedback Measurement:

Feedback control is performed based upon mechanical states of the motor, usually position and or velocity. In most cases these states are measured directly through mechanical sensors, however, because the addition of mechanical sensors to the motor will increase the cost and size of the system, sensorless methods of determining rotor position have been developed. Anzai et al. [63] have demonstrated that rotor position can be determined from measurement of back EMF induced by the flux from the DC voltage excitation of the motor during positioning. However, the magnitude of back EMF is proportional to the speed of the motor. Although the measurement accuracy is high for medium to high speed, the rotor position cannot be determined accurately at low speed or standstill [64]. Bianchi et al. have solved the low speed problem by using high frequency

signal injection into the stator, which modulates the signal depending on the rotor position [65] and extended Kalman filters are often used with these methods to accurately estimate the mechanical states of the motor from only current and voltage measurements.

Experimental results presented by Bendjedia et al. [66] demonstrate very high accurate position and speed estimation using Kalman filters for medium to high speed measurement and back EMF measurement of a 1.5 A current injection to measure standstill and low speeds. The experimental results presented in Figure 2.4.1.1 [66] demonstrate the effectiveness of the method which is indeed a suitable replacement for mechanical sensors. However, there is always a tradeoff when saving costs. Although this method eliminates the need of a costly mechanical encoder, the additional 1.5 A current injection for low speed and standstill state will increase motor heating and is not suitable for low power or mobile applications as this current is 25 times greater than the current used for an optical encoder (US Digital) as a feedback sensor.

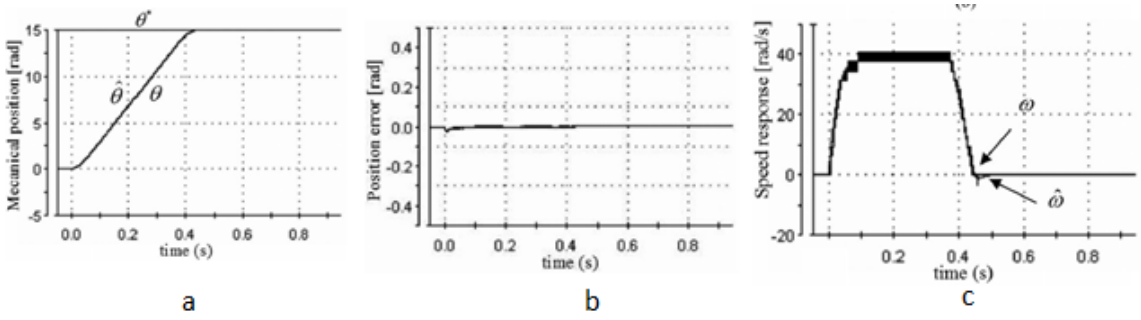

Figure 2.4.1.1 a) Reference trajectory b) position error of estimated position vs. measured position c) speed error of estimated speed vs. measured speed.

Although these methods of sensorless state estimation reduce the overall cost, size and complexity of the system, they will intrinsically provide some additional error over their mechanical sensor counterpart. Since a feedback controller cannot compensate for loss in precision through the feedback itself, it may be preferred in some situations to use

the mechanical sensors. However, state estimation may be more accurate in cases where the order of the state variables exceeds that of the order of the mechanical sensor. For instance, in the case of a velocity controller which only has a position encoder, the derivation of the encoder signal to provide velocity will most likely cause greater noise than that which was demonstrated by the state-estimation provided by back EMF and a Kalman filter presented by [66]. Likewise, higher order control systems requiring acceleration state feedback, such as the third order sliding controller presented in [60], require an accurate measurement of acceleration. Currently, an accurate method of motor rotational acceleration measurement is not easily found in commercially available mechanical sensors, but it could be acquired using a nonlinear observer.

2.4.2 Nonlinear Control

Regardless of the method of feedback measurement or state estimation, many control methods have been proposed to overcome the dynamic effects of the stepper motor under conditions which are not ideal and provide smoother more accurate positioning. Although the stepper motor intrinsically exhibits many high order nonlinear dynamics, most commonly used closed loop control scheme in industry is PID or one of its derivatives such as PI. Since the motor cannot be accurately linearly, and the plant itself will be subject to even more nonlinearities and disturbances, PID gains cannot be determined mathematically and the stability cannot be proven [67]. The PID gains are determined therefore heuristically through a method such as Ziegler Nichols, or empirically through simple trial and error [61]. It has also been suggested that since positioning system is under constant acceleration, a linear or gain scheduled control law

cannot make adequate use of the motor torque to track position with accuracy [59]. For these reasons many groups are exploring nonlinear methods of closed loop control.

Closed loop position control of the permanent magnet stepper motor through feedback linearization was first presented by Zribi et al. [62]. Their work cancels the nonlinear dynamics through exact linearization by the construction of a very detailed mathematical model of the stepper motor which is based upon the parameters of current, voltage, inductance, and resistance of each motor phase as well as the number of rotor teeth, the motor torque constant, viscous friction constant, rotor speed, rotor position, and detent torque. After cancellation of the nonlinear term is performed, assignment is made to include an integral term which is used to eliminate unexpected error from disturbances, imperfect cancellation of nonlinear terms, and unmodeled system dynamics.

Feedback linearization requires a precise mathematical model of the system, but as discussed previously the overall system of a stepper motor positioning system relies on many dynamic or even unpredictable parameters which cannot be modeled or estimated. Therefore this implementation cannot account for the load disturbances or unknown dynamics of the actual system even with the addition of an integral term as in [62]. More robust techniques are required to compensate for these dynamic parameters.

Robust adaptive control was implemented by Melkote et al. [68] to provide robustness against plant dynamics such as friction, load torque and cogging torque. One major benefit of this technique is that it only requires position feedback which could be easily obtained by a standard rotary encoder or a state estimation method. In this work, stability was proven using Lyapunov techniques, and performance was proven through simulation, but no bench testing was performed. Krishnamurthy et al. also proposed a

similar control scheme, but with a more detailed motor model [69]. Similarly, there were no actual benchtop results provided, therefore adaptive control at this time should be considered as a theoretical practice more than a proven method of nonlinear feedback control for permanent magnet stepper motors.

A more proven robust method of closed loop control for stepper motors is sliding mode control. For this reason sliding mode control has been implemented by many groups to guarantee robustness against parameter perturbations, external disturbances, and measurement errors. Zribi et al. [70] have presented a first order sliding mode controller which proves to be robust and accurate. However, it is pointed out by Nollet et al. and other groups that with a first order sliding mode controller, high frequency oscillations are present at the sliding surface. These oscillations result in a rapidly switching command output which results in a "chattering" phenomena of the motor, e.g. the rotor of the motor continuously overshoots the set point by a small amount and never settles to the equilibrium point. Although the system is marginally stable and remains within the general vicinity of the set point, several disadvantages will occur from chattering such as overheating of the coils, instability due to vibration, wasted power, and overall it prevents the motor from reaching an equilibrium point or where it can provide holding torque.

To overcome these shortcomings, a second order sliding mode controller has been applied to the permanent magnet stepper motor by Nollet et al. [71] who demonstrated that higher order sliding mode control laws can reduce chattering of the stepper motor while preserving robustness of control. For a reference trajectory of around 6 radians, maximum position errors of less than 0.01 rad were measured and maximum speed errors

of less than 0.6 radians per second were measured. Further experiments demonstrated the effectiveness of this controller for trajectory tracking and its capability to compensate for unknown variations in torque and system parameters. However, the derivation of tuning parameters used in these experiments was not provided.

A third order sliding mode controller for stepper motors was presented by Defoort et al. [60] which also guarantees robustness and reduced chatter, but offers additional benefits. The proposed third order controller removes the requirement of knowledge of initial rotor state since only speed and acceleration feedback are required and not position. This removes the need to estimate the standstill rotor position and will save hardware, computation time, and power over the previously mentioned control methods which require back EMF and current injection. Also there is no need for offline computation required. Speed and acceleration are estimated through a second order sliding mode observer and no mechanical sensors are used. Position and speed tracking results are comparable to those in [71] but with added robustness and without the need of mechanical sensors or offline computation. Another feature of this presented work is that the controller and tuning parameters are constructively and formally derived so stability is proven and heuristic tuning is not required.

Another robust approach to stepper motor control is the artificial neural network (ANN). ANNs are an attractive option because they require no mathematical model to provide learning control to a system with ill-defined and incomplete information. Rubaii et al. [72] have presented a two distinctive layer ANN system to identify and control the nonlinear stepper motor system. The first part is referred to as the neural network identifier (NNI) which captures the dynamics of the system and the second part

is referred to as the neural network controller (NNC) which provides the necessary control action to perform velocity tracking. The training of the neural network is performed online which means the performance of the system will continuously improve overtime. Experimental results demonstrate excellent tracking and disturbance rejection. Comparison between results of the ANN system to a PID system, as shown in Figure 2.4.2.1 below, demonstrates that the tracking and disturbance rejection is far superior to that of the linear PID control.

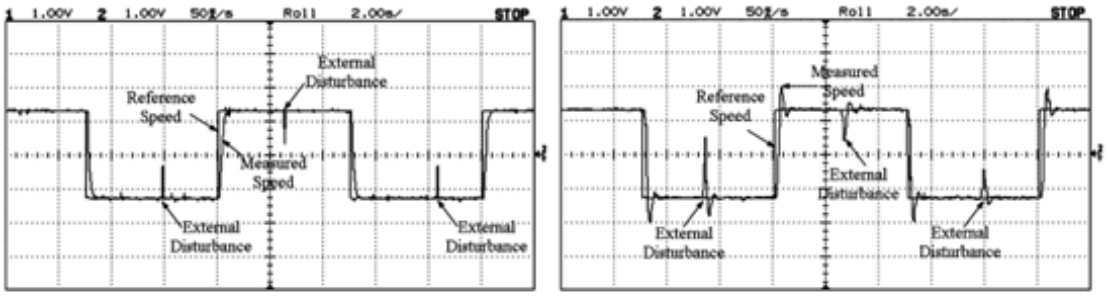

Figure 2.4.2.1 Velocity tracking with external disturbance for a) ANN as compared to b) PID control.

In conclusion, the use of highly dynamic stepper motors in motion trajectory control presents a challenging control problem. All of the closed loop control methods mentioned reviewed here require state feedback which can be obtained either through mechanical sensors or obtained through an observer or state estimator. A detailed mathematical model of the stepper motor has been used to cancel nonlinear dynamics of the stepper motor through feedback linearization, however, this method is most likely not robust enough for motion control systems which will have nonlinear dynamics and disturbances. Robust adaptive control has been demonstrated by several groups in simulation but has not yet been proven on hardware. The model based nonlinear control method which has proven to provide the best tracking results is the third order sliding

mode control which has the important benefit of not requiring initial rotor position information. Another robust approach to solving the closed loop stepper motor control problem is ANN which require no mathematical model of the system, but perform online learning to perform tracking. However, currently it remains that the most basic and commonly applied control scheme is linear PID control.

3. Motion Phantom

3.1 Motivation and Goals

The research and development of MIS and IGI entails the development of enabling methodologies and technologies to perform operations within highly dynamic environments. An example of such an operation is aortic valve implantation on the free beating heart. Natural motion as a result of breathing and heartbeat continuously alter the Area of Operation (AoO). To develop, validate, and optimize a new clinical approach requires in vivo studies on animal models and eventually on humans. Although animal and human studies are absolutely necessary for eventual acceptance of any new method, development of these procedures would benefit greatly from validation on a phantom before testing on living models. Phantoms that can mimic the physical properties, dimensions, and motion of the tissue of interest can provide an accurate and reusable representation of the dynamic environment to validate and optimize the procedure. Several such phantoms, including anthropomorphic ones, are used in both surgical research and in training [73, 74].

Due to the benefits of MRI presented in Section 1.4, groups have begun the development of cardiac surgery under MRI guidance, specifically the operation of Transaplical Aortic Valve Implantation (TAVI) both manually [23] and robotically [49, 74]. Sophisticated computer methods of planning and control of the TAVI operation presented by Yeniaras et al. [75-77] and methods of feature extraction and integration of real-time MRI with robot control by Navkar et al. [78, 79] have provided a solid foundation for the development of MRI guided cardiac surgery tools.

The goal of this work was to design an MR compatible, computer controlled, and actuated phantom that can mimic the motion and geometric constraints of the beating human heart. In addition to being part of the ongoing development of a system for image-guided intracardiac surgeries [75-79], the primary motivations for developing such a device are the following:

- Reduce the development cost for imaging and robotic systems, as compared to animal or excised heart models.
- Reduce the number of animal studies; relieving some of the pressure by the ethical dilemmas of animal testing.
- Serve as a versatile and reusable test bed for evaluating the methods of procedure practice, and as a training platform.

This work, of which the mechanical design has been published in [46], and the preliminary motion and MRI compatibility results have been published in [80], not only provides the above contributions to the larger Multimodal Image-guided RObot-assisted Surgeries (MIROS) project but provides important results to fields of MRI compatible robotics and mechatronics community through the use of remote actuation to use traditionally incompatible actuators in the MR environment. The research of this work also lead way to further research into tracking control of stepper motors under high acceleration and the development of a multi-axis precision motor control on FPGA which are presented in the next Chapter.

3.2 Concepts and Realization

The motion phantom was developed primarily to serve as a validation system and test bed for the TAVI procedure. Following the concepts of the robotic manipulator

presented by Yeniaras et al. [81] and the TAVI procedure, presented by McVeigh et al. [23] the area of operation is considered as shown in Figure 3.2.1. Presented within the figure is a long-axis MR image of the human heart with an overlay of a virtual flexible robotic manipulator (blue) that enters via a transapical trocar (pink) and advances through the left ventricle to the aortic annulus for delivering a prosthetic aortic valve [8]. Analysis of this topography reveals the critical landmarks of the heart associated with such a procedure which include: the apex (through which a trocar is inserted), the endocardial surface of the left ventricle, and the aortic annulus. As shown in the figure, a simple yet accurate way to represent those landmarks would be as three cylinders.

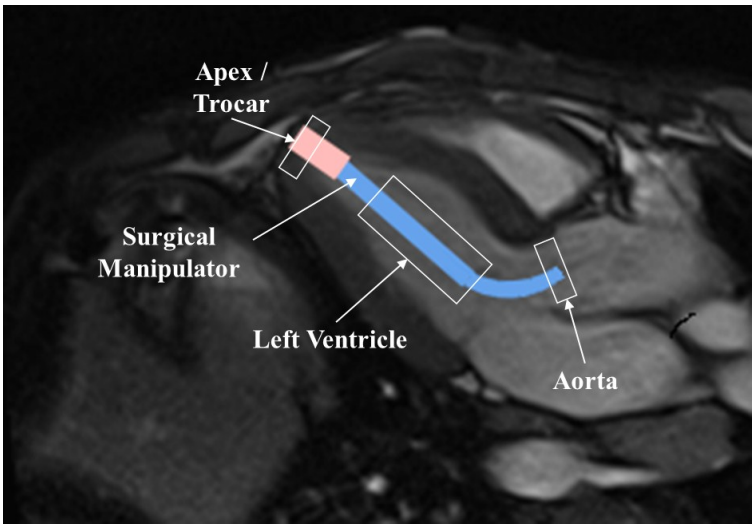

Figure 3.2.1. Topography of an intracardiac procedure for aortic valve annuloplasty using a robotic manipulator. Relevant cardiac landmarks: apex, left ventrical and aortic annulus superimposed to long axis image of the heart.

In the free beating heart, the three previously described landmarks move in 3D space with a continuous periodic motion. The dimensions and motion of these landmarks, which have been extracted from CINE MRI images by Yeniaras et al. using the methods described in [81] can be used to generate trajectories of relative motion and an appropriate kinematic structure was created to emulate the moving area of operation. All

possible motion of a cylinder in 3D space except rotation in the axial direction can be represented by use of the three Cartesian coordinates: X, Y, and Z of two points along the cylinder P1 and P2. (Figure 3.2.2). The open faces of the tubular structure, P1 and P2, move independently as the heart beats and can be actuated by two separate Cartesian stages. Therefore the motion phantom will be designed as six Cartesian stages to actuate the three cylindrical cardiac landmarks.

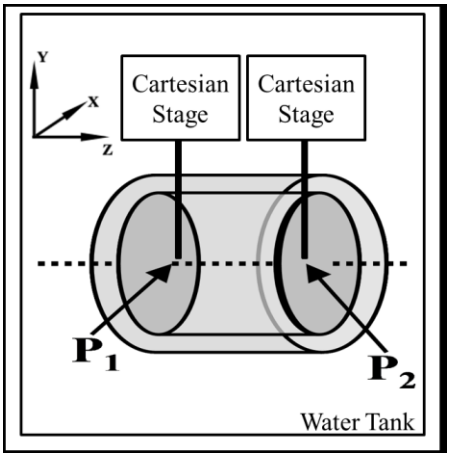

Figure 3.2.2. Two Cartesian stages can be used to control the three dimensional motion by actuating points P1 and P2 in 3D space.

3.3 Physical Design and Prototype

Although several types of actuators can be used for MR compatibility including pneumatic, piezoelectric and hydraulic [5, 6, 12], standard electromagnetic stepper motors have been selected as the actuators for this work because they can provide repeatable and precise motion with a high torque to size ratio. However, since electromagnetic stepper motors are not MRI compatible, a remote actuation method is required to locate them a safe distance away from the scanner's magnetic center. This distance is based specifically on the fringe field of the scanner which in this study is the Siemens MAGNETOM Avanto 1.5T MR scanner. The static fringe field strength

provided by the manufacturer's planning guide is presented in in Figure 3.3.1 as a contour plot. The strength of the field at the distance of 2 to 2.5 meters (m) away from the center of the scanner is approximately between 20 and 5 milliTesla (mT) respectively. Therefore it was determined that a phantom 2.5 m in length would allow the end-effectors to be brought into the bore of the machine while the motors remain in a region of low magnetic field.

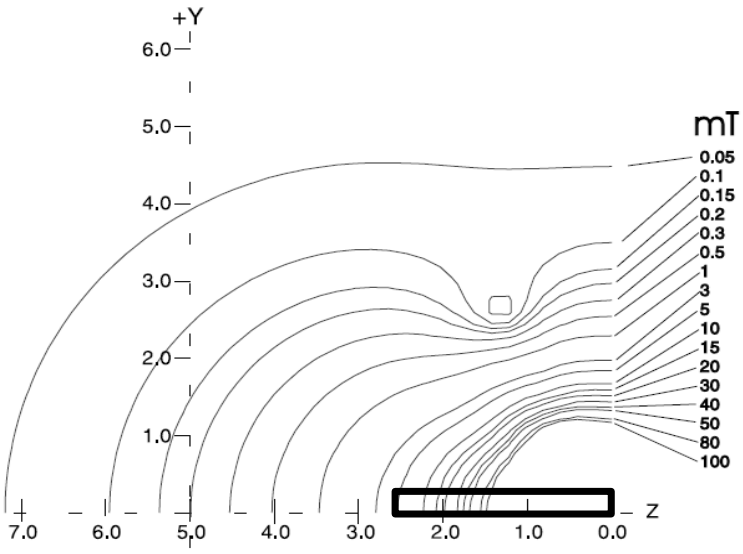

Figure 3.3.1. Fringe field for the Siemens MAGNETOM Avanto 1.5T MR Scanner. Origin at the magnetic center. Axis units are meters. Box represents the area occupied by the phantom.

Motor controllers, power supply and other electrical equipment generate RF noise which will potentially be received by the MRI machine and cause artifacts. Therefore this equipment is kept outside of the MRI room and passed into the room through shielded cables. More details on cable shielding and passing signals into the MRI room is given in section 4.3. In addition to the remote placement of the actuators to ensure MR-compatibility and safety in physical prototyping, non-paramagnetic materials were selected for placement inside of the MRI scanner. Non-conductive materials were

preferred because they will not produce imaging artifacts. Acknowledging these constraints the phantom is constructed mostly of plastic and composite materials such as ABS, acrylic, carbon fiber, and fiberglass. Non-magnetic metals were used sparingly where necessary. These items include aluminum rivets and brass spur racks and gears used to transfer motion via rack and pinions.

This phantom consists of six stages, one for each of the two points of actuation for each cardiac landmark cylinder. Each stage, which must account for three directions of motion: horizontal, vertical, and depth, or X, Y, and Z respectively, is designed as a long structure capable of rolling on a single fixed base. Each Cartesian stage (Figure 3.3.2) is composed of a 2.5 m rolling platform (a) which extends from the motor side (b) of the stage to the actuation side (c). The motor side is located 2.5 meters from the MRI magnetic center, and the actuation side is placed inside the bore of the MRI machine. This platform rolls on the phantom base (not shown in this figure) to give motion along the Z axis which is the long axis of the MRI. On top of this platform (a) rest two carts (d and e) which are actuated by the same driveshaft so that their movement is coupled. One cart (d) contains a motor and the other cart (e) contains a rack and pinion. The parallel movement of these carts provides movement of the end-effector in the X direction (horizontal short axis), while the motor and rack and pinion mechanism inside of the carts actuate the end-effector in the Y direction (vertical short axis). The color scheme of the figure represents the direction of movement for each part, i.e. parts which move in the X, Y, and Z directions are colored red, yellow, and green respectively. Motion of both Cartesian stages provides resulting 3D positioning to the anatomical structure (f) via points P1 and P2.

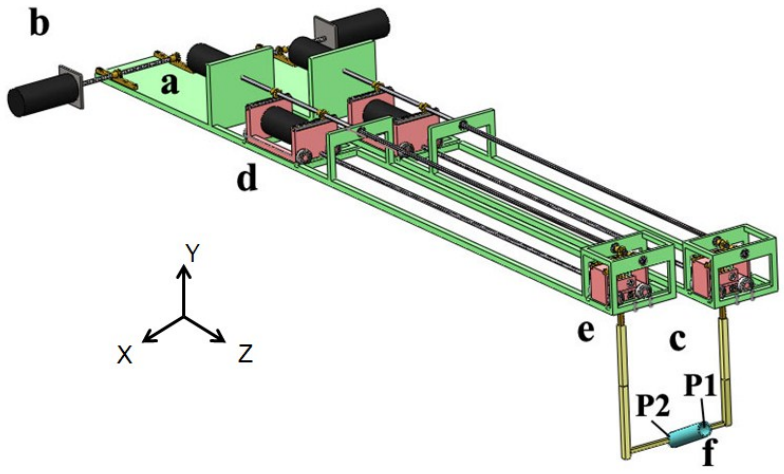

Figure 3.3.2. Model of two-Cartesian stages a) 2.5 meter long platform, b) Motor side, c) Actuation side, d) Motor cart, e) Rack and pinion cart f) Cardiac landmark. Color corresponds to direction of motion.

From the MRI data collected it was determined that each stage should be capable of moving a minimum of 10 millimeters in the x, y, and z directions in order to account for the maximum beating heart motions. However, for configurability, each stage was designed capable of a 20 mm range of motion. Since space inside an MRI scanner is limited, the phantom was designed to be as small as possible with the ability to complete its three Cartesian motions. The resulting size of each individual stage is less than 7 centimeters wide and 5 centimeters tall. Preliminary Cartesian stages [46] were built using only carbon fiber in a truss configuration and transmitted power through carbon fiber driveshafts as shown in Figure 3.3.3. However, issues were found with the straightness of the carbon fiber trusses. A better solution was to use laser-cut acrylic as the foundation of the stages and carbon fiber rods across the top of the stage for rigidity. The proposed carbon fiber driveshafts provided too much torsional flexibility and were replaced by aluminum 7075 alloy rods. These aluminum driveshafts rotate through PTFE

bushings. The remaining structural parts of the stage were constructed of ABS plastic or acrylic. The final version of the Cartesian stage is presented in Figure 3.3.4.

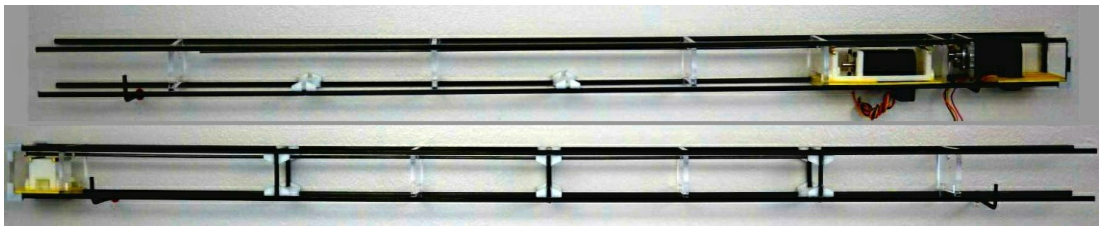

Figure 3.3.3. Original carbon fiber truss design with carbon fiber driveshafts. Due to length, the stages are stored and transported in halves.

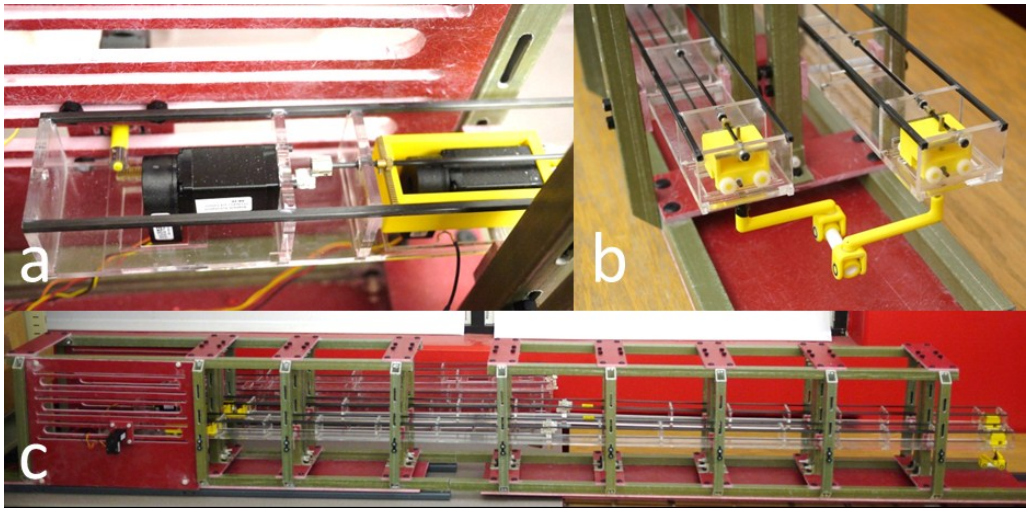

Figure 3.3.4 Views of a) motor side b) end effector c) overall view of two of the final version Cartesian stages made from laser cut acrylic.

Space inside of an MRI scanner in which robots can operate is constrained to 60 cm horizontally and 40 cm vertically and the overall dimensions of the main actuation structure of the phantom are 37 cm high and 23.5 cm wide. The cardiac landmarks can be accessed from the opposite side of the MRI than that of the patient couch. Figure 3.3.5 shows the overall phantom and the structural base which holds the stages. The base was designed of structural fiberglass. This material was the most rigid of the plastics and composites tested which included LDPE, PVC. Garrolite, and Acrylic.

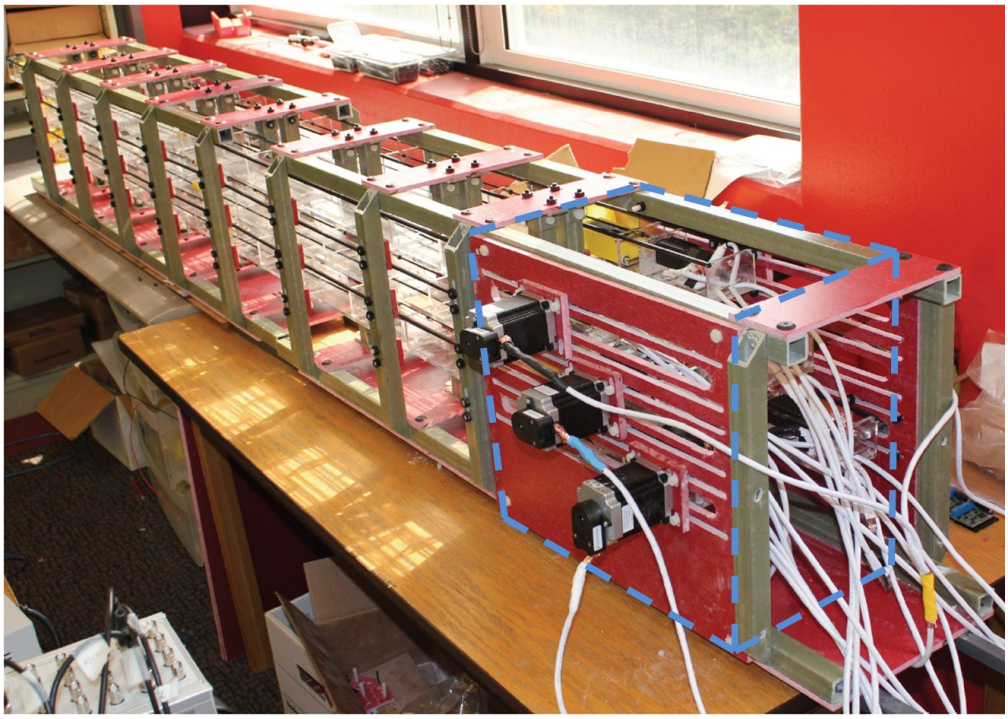

Figure 3.3.5. Structural base which is composed of fiberglass with six stages installed. The region outlined in blue is the only region containing paramagnetic

The components were fastened together using plastic rivets where possible, and aluminum rivets in sections with limited space. Brass spur gears and racks were chosen because of the strength and availability. Though non-ferrous metal components were occasionally used in this design, the design has minimal use of non-magnetic metals within 2.5 m of the MRI's magnetic center and does not use any paramagnetic materials except within the area marked in blue in the Figure. Figure 3.3.6 shows the final construction of the phantom from the end effector side with the trocar and cylindrical tubes installed.

Preliminary MRI testing was performed and published in [80] to test for noise and artifacts induced into images by the motion phantom system. A critical concern to address was the possibility of MRI imaging artifacts being introduced by the electrically

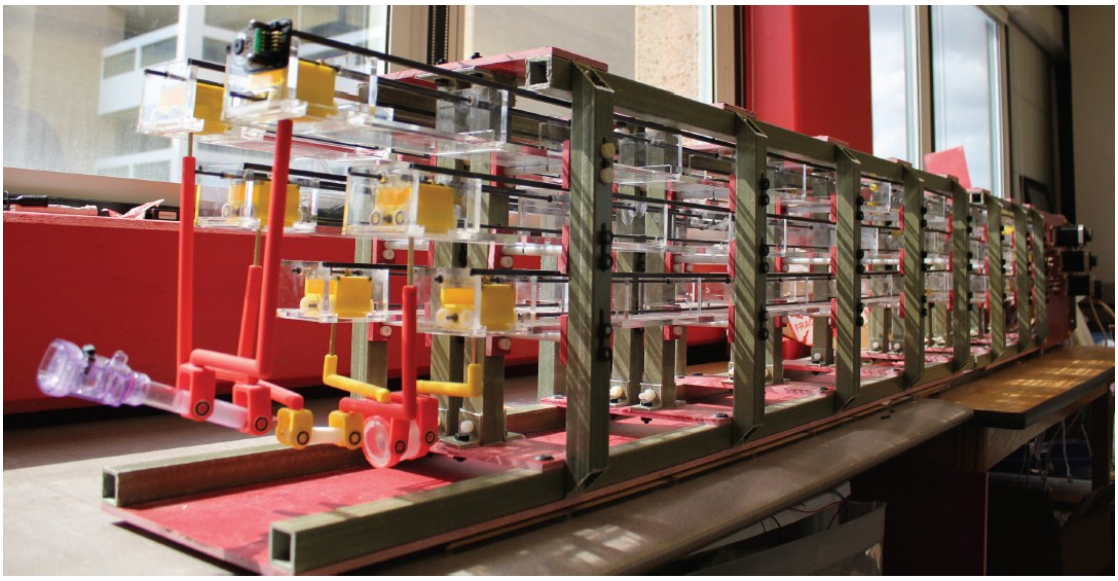

Figure 3.3.6. Final construction of motion phantom with trocar and cylindrical tubes installed to end effectors.

conductive brass and carbon fiber components which may generate eddy currents. To test the compatibility of the system, a single stage with two motors and all of its metal drive components installed was operated inside the MRI with a bottle of contrast agent as shown in Figure 3.3.7. The following conditions were tested:

1. Baseline: No foreign objects were present in the MRI room.
2. Materials: The stage was inserted into the MRI, but no cables were present, and no power was applied in order to test for noise or artifacts induced by materials.
3. Cables: The cables were installed without any power applied in order to test if the cables transmit outside noise to generate image noise or artifacts.
4. Power Idle: The phantom motors were running idle to test for artifacts from the motor power signals
5. Motion: The phantom motion was activated to test for additional artifacts from motion

Figure 3.3.7. One Cartesian stage inside the Siemens 1.5T MRI scanner

The resulting images of these experiments are presented in Figure 3.3.8 for the True FISP CINE (TF) pulse sequence and in Figure 3.3.9 for the turbo-spin echo (TSE) pulse sequence. Change in SNR due to having all materials in the MRI without electrical cables or power was calculated to be less than 1% for both pulse sequences. It was observed, however, that passing the unpowered cable through the waveguide into the room caused an SNR reduction of approximately 70% for the TF sequence and 50% for the TSE sequence. Powering the motors caused significant noise and interference with an SNR reduction in excess of 90% for each sequence. One important discovery was that grounding the shield of the motor power cable greatly improved image quality. Figure 3.3.10 shows the side by side comparison of TF images acquired with the cable shield grounded and ungrounded.

Acquired images were relatively clear to the human eye, that is the phantom boundaries were easily distinguishable. However, SNR measurements were very poor due to the broad and frequent zipper artifacts which appeared in the images. In response to the poor SNR results of the previous experiments, 100 uH RF Chokes were added in

series to each of the motor signals between the motor driver and the cable. The setup of previous experiment was repeated, and the motor cable shield was grounded in response to the previous results. Images were acquired with the motor running with and without

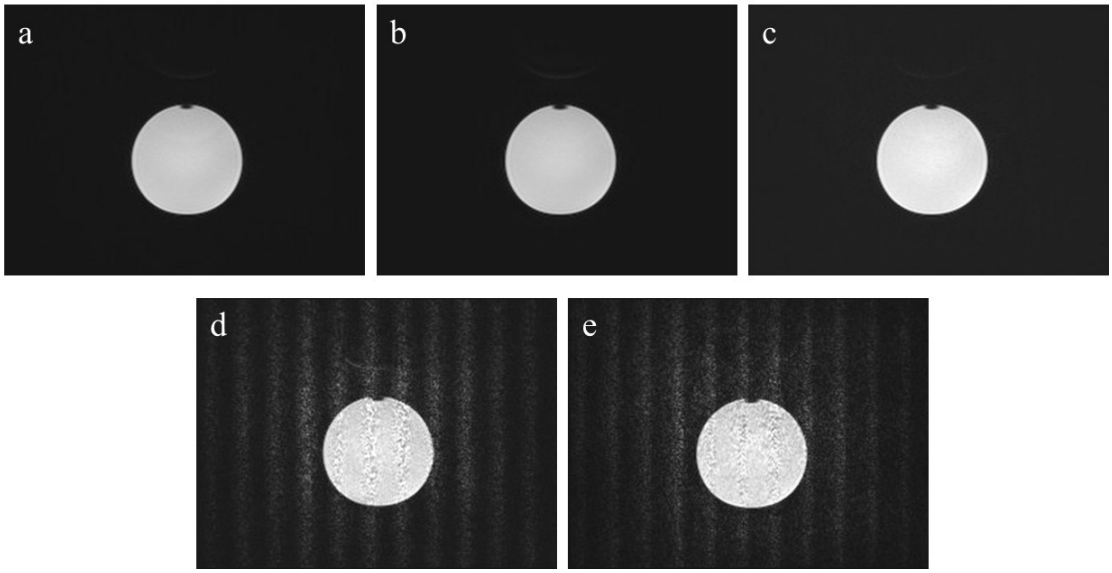

Figure 3.3.8. MRI Image Results for TFCINE under the five test conditions: a) Baseline b) Materials c) Cables d) Power Idle e) Power Running

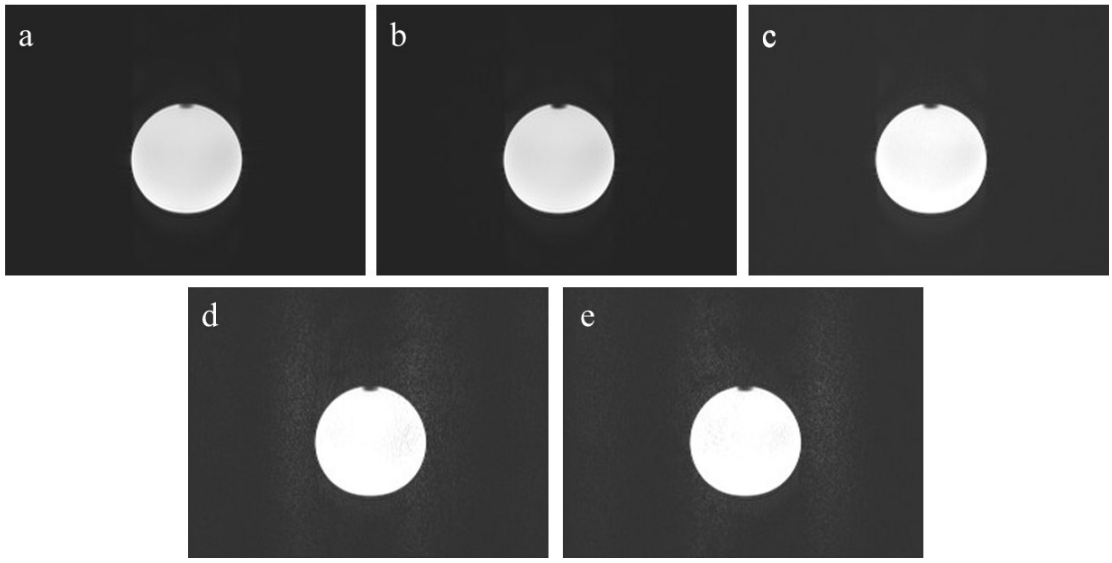

Figure 3.3.9. MRI Image Results for TSE under the five test conditions: a) Baseline b) Materials c) Cables d) Power Idle e) Power Running.

the use of the RF Chokes. Ten images were acquired in a series and the average SNR was calculated for each series. The average SNR for the baseline scan, unfiltered operation, and filtered operation were calculated to be 210, 10, and 80 respectively. Filtering the signals showed significant improvement which lead to further filtering experiments presented in Chapter 7. Side by side comparison of the baseline, unfiltered, and filtered images is presented in Figure 3.3.11.

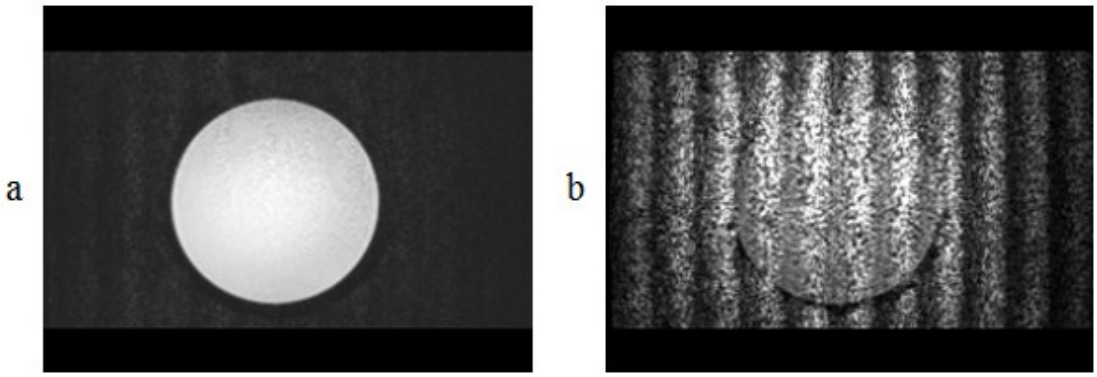

Figure 3.3.10. MRI images acquired using the True FISP pulse sequence while the shield of the motor cable was a) ungrounded b) grounded.

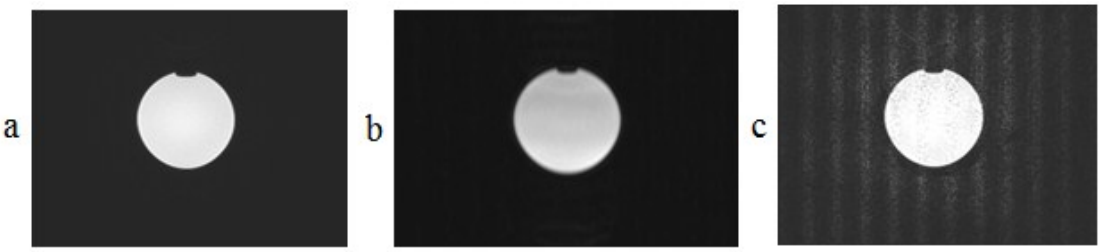

Figure 3.3.11. MRI images acquired for a) baseline scan b) filtered motor signals c) unfiltered motor signals.

3.4 Motion Control

Actuation of the phantom consists of accurately positioning the cylinder representing each cardiac landmark. Each cylinder is actuated from two opposing sides creating the need for two independent Cartesian stages. Each stage must account for three

directions of motion: horizontal, vertical, and depth, or X, Y, and Z respectively. Each stage is designed as a long structure capable of rolling on a single fixed base. This rolling motion accounts for the Z direction of actuation. On top of this rolling Z plane rest two carts which are translated together using racks and pinions to implement the X direction of motion. Mounted to one of these carts is the motor for Y motion and built into the second cart is the Y rack and pinion. Driveshafts connect both X and Y motions to their respective motors. The end result of this stage configuration is a 2.5 m long semi-enclosed rectangular stage with an end-effector capable of movement in any of the three Cartesian directions. The corresponding kinematic diagram of the described motion is presented in Figure 3.4.1 below. Each cylinder is linked to the stage via universal joints. This configuration allows the tube to translate in X, Y, and Z directions and rotate about the X axis and Y axis but not the Z axis. This configuration therefore provides five output degrees of freedom (DoF) resulting from six input DoF for each cylinder.

Each stage makes use of three motors, one for each Cartesian direction, requiring eighteen motors in total for the phantom. High torque hybrid stepper motors were used due to the size constraints including NEMA 11 stepper motors (Anaheim Automation 11Y302D-LW4) for the X and Y directions, and NEMA 23 stepper motors (Anaheim Automation 23L310D-LW8) for the Z direction. Each motor is paired with a 1024 CPR rotary optical quadrature encoder (US Digital E5). Chopper drives (Gecko 251) are used to power the stepper motors. These drivers feature fixed 10X microstepping which increases the motor precision from 200 to 2000 steps per rotation. The drivers accept step and direction command inputs and output necessary current to the motor to adjust the position accordingly. Step and direction signals are the output of a closed-loop position

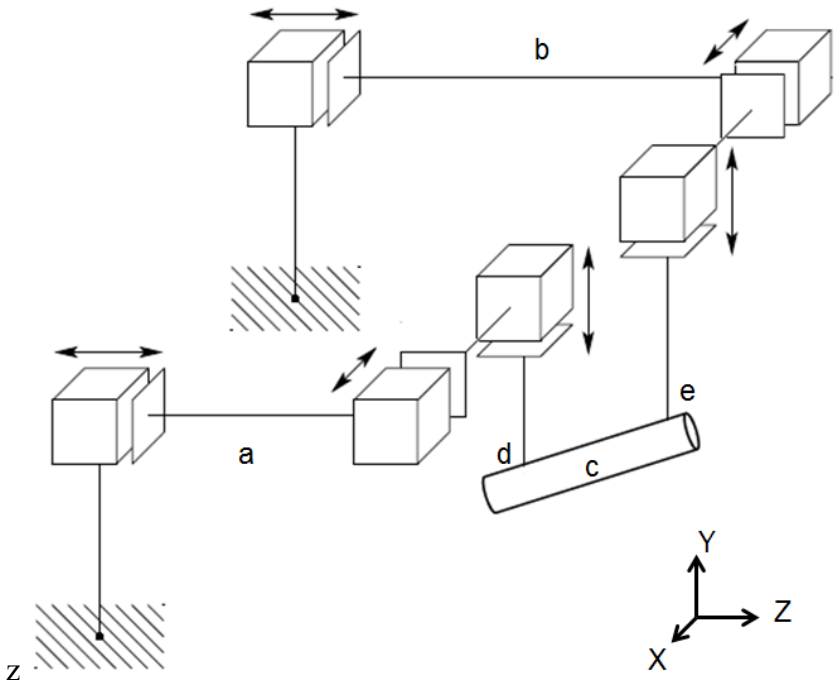

Figure 3.4.1. Kinematic diagram of two Cartesian stages (a) and (b) used to actuate one tubular structure (c) by changing the 3D position of the two points (d) and (e).

control scheme implemented on an Altera DE2-115 Field Programmable Gate Array (FPGA) (TerasIC, Taiwan). This FPGA was used in place of the multiple microcontrollers proposed in our previous work [46] because it can be programmed to perform control calculations and decode quadrature encoders for all motors in parallel on a single device. The actuated phantom can mimic operator defined motions, as well as replicate the motion of the heart extracted from cardiac dynamic imaging. In those studies, we investigated the actuated phantom with the motion pattern of the human beating heart extracted from CINE MRI data of healthy volunteers. Datasets containing 25 points were extracted for each one of 6 points to be actuated. To simulate a heart cycle at 60 beats per minute, these 25 points are repeated at even intervals over 1 second. An example position profile is shown in Figure 3.4.2 below. The motor velocity required between each point

could most easily be approximated by the simple linear approximation to give the velocities of Figure 3.4.3.

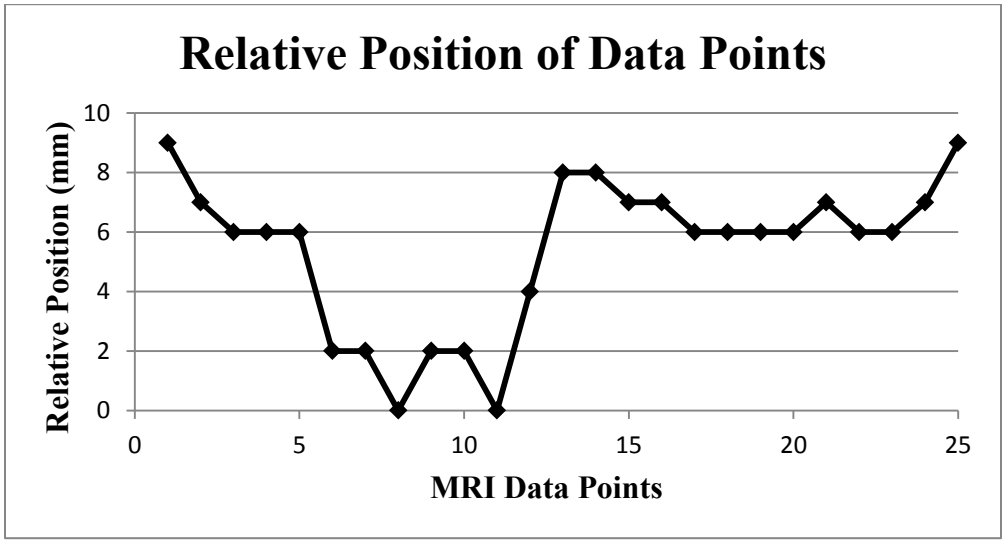

Figure 3.4.2. Relative position of the 25 points obtained from MRI data.

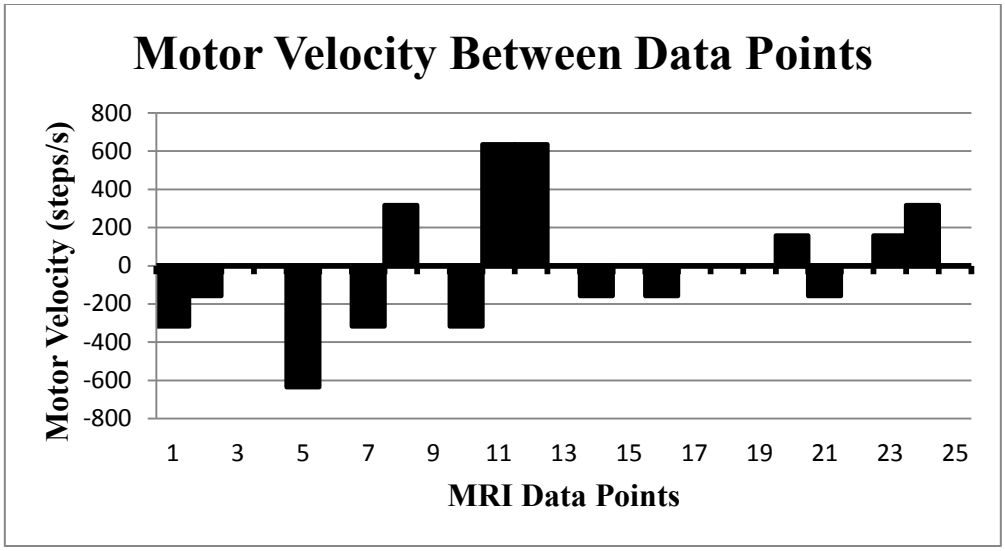

Figure 3.4.3. Required motor velocity between points using a linear approximation.

Analysis of the heart motion profiles demonstrated that there are between 4 and 16 direction changes per second with a maximum change in velocity of 960 pulses per second. Even though stepper motors are known to have high open loop accuracy, our preliminary experiments demonstrate that they are incapable of tracking these motions. The linear approximation is therefore an insufficient approach for calculating velocity

and an algorithm which provides slower acceleration is required. A controller was designed to command a trapezoidal velocity profile to the motors as well as provide PID feedback control. The full details of the controller design are presented in the next chapter.

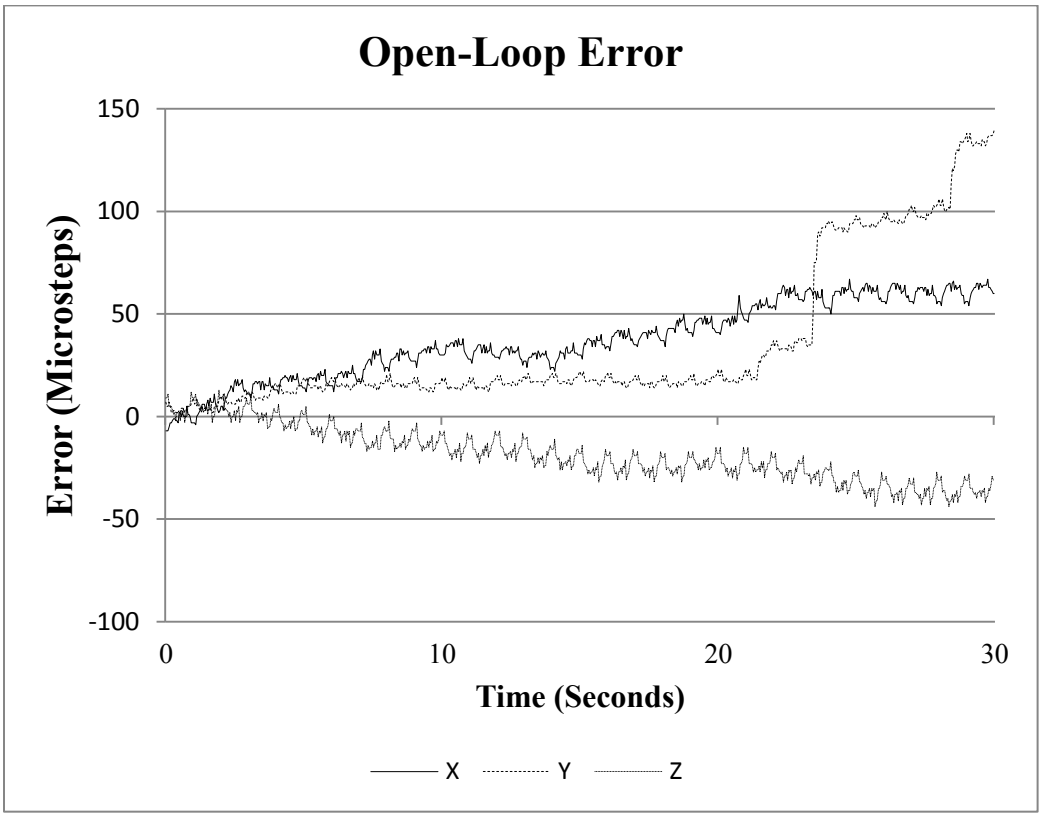

Figure 3.4.4. Open-loop tracking performance over 30 seconds for one Cartesian stage with three axes X, Y, and Z.

Since each phantom Cartesian stage is a two meter long mechanical transmission system, significant load is presented to the motors through friction and inertia of the mechanical transmission itself even without considering the load on the end effectors or external disturbances. Without the use of open-loop control, the motors were unresponsive to the commanded trajectories because of the step-out condition. Figure 3.4.4 presents the tracking performance due to open-loop control. It can be seen from the

figure that the trajectory tracking error begins to diverge immediately after the start of the motors. The system is therefore unstable without the addition of closed-loop control.

The closed-loop motor controller was applied to each axis and validated by recording the tracking performance for each of the X, Y, and Z directions of a Cartesian stage as shown in Figures 3.4.5-3.4.7. The demonstrated tracking performance is excellent regardless of the axis recorded. Each axis has its own unique trajectory as well as its own dynamics such as friction and inertia. Each trajectory, although relatively small in amplitude features several direction changes during the one second period. Submillimeter tracking performance is achieved for all three axes.

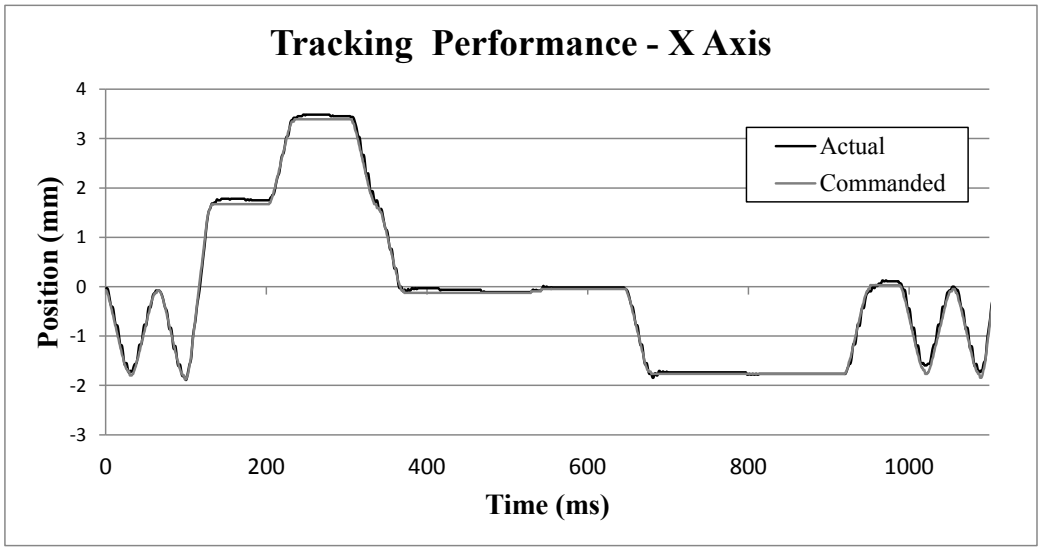

Figure 3.4.5. Closed-loop tracking performance for the X axis of the Cartesian stage

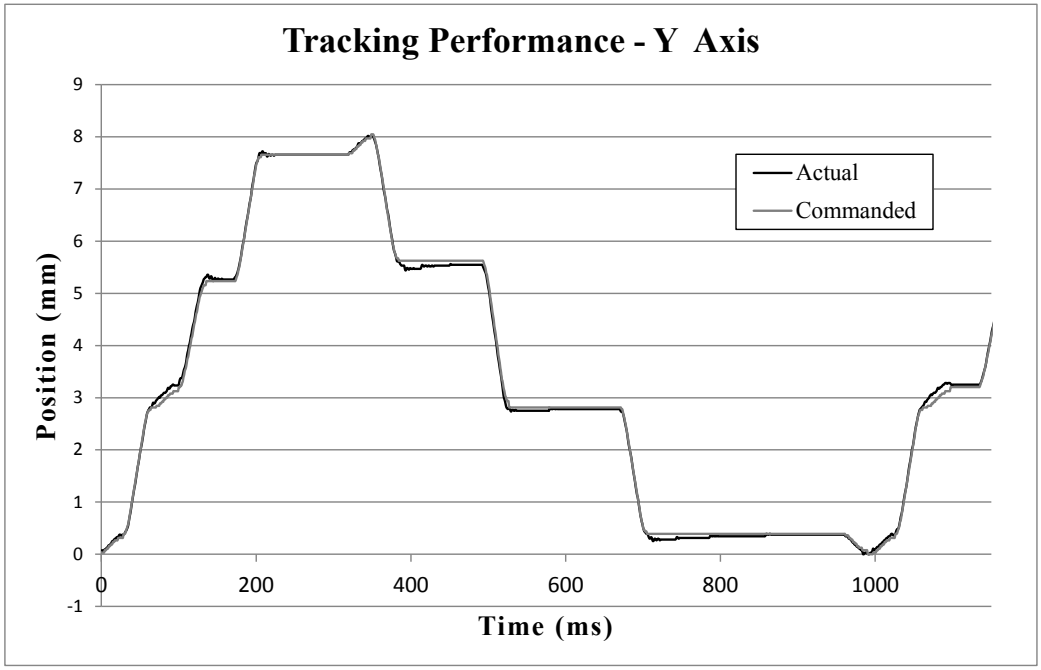

Figure 3.4.6. Closed-loop tracking performance for the Y axis of the Cartesian stage.

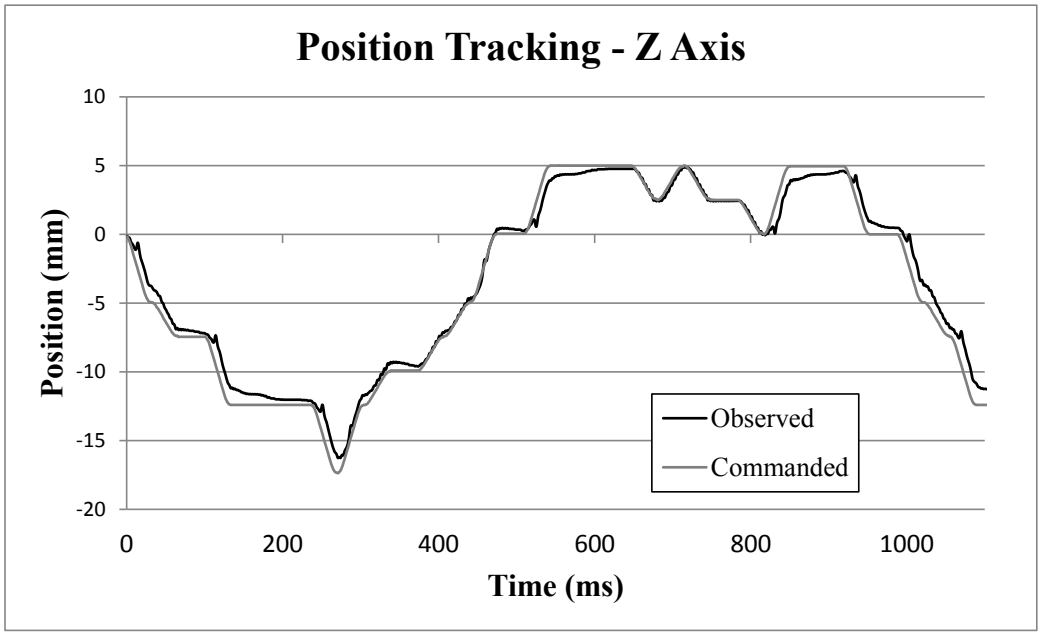

Figure 3.4.7. Closed-loop tracking performance for the Z axis of the Cartesian stage.

4. FPGA Based Stepper Motor Controller

4.1 Overview

The following FPGA based stepper motor motion controller was developed in order to meet the needs of the actuated Phantom of Chapter 3 which simulates the high speed anatomical motion of the human heart. Stepper motors use electromagnetic properties to provide discrete and predictable motion. However, in high acceleration conditions the dynamics of the stepper motor render it unpredictable and ineffective. The resulting condition referred to as step-out may cause the motor to skip miss steps, or in worse cases rotate backwards, or remain completely still. A controller is required to control the acceleration of the motor to prevent the step-out condition from occurring. Closed-loop feedback control was used to ensure positional accuracy and provide closed-loop tracking capabilities. The open-loop and closed-loop control will be combined as a hybrid control design and implemented on the FPGA for performance. The following subsections 4.2 – 4.5 will give the details of the implementation and results will be given in subsection 4.6. The design principles of this controller were modified for use with the SMFT actuation method as discussed in 4.7.

The components used for the control of the hybrid stepper motors include an FPGA (Altera DE2-115 Development Board), chopper drives to drive the motors (Gecko 251), hybrid stepper motors (Anaheim Automation), and rotary encoders (US Digital E5) as shown in the block diagram of Figure 4.1.1. The algorithms presented within this section are general and not specific to any one piece of hardware i.e. any model of FPGA, chopper drive, hybrid stepper motor, or encoders could be used with little or no modification as they are standard equipment used in industry.

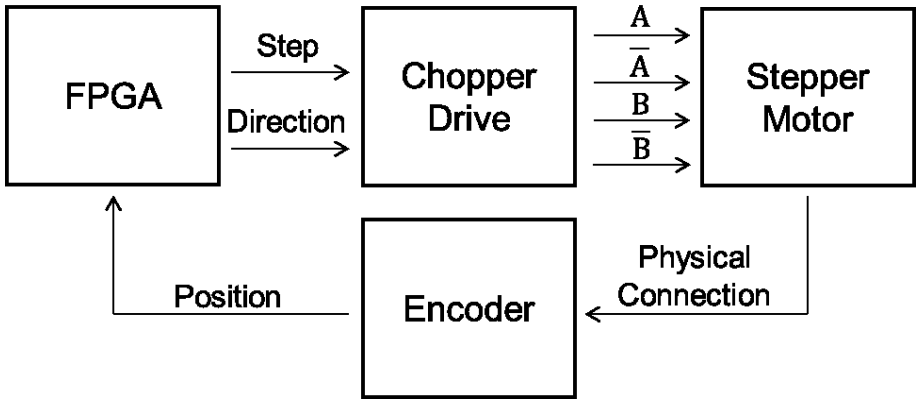

Figure 4.1.1. System Hardware Diagram

Stepper motor drivers commonly accept two digital inputs step and direction which are used by the driver's internal hardware to command the proper currents to the motor poles to adjust the position accordingly. A rising edge on the step input corresponds to one set or microstep of motor actuation depending on the driver settings. Although these types of drivers feature easy operation, they do not measure or control the internal dynamics of the motor. They also do not accept any form of feedback since stepper motors can often be used in open-loop mode. Several p are reviewed in Chapter 2 on the closed-loop control of stepper motors, but none of the state feedback data required by those control algorithms is available through commercial drivers. Feedback available in a typical industrial stepper motor control loop is limited to position and its derivatives through the use of rotary encoders. Therefore, the only available method of optimizing the motion of the stepper motor is to control the timing of the input pulses given to the driver.

4.2 Selection of Digital Hardware

All aspects of the stepper motor controller were designed and implemented using Field Programmable Gate Array (FPGA) technology as a purely parallel solution to high-

speed multi-axis control. Unlike microcontroller or PC based implementations, the motion control core designed here can be replicated multiple times on a single FPGA without coupling performance. The factors of performance, cost, and development time were considered in the selection of a suitable platform for control. Selection was performed from four potential hardware platforms: a computer, microcontroller, Field Programmable Gate Array (FPGA), or Application-Specific Integrated Circuit (ASIC). Each one has its own merits and limitations and our final selection was to weigh the different features of those options (reviewed in Table 4.2.1 below.)

TABLE 4.2.1
COMPARISON OF DIGITAL HARDWARE PLATFORMS

	Computer	Microcontroller	FPGA	ASIC
Architecture	Processor	Processor	Freeform	Freeform
Architecture Configurability	Fixed	Fixed	Reconfigurable	Fixed
Hardware Interfacing	Bus	Direct	Direct	Direct
Parallel Limitation	Processing cores	Processing cores	Logic Elements	Size and cost
Operating Frequency	1 Ghz – 4 Ghz	4 Mhz – 1.2 Ghz	50 Mhz - 800 Mhz	Hardware Defined
Development Time	Shortest	→		Longest
Real-Time Accuracy	Worst	→		Best

Computers and microcontrollers are the most commonly used platforms for a digital system because of familiarity and the structured architecture that a processor system provides. Most engineers, regardless of discipline, are capable of converting simple ideas to code of some programming language. FPGA's, however, have no inherent architecture to process instructions. Though it is possible to synthesize a processor architecture within an FPGA, for the purpose of this comparison, FPGA refers

to a from scratch FPGA development. While the FPGA's lack of a predefined architecture adds to development time, it gives opportunity to greatly enhance the performance capabilities as a real time system. The ASIC design process is similar to that of the FPGA except that once an ASIC is manufactured it cannot be reconfigured. The advantage of ASIC though is that it can be cheapest to manufacture in large quantity since it is the least generic solution.

A digital control system requires hardware interfacing to connect the inputs and outputs of the controller to the physical world. Computers have no native hardware interfacing which make them the poorest choice as a real-time system. Hardware interfacing must be done through external busses such as PCI or USB which have very high clock-cycle overhead. Microcontrollers have hardware interfacing logic built-in and data can be read through the processor directly. Due to this advantage, a microcontroller in a digital control system can achieve the same results as a computer with a much lower clock frequency. In an FPGA or ASIC design there is no such architecture so external signals can be used directly in combinational or sequential logic. This is a major advantage in real time performance.

Processors, whether in a computer or microcontroller, operate in a load store architecture processing one instruction per clock cycle per processing core. All data is loaded through bus networks which take many clock cycles to pass data. This architecture is designed to be a robust handler for all scenarios of logic and operations. It is ideal for generic applications such as desktop computing. However such a generic implementation is full of bottlenecks and even though a processor may have a clock frequency in gigahertz, the effective throughput of data is significantly slower. For example simple

addition operations require the processor load the data from memory through the bus, perform the operation, and store the data back to memory through the bus. Complex operations such as division or operations on multiple words of data will take even longer to complete. In an FPGA or ASIC implementation data can be stored directly in registers, and hardware can be dedicated for this operation so that the arithmetic can be performed using combinational logic or sequentially in one clock cycle. The engineer of course still has the option of introducing memory or pipelining to the system to optimize space in the FPGA, but the architecture is part of the system design.

For optimal performance, it is desirable to compute independent calculations in parallel. The first cardiac phantom system has 18 motors. If all 18 motors are interfaced and controlled using one computer or processor, interrupts and overhead from the timing processes and hardware interfacing would significantly reduce the real time performance of the system. To provide parallel processing capabilities, some computer and microcontroller processors have multiple cores. However, current technology limits the number of cores available per processor and therefore the use of a processor for parallel computing is not ideal. Therefore, multiple processors would be required, communicating with some main processing unit which would provide an operator interface and keep them in sync. However, if an FPGA or ASIC controller is designed efficiently enough, all of the controller units and master unit can be contained in one silicon device to provide more efficient, less complex, lower cost parallel computation.

Based on the factors discussed above, the FPGA was chosen as the target platform for this control scheme. Implementing the controller on the FPGA offers the most flexibility and configurability. The implementation can be designed to maximize parallel

computation in order to provide the best real-time accuracy. The negative effect of this decision is that completing this design on the FPGA requires the longest development time.

4.3 Open-loop Control

Although stepper motors are open-loop stable, their operation is sensitive to the dynamics which occur within the motor during operation. By switching the current direction which effectively changes the orientation of the magnetic fields of the motors poles, the rotor can be "stepped" sequentially through a fixed number of steps to be positioned or perform rotation. Harmonic vibrations and ringing are observed effects from the dynamics of this stepping process. As the rotor reaches its new position, inertia will push the rotor past the desired position until the force of the magnetic field brings the rotor backward and past the desired position again. This oscillation, or ringing, will occur until natural damping allows the rotor to finally settle at the equilibrium point as shown in Figure 4.3.1 [82]. Problems occur if a new step is commanded before the ringing has settled. In this case, unpredictable motion known as step-out may occur. Step-out may cause the rotor to overshoot its next step, fail to step at all, or even move in the wrong direction.

The amplitude and settling time of this ringing phenomenon is dependent on the inertia of the motor, the inertia of the load, and the strength of the magnetic field at each pole. It is desired to control this dynamic to keep this ringing condition from disrupting the motion of the motor, however since the motors and hardware do not provide adequate feedback to measure this phenomena, active damping cannot be performed. Therefore, open-loop control should be used to try to prevent step-out from happening.

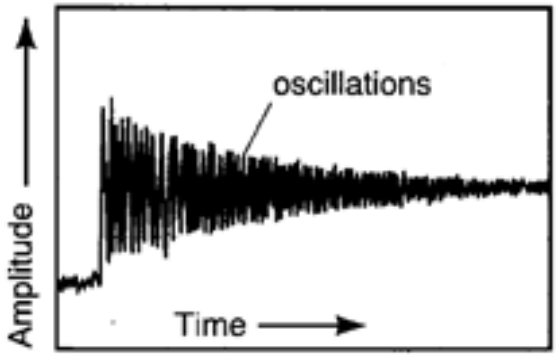

Figure 4.3.1. Ringing which occurs after each step can lead to step-out.

Chen et al. [83], amongst other groups, have experimented with three velocity profiles: The S-curve, trapezoidal, and parabolic profiles. Figure 4.3.2 [83] shows the shape of these profiles and their effective position path; The parameter β, used in the figure, corresponds to the rate of acceleration. The S-curve accelerates slowly during low velocity and acceleration increases as velocity increases. This is the most optimal acceleration to the motor, but the resulting position tracking is non-linear so if linear interpolation is desired this method is the least suitable. The parabolic profile provides high acceleration during low rpm with a decreasing acceleration as velocity increases. This velocity profile yields very little improvement over the linear velocity approximation and is therefore unsuitable for our rapid motions. However, the corresponding position tracking is excellent. The trapezoidal profile provides constant acceleration which is not as optimal as the S-Curve, however, it was selected because it gives performance which falls between the S-curve and parabolic profiles. If the acceleration is chosen properly, the trapezoidal profile will provide ample velocity feedforward to reduce ringing, while maintaining decent position tracking. The trapezoidal profile is ideal for use on the FPGA because the calculation is simple in complexity and therefore space efficient.

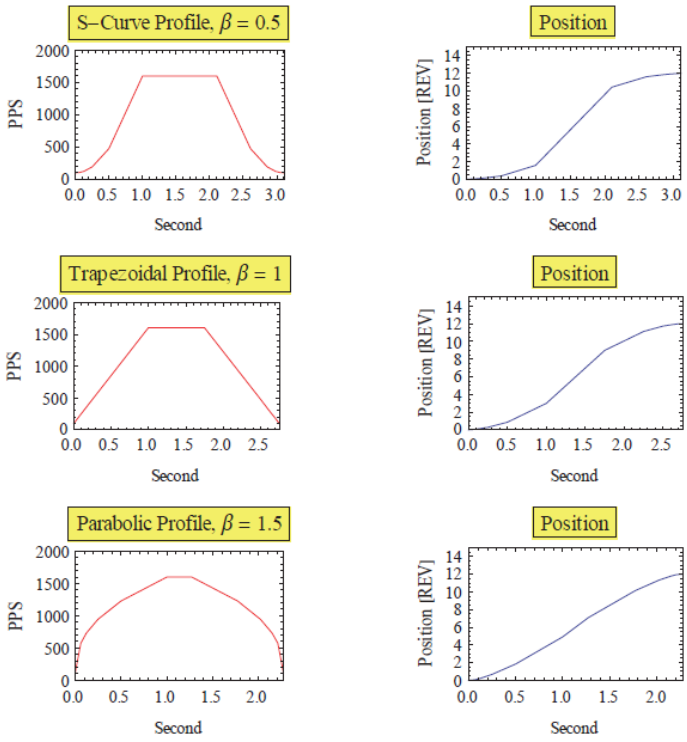

Figure 4.3.2. Position profiles (right) correspond to the three velocity profiles (left). S-Curve, trapezoidal and parabolic are shown. β corresponds to the rate of acceleration.

4.4 Hybrid Closed-loop Control

The velocity profile alone provides enough accuracy for most applications. However, the rapid motions, inherent inertia, and desired submillimeter accuracy of this system necessitate closed loop control. With the current gear ratios of the motion phantom, one full step equates to $1/6^{th}$ of a millimeter. Therefore, to claim submillimeter accuracy this system must maintain less than six full steps of error. To guarantee accuracy, as well as provide for error correction under load, velocity based feedforward control is used in conjunction with position based PID feedback control. The general control model presented in Figure 4.4.1 below was implemented and replicated on the FPGA to create the multi-axis controller.

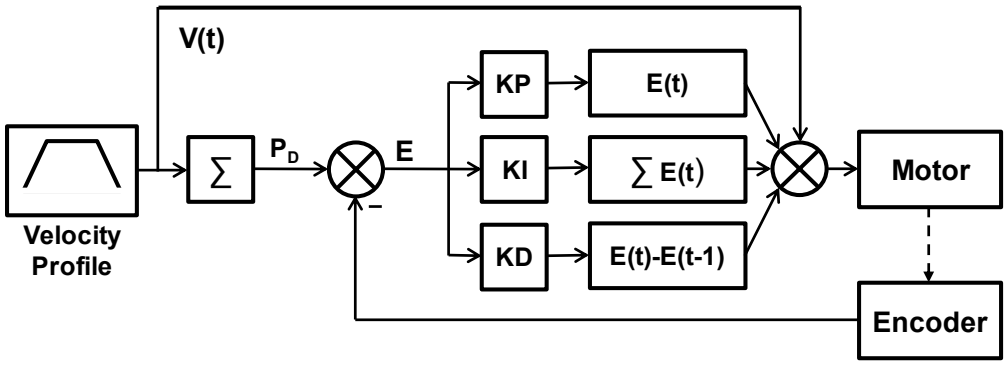

Figure 4.4.1. Block diagram of the implemented control system. Feed-forward velocity control is used in conjunction with PID closed-loop control. P_D and E refer to desired position and error respectively.

The current value of the velocity profile V(t) is used as feedforward control to the motor. The velocity profile and desired position (P_D) are calculated on the fly so that the error (E) can be calculated using the encoder data of the previous iteration. The desired current velocity of the motor according to the velocity profile is summed with a result of the error correction factor which is given by the PID control law shown in the equation where KP, KI, and KD refer to tunable constants for the proportional, integral, and derivative terms respectively.

Error Correction Factor

$$= \mathrm{KP} * \mathrm{E(t)} + \mathrm{KI} * \sum E(t) + \mathrm{KD} * (\mathrm{E(t)} - E(t-1)) \qquad (4.4.1)$$

4.5 FPGA Computational Core

The control methods previous described were designed to address the constraints of the desired system output and motor dynamics. Transforming these control theories to an FPGA implementation imposes further constraints. In particular, speed and area are two design constraints which usually counteract each other in FPGA design. Speed is not only limited to the device clock speed, but by how many clock cycles are required to

generate results. Area refers to the amount of logic elements required by a design. Each FPGA has a limited number of logic elements available depending on the model.

To make a circuit faster usually requires more area; likewise, to reduce the area of some hardware, pipelining is usually implemented at a cost of speed. However, both speed and design are crucial to this design. In order to track the fast motions of the heart data, we want to sample as quickly as possible, but to fit 18 controllers on one device, area must be optimized in every way possible. To avoid the need for pipelining in this design, only fixed point numbers were used. This design decision influenced every calculation made in this design because all calculations had to be kept so that the numerator is safely larger than the denominator to minimize truncation error.

Division operations in this first implementation were performed using Altera's combinational lpm_divide megafunction which is an intellectual property (IP) core given as part of the Quartus development suite. The Altera megafunction is capable of performing division in only one clock cycle. However, the synthesized dividers take thousands of logic elements each. Shift registers can be used to divide with minimal expense in logic elements, but only for division by factors of two. Multiplication operations were performed using the lpm_mult megafunction IP core which enables the use of the FPGA's 532 built-in hardware multipliers instead of using logical elements. As a result, multiplication is also performed in a single clock cycle, but the amount of hardware multipliers available varies by FPGA model. With these facts in mind, equations were carefully composed to use as few division operations as possible.

The architecture of the designed controller (Figure 4.5.1) is hierarchical. A master module interfaces all external signals. Switches, buttons and LEDs are handled directly in

the external hardware module but encoder signals and controller outputs are propagated down to the motion control module. Serial communication is handled by a dedicated module just under the master module. The EEPROM allows a position trajectory, and tuning constants to be stored in memory so that the system can be operated free of the PC. The remaining control functions are all located within the motion control module with the exception of the shared clock which is used by all motion control modules to ensure that the motions between modules all occur in synchrony.

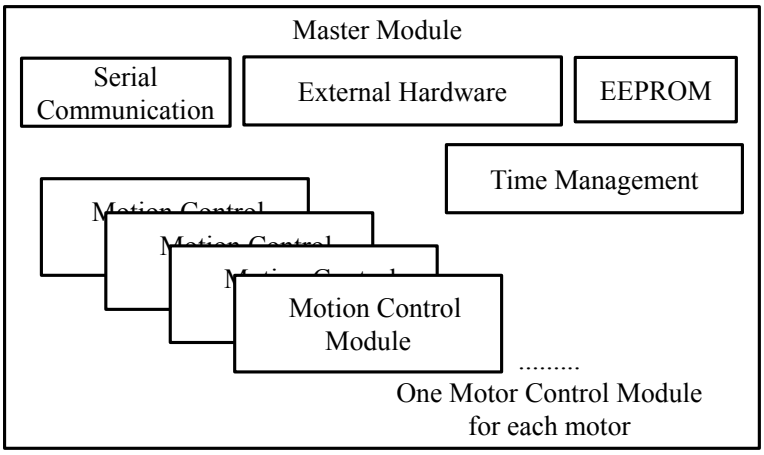

Figure 4.5.1. High level system architecture for FPGA implementation of the hybrid controller.

The time management block consists of a counter which raises a flag at each time cycle Δt and also stores the elapsed time in a register named TimePassed to keep track of the elapsed time as required by the desired position calculations in the motion control module. Within the motion control module, three main calculations are required: the velocity profile calculation, desired position calculation, and error calculation as organized accordingly in Figure 4.5.2.

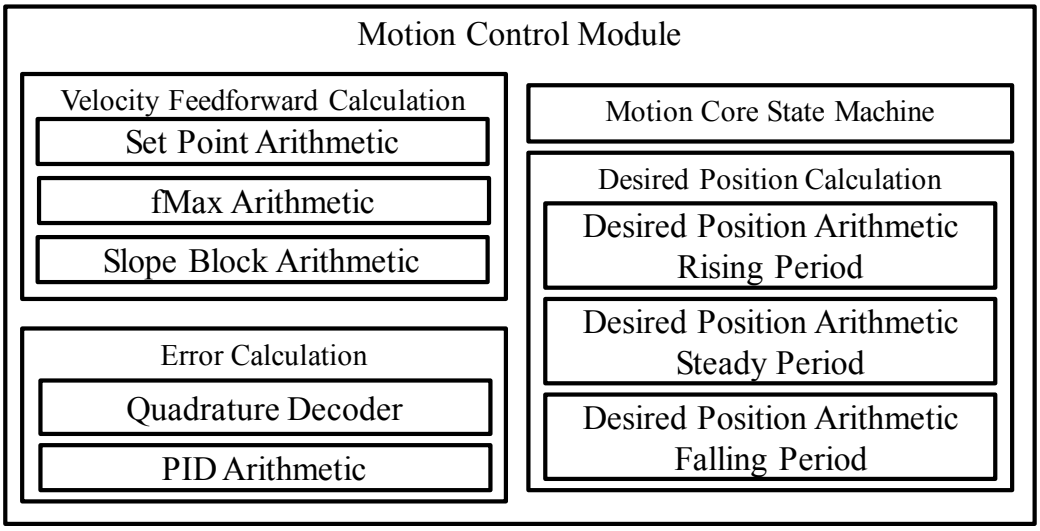

Figure 4.5.2. Subblocks within the Motion Control Module.

The velocity feedforward calculation block contains the arithmetic necessary to calculate the current velocity set-point at each sample time Δt along the trapezoidal velocity profile. The sample time Δt is defined as

$$\Delta t = \frac{\text{ClockSpeed}}{(TPS * n) \ll LogSamples}, \tag{4.5.1}$$

where TPS refers to the amount of trajectory points per second, ClockSpeed is the speed of the FPGA clock, n is a scaling factor to adjust the length of time occupied by the rising and falling states, and LogSamples is defined as 2^m where m is the number of samples per period T. Storing the data as LogSamples in EEPROM saves space and also enables the use of shift registers in all calculations rather than multipliers or dividers, but the number of samples must be a multiple of 2.

The velocity profile shown in Figure 4.5.3 demonstrates the three states: rising state, steady state, and falling state, as well as the significance of the term n. The term n is the number of states of equal time duration which will occur within the profile. Regardless of the value of n, there will always be one rising and one falling state.

Therefore, a higher value of n, will lead a longer steady state time, and therefore a shorter time duration for the rising and falling states.

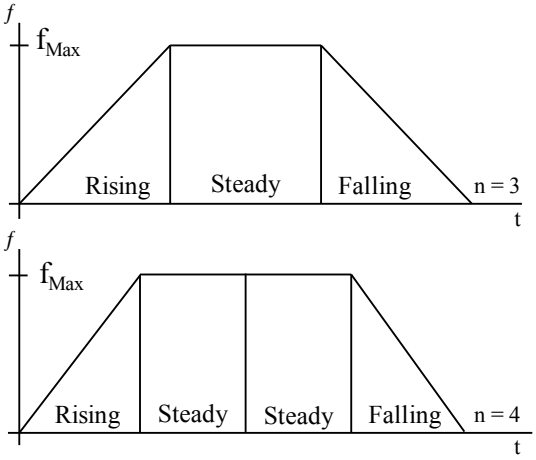

Figure 4.5.3. States within trapezoidal profile. Adjusting the number of states n modifies the time duration ratio between rising/falling time and steady time.

The arithmetic of the velocity feedforward module is divided into three arithmetic modules: set point arithmetic, f_{Max} arithmetic and slope block arithmetic. The velocity set-point provided to the motor changes for every update time Δt during the rising and falling periods and is held constant as f_{Max} during the steady state. To reduce calculations a simple add/subtract module was used to add or subtract a fixed value to the set point to generate the rising and falling slopes of the trapezoid. The fixed value referred to as SlopeBlock is calculated simply as

$$SlopeBlock = fMax \gg \text{LogSamples}. \tag{4.5.2}$$

The set point arithmetic, depending on the state, is described by

$$SetPoint(t) = \begin{cases} SetPoint(t-1) + SlopeBlock & \text{Rising State} \\ fMax & \text{Steady State} \\ SetPoint(t-1) - SlopeBlock & \text{Falling State} \end{cases} \cdot \tag{4.5.3}$$

where the value f_{Max} is the maximum frequency of the velocity profile. This is also the velocity set-point during the steady state. This velocity can be calculated as

$$\mathrm{fMax} = \frac{\mathrm{TargetDistance} * \mathrm{n} * \mathrm{TPS}}{\mathrm{n} - 1}, \tag{4.5.4}$$

where TargetDistance refers to the desired position of the motor in microsteps after the completion of the velocity profile.

The effect of adding and subtracting the slope block to create the rising and falling slopes is shown by the resulting velocity profile is shown in Figure 4.5.4 with n=3. Due to fixed point truncation error in the slope block calculation, the set-point will not quite reach f_{Max} during the last cycle of the rising period and likewise the set-point will not be exactly zero at the last cycle of the falling period. Fixed point errors such as these will be corrected by the PID controller.

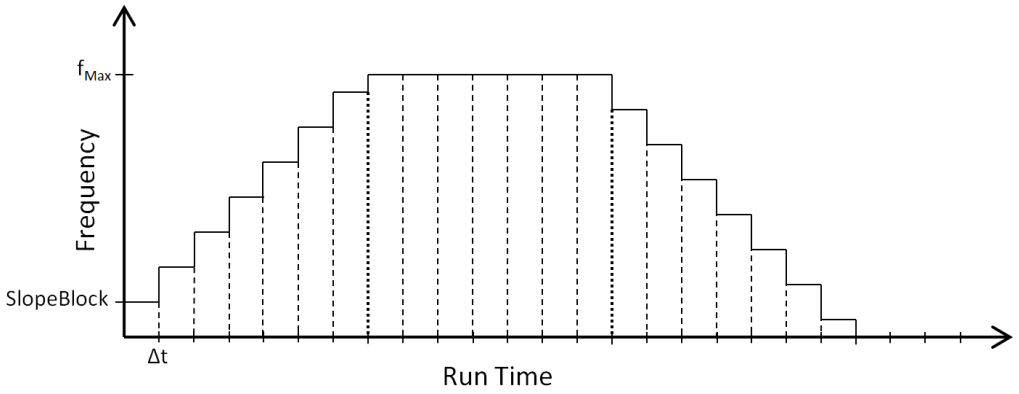

Figure 4.5.4. Discretized trapezoidal profile.

The desired position block contains the rising, steady, and falling desired position arithmetic blocks which are used to precisely calculate the desired position of the motor at the current point in time using dedicated hardware. The desired position at any given time t is given as follows depending on the state. For the rising state,

$$Desired\ Position =$$

$$PositionSave + \frac{fMax\ \left[\frac{1}{s}\right] * t^{\,2}[cc^2] * FPS\left[\frac{1}{s}\right] * n}{Clock\ Speed^2\ [\frac{cc^2}{s^2}]}. \tag{4.5.5}$$

For the steady state,

$$Desired\ Position =$$

$$PositionSave + \frac{(t\ [cc] - TimeSave\ [cc]) * fMax\ \left[\frac{1}{s}\right]}{Clock\ Speed\ [\frac{cc}{s}]}. \tag{4.5.6}$$

For the falling state,

$$Desired\ Position = PositionSave +$$

$$\frac{\left(\frac{Clock\ Speed\left[\frac{cc}{sec}\right] - t\ [cc] * FPS\left[\frac{1}{s}\right]}{Clock\ Speed\left[\frac{cc}{sec}\right] - TimeSave\ [cc] * FPS\ \left[\frac{1}{s}\right]} + fMax\ \left[\frac{1}{s}\right]\right) * (t\ [cc] - TimeSave[cc])}{Clock\ Speed\ [\frac{cc}{sec}]}. \tag{4.5.7}$$

PositionSave is a register which accumulates the current desired position at each state change until the controller is reset. It is updated per state change rather than for each new point in the trajectory to reduce calculation. TimeSave is a register which saves the TimePassed register data at each state change. Storing the register data is more efficient then calculating the time which occurred during previous states. These values are illustrated by Figure 4.5.5 below.

The desired position calculation can be used to calculate error from the accumulated encoder as

$$Error = Desired\ Position - Accumulated\ Encoder\ Value\ , \tag{4.5.8}$$

where the accumulated encoder value is calculated within the Error Calculation block. Also calculated within this block is the PID correction factor. For PID calculation, the

sample period was considered to be one clock cycle so the simplified digital PID form was adjusted as follows,

$$Kp * Error + KI \sum Error + KD * (Error - Error\ Last). \quad (4.5.9)$$

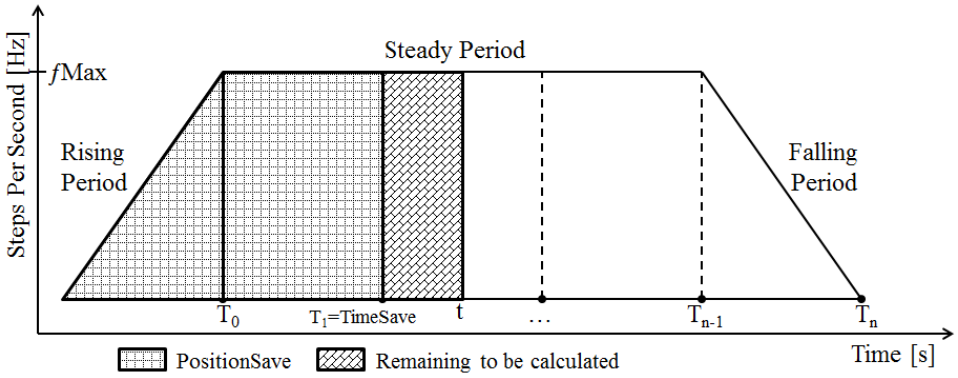

Figure 4.5.5. Demonstrating the implementation of the position save register.

The controller can now be synthesized using the arithmetic logic of the Motion Control block to generate all of the required values. The overall synchrony and control of the states is performed using a state machine of five states: waiting, sample rate determination, rising, steady, and falling states (Figure 4.5.6). The waiting state simply waits for the next trajectory point to be loaded and a flag to be raised indicating that the data is ready. The sample rate determination state is to protect from oversampling. In the case that the sample rate Δt is sufficiently fast compared to the amount of steps in the target distance, the SlopeBlock calculated in (4.5.2) could return a zero result. To avoid this the SlopeBlock is checked and sampling rate is adjusted until the SlopeBlock is larger than zero. During the rising, steady, and falling states the appropriate registers are updated from the latest values produced by the arithmetic blocks to generate the desired set point velocity.

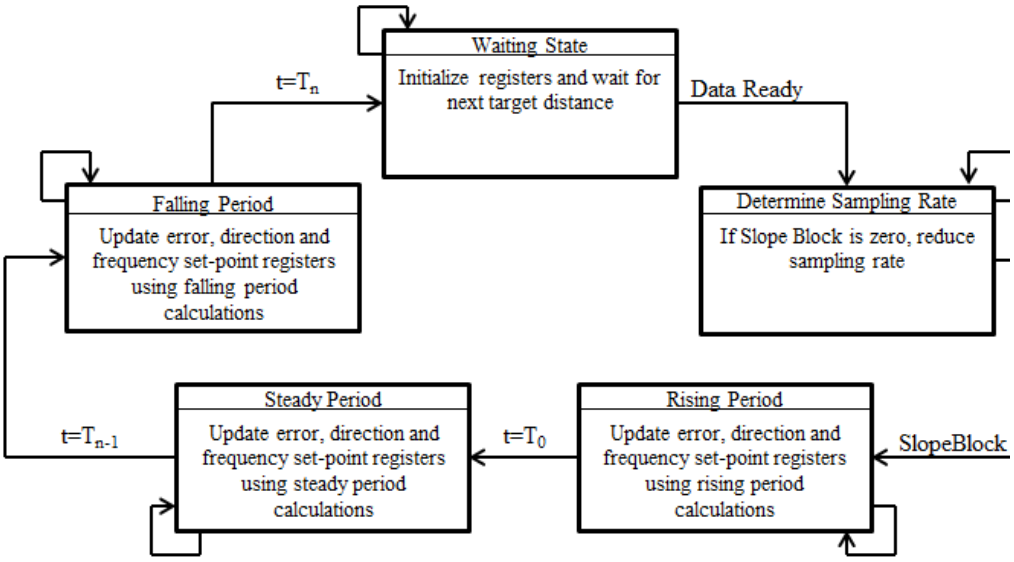

Figure 4.5.6. Motion core state machine.

4.6 Preliminary Results

Hardware utilization per module is shown in Table 4.6.1 below in terms of combinational functions, registers, and DSP elements. Combinational functions contain logic which will be stored in adaptive look-up tables (ALUT) in the FPGA circuitry. Dedicated registers refer to strictly storage units which are used to store a value. During hardware synthesis, combinational functions and dedicated registers are stored in adaptive logic modules (ALM) which each can hold a fixed amount of combinational functions and dedicated registers. Therefore, the final storage size of the synthesized hardware will be in the range between the total number of combinational functions and the sum of combinational functions and dedicated registers, depending on how many of the registers are packed together with combinational functions inside of the ALM. Multiplication performed by the Altera megafunction IP core is performed in digital signal processor (DSP) hardware rather than combinational functions to save space. DSP

elements in the table refer to this utilization. The Terasic DE2-115 development board used in this experiments contains the Altera Cyclone IV EP4CE115F29C7N which features 114,480 ALMs, and 266 DSP elements. Since it is desired to control 18 motors simultaneously, 18 motion core modules are required, as well as one EEPROM, serial communication, and time management block. According to the data in the table, control of 18 motors would require 211524 ALMs in the worst case, that is without packing combinational functions and dedicated registers together and without compiler optimization of sharing some logic between the 18 motion core modules. Also 522 DSP elements would be required. From this data it is concluded that two of the current FPGA are required for simultaneous control of 18 motors. However, a pipelined implementation with a smaller footprint is presented in the next section which reduces the size of the motion control module.

TABLE 4.6. 1
RESOURCE UTILIZATION BY MODULE

Module	Combinational Functions	Dedicated Registers	DSP Elements
Motion Core	11338	363	29
EEPROM	353	156	0
Serial Communication	175	151	0
Time Management	37	34	0

4.7 Further Optimization

Modifications were performed to the stepper motor controller to allow it to be used more generally for the control of the stepper motors used in the projects of the following sections. First of all the ability to take motion commands on-the-fly through

serial was added. Second, more tunable parameters were added including rise time, target time, and low level sampling frequency, in nanoseconds, can be sent as variables. All time operations are performed in nanoseconds now instead of milliseconds. Third, the largest modification, is the use of a single shared arithmetic pipeline for most calculations. The largest consumption of hardware area in the previous design was the dividers, which could calculate division in only one clock cycle. These six dividers consumed a total of 9,171 combinational functions in the previous design. Two serial dividers, which require one clock cycle of operation for each bit in the dividend, were used in place of these six dividers. The addition of this new arithmetic pipeline also requires the implementation of new states in the state machine. Together these modifications greatly reduce the hardware utilization requirements without noticeable effect on performance.

The state machine, which contains eight states, is described in Table 4.7.1 below. After the wait state, four calculation states are required to calculate values that will be used for calculations taking place during the rising, steady and falling states. Rise time (T_{Rise}) and target time (T_{Target}) are converted from nanoseconds to clock cycles in states Calc_RT and Calc_TT respectively. The maximum velocity commanded during the steady state of the trapezoidal profile is calculated during the Calc_f_{max} state as follows where P_{Target} refers to the target position.

$$f_{max} = \frac{P_{Target}[steps] * Clock\_Frequency\ [\frac{cycles}{sec}]}{T_{Target}[cycles] - R_T\ [cycles]}. \tag{4.7.1}$$

After the calculation of f_{max} is completed, the acceleration, or slope $\frac{\Delta f}{\Delta t}$ of the trapezoid must be determined. Since the trapezoidal profile is being calculated on fixed point digital hardware, the rising and falling edges are discretized to a staircase as shown

TABLE 4.7.1
DESCRIPTION OF THE MAIN STATE MACHINE

State	Description	Duration
Wait	Wait for valid data	Until a start flag is raised
Calc_RT	Convert the rise time to clock cycles to simplify calculations	Until the arithmetic operation is complete
Calc_TT	Convert the target time to clock cycles to simplify calculations	Until the arithmetic operation is complete
Calc_f_{max}	Calculate the maximum frequency of the velocity profile	Until the arithmetic operation is complete
Calc_Slope	Calculate Δt and Δf which make up the slope of the velocity profile	Until the arithmetic operation is complete
Rising	Increase velocity by Δf for each Δt	Until T_R is elapsed
Steady	Velocity is constant at f_{max}	From T_R to $T_P - 2T_R$
Falling	Decrease velocity by Δf for each Δt	From $T_P - 2T_R$ until T_P
Finish	Raise flag, set $P_{Desired}$, return to Wait state	One clock cycle

in Figure 4.7.1. The values of Δt and Δf, which correspond to the width and height of the staircase of the trapezoidal profile respectively, are simultaneously calculated during the state Calc_Slope. Since, The maximum frequency f_{max} will vary according to the magnitude of the target in steps, it is not feasible to use fixed values for Δt and Δf. To divide every f_{max} by the same fixed number of points Δt and calculate Δf accordingly is also not feasible because it is possible that the fixed point calculations of Δf will result in a zero value. The following algorithm was designed to generate suitable values for Δt and Δf without division and the corresponding state machine is presented in Figure 4.7.2. Let $\Delta f = f_{max}$ and $\Delta t = T_R$. For each following clock cycle the values of Δf and Δt are halved by a bit shift until Δf is between zero and 10. This method of repeated bit shifting will

guarantee that Δt and Δf are non-zero. Although this method does add calculation time before each velocity profile can be executed, the calculation time is minor considering the clock speed of today's FPGAs.

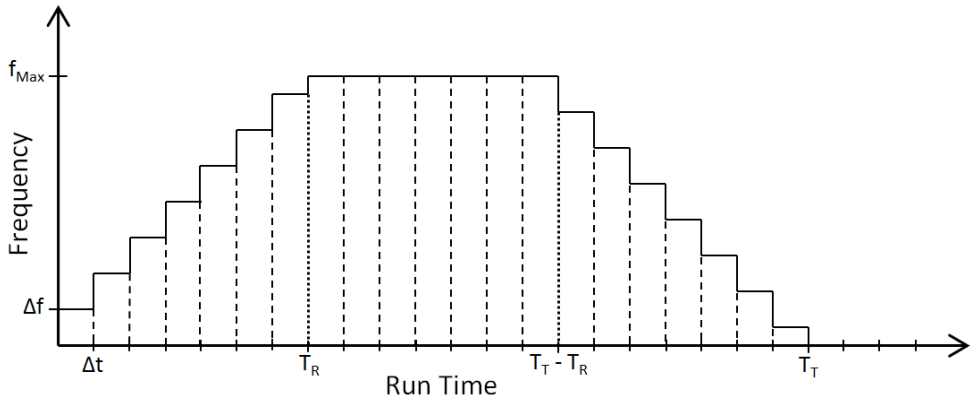

Figure 4.7.1. Discretized representation of the trapezoidal velocity profile.

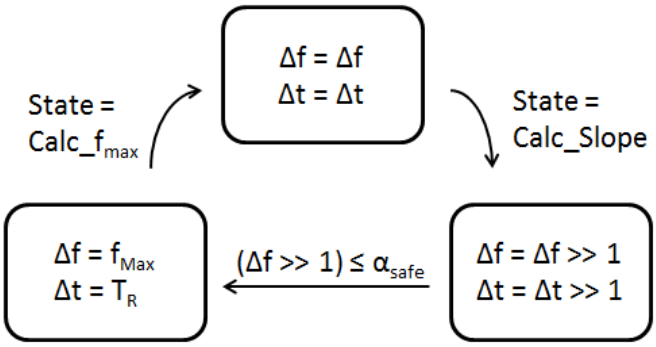

Figure 4.7.2. State machine for calculating Δf and Δt. The ">>" operator denotes a right bitwise shift

As with the previous design, the current frequency, $f_{Current}$, and desired position, $P_{Desired}$, are continuously calculated with specific equations dependent on the current state during the rising, steady and falling states. $f_{Current}$ is generated according to the velocity profile based upon $f_{max}, \Delta f$, and Δt using the following logic,

$$f_{Current} = \begin{cases} f_{Current} + \Delta f & t < T_R \\ fMax & T_R < t < T_T - T_R \\ f_{Current} - \Delta f & T_T - T_R < t < T_T \end{cases}, \quad (4.7.2)$$

where the given time constraints also correspond to the start and finish of rising, steady and falling states respectively. Using this method, the resulting velocity profile is generated using very little logic and only fixed point calculations. PDesired is calculated based upon the geometry of the velocity profile as follows in (4.7.3) for the Rising Steady and Falling states,

$$P_{Desired}(t) = \begin{cases} \dfrac{t^2 * f_{Max}}{2 * f_{Clock} * T_{Rise}}, & Rising \\ \dfrac{(t - T_{Rise}) * f_{Max}}{f_{Clock}} + \propto, & Steady \\ \dfrac{(T_{Target} - t)^2 * f_{Max}}{2 * f_{Clock} * T_{Rise}} + \beta, & Falling \end{cases}, \quad (4.7.3)$$

where t refers to the elapsed time in clock cycles since the start flag was raised. The varaibles α and β refer to the desired position after the previous state i.e. $\alpha = P_{Desired}(T_{Rise})$ and $\beta = P_{Desired}(T_{Target}-2\ T_{Rise})$. The units for T_{Rise} and T_{Target} are clock cycles, and the units for f_{Clock} and f_{Max} are steps per second.

Although absolute parallel computation is a major benefit of an FPGA based design, it comes with a tradeoff as demonstrated by the results of the previous design. There is a necessary tradeoff between computational speed and logic area. Addition and subtraction logic have a very small footprint, however multiplication and division hardware can consume a large amount of logic area. To conserve logic area, dividers were avoided where possible by using bit shift operations. For calculations where division is unavoidable, this system makes use of one shared arithmetic unit to perform all of the multiplication and division calculations necessary for each state.

The arithmetic unit consists of three multipliers and one divider which are configured in the fixed configuration shown in Figure 4.7.3. The general function of this arithmetic unit is

$$Result = \frac{A * B * C}{D * E}, \tag{4.7.4}$$

where A, B, C, D and E refer to hardware registers which are changed depending upon the required arithmetic operation of the current state. The calculations of equations (4.7.1) and (4.7.2) were derived so that they could be calculated using this single arithmetic unit by changing the input register values to the values in Table 4.7.2 depending upon state.

TABLE 4.7.2
ARITHMETIC UNIT INPUT REGISTER VALUES

State	A	B	C	D	E
Calc_f_{max}	P_{Target}	f_{clock}	1	1	T_{Target} -T_{Rise}
Rising	t	t	f_{Max}	f_{clock}	$2T_{Rise}$[α]
Steady	t - T_{Rise}	1	f_{Max}	f_{clock}	1
Falling	T_{Target} -t	T_{Target} -t	f_{Max}	f_{clock}	$2T_{Rise}$[α]

[α] The coefficient of 2 is accomplished through a left bitwise shift.

To convert the controller output frequency to the proper step command which should be received by the chopper drive, a pulse generator module is necessary. The pulse generator module is simply composed of a counter and a divider. The counter counts to a target value which indicates completion of a time period corresponding to $f_{current}$ calculated by the controller. After the counter reaches this value, a pulse is output on the step pin for the corresponding motor and the pin is raised high for 100 microseconds which is above the minimum logic high time for the chopper drives. The calculation of the target value in relation to $f_{Current}$ is performed as follows

$$PPS = \frac{f_{Current}}{f_{Clock}}, \tag{4.7.5}$$

where PPS refers to pulses per second. This operation requires an additional serial divider.

These modifications yielded significant reduction in hardware utilization per axis as demonstrated in Table 4.7.3 below. The logic hardware requirements of the motion core now less than half of the original design. In terms of ALMs, a single device could now control more than 20 motion core modules. Although the use of multipliers is still high, these can be implemented in ALMs once the DSP resources are depleted, or a serial multiplier could be used. The sacrifice for this decrease in hardware utilization is an increased computation time for the desired position calculations from 20 nanoseconds to 2 microseconds. The end effect is a reduction of the maximum controller sampling frequency from 50 MHz to 500 KHz which still exceeds the need for the current applications.

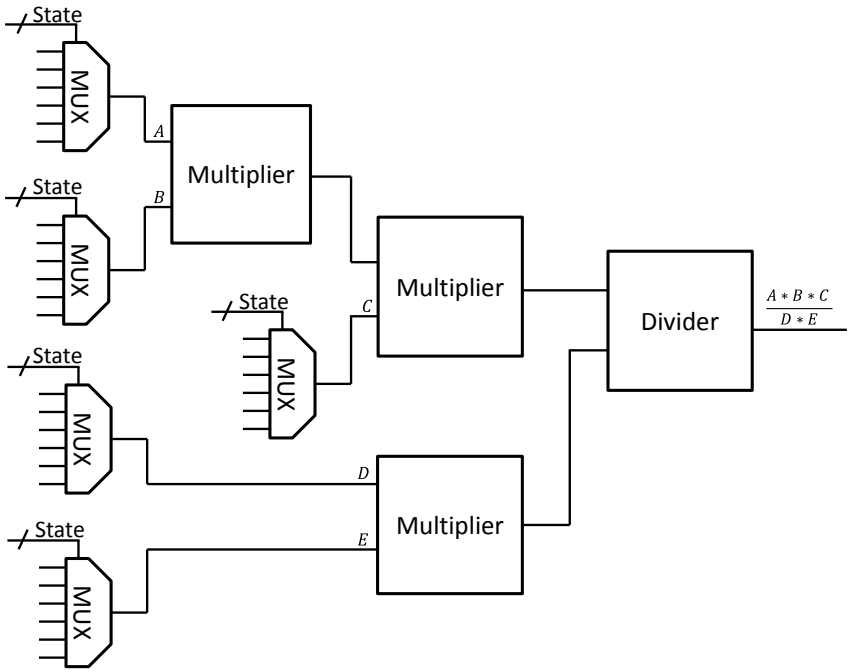

Figure 4.7.3. Arithmetic unit shared by all states. Values A, B, and C are switched depending on the state.

TABLE 4.73
HARDWARE UTILIZATION

Module	Combinational Functions	Dedicated Registers	DSP Elements
Motion Core	3522	1450	24
Serial Divider	339	328	0

Performance of the controller was validated through several experiments to measure tracking performance. The tracking performance was tested using a sigmoid trajectory of 16 rad. This same experiment was performed by previous works [67, 84, 85] to demonstrate tracking performance of stepper motor control algorithms. The reference trajectory and motor response are shown in Figure 4.7.4 and the tracking error is shown in Figure 4.7.5 below. Maximum and mean absolute tracking error were observed to be 0.0123 rad and 0.0023 rad respectively during the 2 second period with a motor precision of 0.00314 rad.

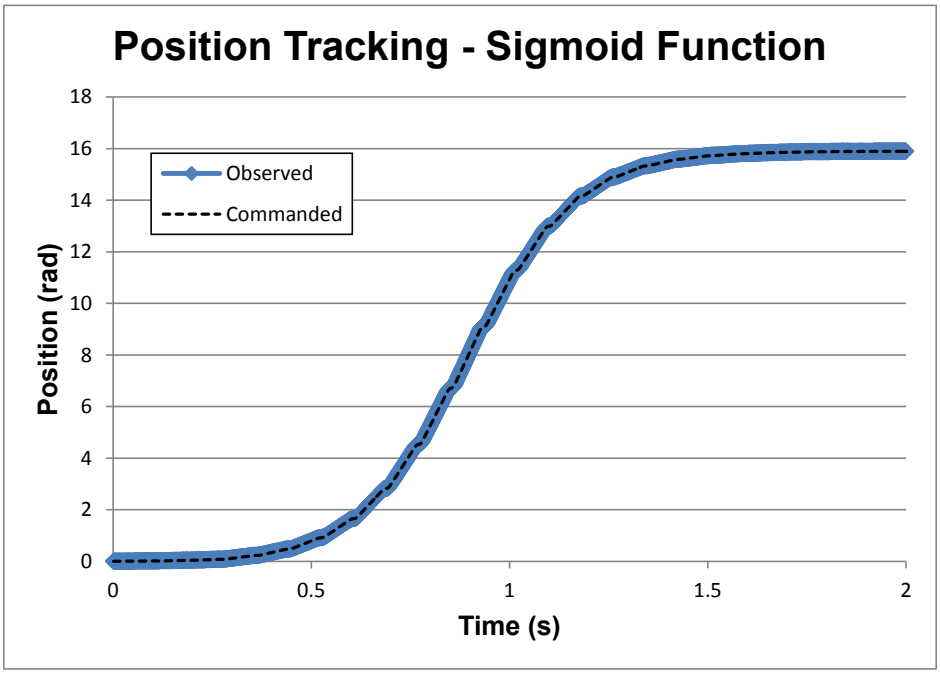

Figure 4.7.4. Commanded and observed position in radians during the tracking of the sigmoid function.

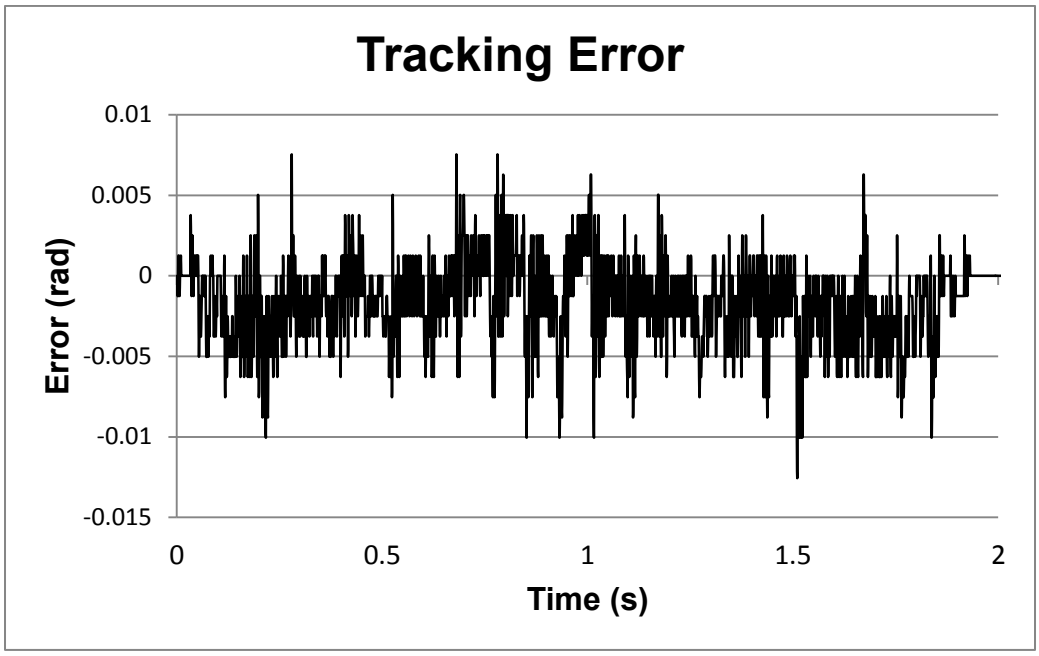

Figure 4.7.5. Tracking error during the tracking of the sigmoid function.

Tracking performance was also tested using a sinusoid with amplitude of 1 rad and increasing frequency over time. This signal, which is often referred to as a chirp signal, is used in many works to validate the motion bandwidth of the system. Tracking of the chirp signal, shown in Figure 4.7.6, was again excellent with average and maximum absolute error measured to be 0.0034 and 0.0339 rad respectively. The average absolute error is almost equal to the precision of the motor which is 0.00314 rad. Tracking error over time is plotted in Figure 4.7.7. Although the digitalized chirp signal showed a few areas of distortion, they were still tracked appropriately by the motor and controller which further emphasizes the performance of this controller.

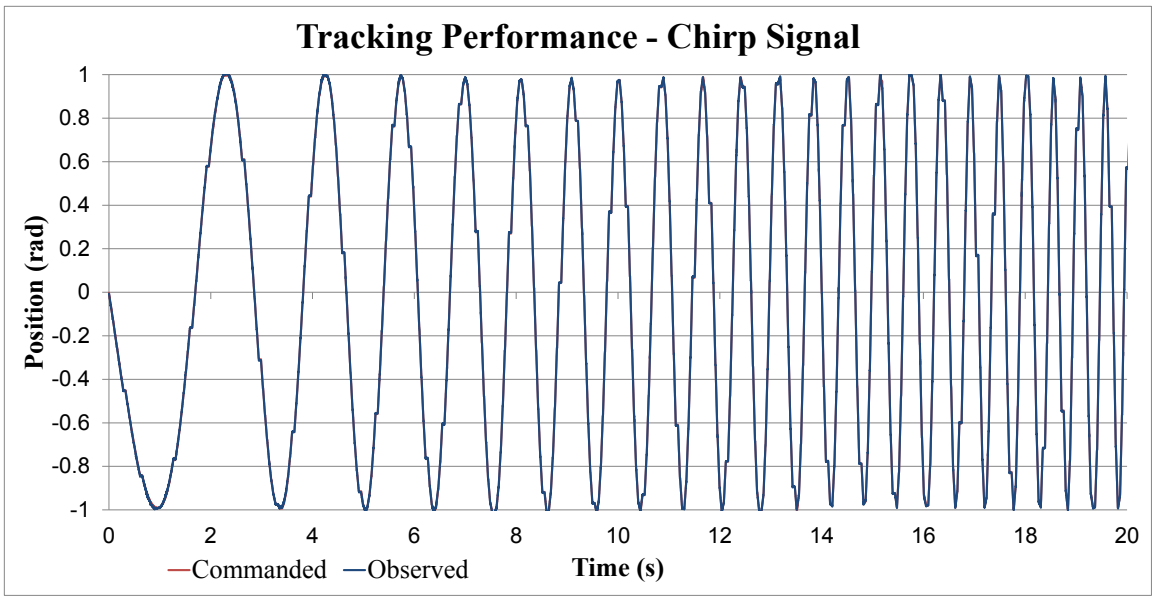

Figure 4.7.6. Tracking performance of a sinusoid with increasing frequency.

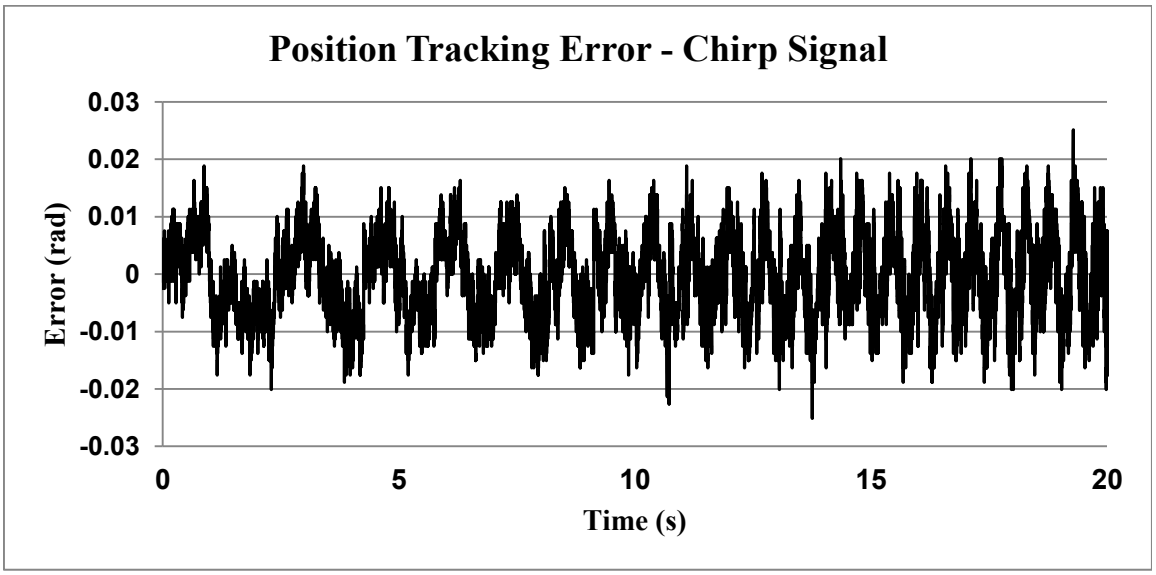

Figure 4.7.7. Tracking error during the tracking of the chirp signal.

5. Solid Media Flexible Transmission

5.1 Motivation and Benefit

MRI is an intrinsically three-dimensional modality which offers high contrast and spatial resolution and a plethora of soft tissue contrast mechanisms for assessment of anatomical morphology and function [18, 86]. These benefits, in addition to the fact that it does not require ionizing radiation, make it a desirable methodology for image guided interventions. However, the constraints of the magnetic resonance (MR) environment such as space, material, and signal noise present many challenges in the development of MRI guided interventions. The advent of such interventions first relies on the research, development, and exploration of compatible actuation technologies which must be able to provide safe and precise actuation within the confined space of the MRI machine at the presence of high magnetic fields and rapidly changing magnetic field gradients. Additionally, the operation of these devices should not interfere with the RF sensitive imaging process or affect image quality. The ASTM F2503–08 standard defines some standard terminology including the MR environment, which is described as the volume within the 0.50 mT line of the MRI machine and three categories of MR compatibility: MR Conditional, MR Unsafe, and MR Safe which refer to an item which poses risk of hazard in the MR environment under some conditions, any conditions, or no condition respectively.

Most common robotic and actuation mechanisms contain magnetically susceptible materials or electromagnetic components which are MR Unsafe. Therefore, MR Safe and MR Conditional power transmission methods have been used to transmit force from MR Unsafe drive components located outside of the MR environment to end effectors which

are MR Safe or MR Conditional. Power transmission systems used to date include pneumatics [32, 48], hydraulics [30, 87], and mechanical drive systems including but not limited to cables, belts, and driveshafts [16, 80, 88, 89]. MRI safe ultrasonic motors (USM), are also very popular as direct drive [38, 40] or used in combination with power transmission methods [16, 89]. Efforts to address EMI from USM include interleaving imaging and actuation [40], specialized in-room filtered drivers [41], and extensive shielding even with commercial USM, as example with Shinsei [90-96] and Squiggle or PiezoWalk [97, 98]. The reported success of each of these methods has varied between groups and relies not only on the actuation method itself, but the specific application and implementation.

Extensive literature reviews of MRI compatible actuation techniques and systems have been presented by Gassert et al. [28] and Tsekos et al. [18] and Section 3.1 and 3.2 of this work. Recent developments include devices for anatomy-specific interventions such as in the prostate [32, 53, 54], heart [49], and brain [10], as well as for general needle positioning [16, 33]. In the last five years, groups have reported significant improvements in image quality with less than 5% SNR reduction using pneumatic or hydraulic actuation [31, 32] or USM with filtered control signals [41, 99] in closed-bore MRI machines as compared to previous reports 30 to 60 percent [16, 52]. Submillimeter positioning accuracy [32, 49, 100] is also becoming standard. These innovations, along with the current commercialization of the NeuroArm (IMRIS Inc.) [10] have demonstrated that closed-bore MRI compatible interventions are now within the realm of possibility.

However, a critical barrier, therefore, in the development of MRI guided interventions is the development of "true" MRI compatible actuators [18]. Further research into specialized actuation methods is required to enable real-time image-guided interventions (IGI) within traditional and future closed-bore MRI scanners and to deliver the benefits of MRI guidance to more interventions. In this work we intend to explore a new method of MR safe force transmission which could provide fast and precise actuation without the use of any metallic or electrical components inside the MRI bore. Such technology would enable future robotic systems to perform real-time positioning of an end effector to organs or other areas of interest. This section presents the results of the preliminary investigation into the feasibility and performance of a new method of remote power transmission, herein referred to as Solid Media Flexible Transmission (SMFT).

Similar to pneumatic or hydraulic systems, SMFT decouples the end effector from the actuator by transferring force through semi-flexible tubes allowing power from MR unsafe actuators to be transferred into the MRI bore safely with minimal interference. In addition to these benefits, SMFT can provide fast and precise actuation and maintain stiffness or back drivability by control of the motors used for remote actuation. The media used to transfer force are many discrete, uncompressible objects therefore the system is not subject to laws of fluid dynamics which have been a reported challenge for MRI compatible applications [28, 101, 102]. Moreover, SMFT tubes can be routed freely without the requirement of a fixed mounting structure, redirection system, or tensioning devices such as those required by cable, belt, or driveshaft transmissions.

Of the several methods of MRI-compatible actuation discussed, each has its specific benefits and drawbacks. There are many factors to be considered in selecting

actuation hardware which are dependent on the application. However, three themes have presented themselves repeatedly in MRI-compatible research thus far: safety, image quality, and kinematic performance. It can be observed that no system published so far is perfect in regard to each of those themes, but instead they each have their strengths and weaknesses. In terms of MRI-compatibility, which refers to a relative assessment of a devices safety and preservation of image quality, pneumatic and hydraulic (fluidic) systems are the most compatible because they are decoupled from electromagnetism [102]. However, fluidic systems are dynamic non-linear systems by nature and have poor kinematic performance and controllability issues [28, 101, 102]. For this reason, the most favored method of MRI compatible actuation to date is piezoelectric or ultrasonic motors (USM) [18]. MRI safe USM offer superior kinematics and resolution, powerless braking and commercial availability (e.g. Nanomotion, PiezoWalk®, Shinsei, and Squiggle) [35, 37-40, 74, 90, 92, 93, 98, 103-107]. However, although these motors are labeled as MR safe by manufacturers, they are not intrinsically compatible, and are safest in remotely actuated applications since they require electric drive signals and wiring for operation. The use of such actuators as remote actuators has been performed by several groups [16, 89], but since noise must be filtered using the same methods as for electromagnetic actuators the only benefit they provide is that they do not contain magnetic materials at a significant cost sacrifice since the cost of USM and drivers is several times greater than an electromagnetic equivalent.

The proposed method of force transmission is designed to enable the use of traditional electromagnetic actuators, or any traditionally incompatible actuator, in the MR environment. It works by decoupling compatible end effectors from standard

actuation devices located outside of the MR environment. Overall the concept of is similar to traditional hydraulic or pneumatic systems in which a force applied to one end of a tube results in a force at the opposite end. However, the system is in fact fundamentally very different from hydraulic and pneumatic systems due to the fact that the actuation media are not fluidic and the actuation media are incompressible. The inherent results of these two distinct differences are that the proposed actuation system does not follow the laws of fluid dynamics nor does it have the same non-linear dynamics of the hydraulic and pneumatic systems. SMFT is a rigid but bendable power transmission system therefore the kinematic properties of the end effector are a direct result of the actuators themselves except for the effects of backlash and friction which are minimized throughout this work.

It is important to express that the proposed power transmission system is not a suitable replacement for pneumatic or hydraulic power transmissions systems in their traditional industrial applications which may require high speed rotation, or high force output respectively as their nature allows them to excel in these areas. In fact the proposed system may appear to be more "basic" than pneumatics or hydraulics. However, previous works, which make use of fluidic actuators, reported pressures as high as 5 bar for pneumatic systems [31, 32, 49] and 15 bar for hydraulic systems [31]. SMFT is not pressurized in the same manner. Although some undesired radial force is exerted by SMFT, force distribution is not homogeneous or omnidirectional throughout the transfer tube as the case with fluidic transfer therefore it will not leak at any arbitrary point if punctured. Furthermore, since the diameter of the motion elements is similar in size to that of the transfer tube, a "leak" is only likely if the tube is completely severed or

disconnected. It should be recognized that, although this novel method of force transmission could be useful in future applications which require EMI free force transmission, force transmission without the use of conductive or paramagnetic material, or low-force positioning which requires remote actuation without fluid dynamics, the current scope of the proposed system is strictly MRI compatible actuation, in which, SMFT will provide the following benefits:

- The kinematic characteristics of any actuator can be transferred through SMFT in an intrinsically compatible manner.
- Actuators are relocated outside of the already constrained operating area.
- SMFT is a bendable and can be adapted to the requirements of the workspace.
- SMFT is not susceptible to small leaks as fluidic systems are.
- SMFT does not make use of any paramagnetic or conductive materials beyond the remote actuation point.
- Signal propagation will not occur through SMFT transmission lines.
- SMFT motion elements are non-compressible and rigid.
- SMFT is only “pressurized” when in motion.
- When paired with stepper motors, SMFT can provide sufficiently fast actuation without the need for brakes.

5.2 Motion Elements

The design of SMFT is basic in principle; many discrete, solid, low-friction components are used as the medium to transfer force inside of a tube. The tube itself acts as a semi-flexible guide to transmit the force from the actuator to the end effector. However, the interaction between the tube and the solid media, which will be referred to as the "motion elements", are subject to dynamics, most notably friction, which could reduce efficiency or lead to a complete loss of force before the end effector depending on the configuration of the motion elements. The selection of low friction components is crucial to enable efficient motion transfer and so are the dimensions and resulting clearances between components. Sufficient clearance is requirement for motion within the tube, but excessive clearance will be prohibitive of motion transfer as discussed below.

Figure 5.2.1 demonstrates four configurations which were compared during the preliminary design of SMFT. In all cases, the solid media being used are non-paramagnetic ball bearings. Ball bearings were chosen because their round shape makes it so that their orientation inside the transfer tube is not important. In the case of orientations c and d, hollow cylindrical bushings were added. The shape of these items will enable them to maintain their orientation within the transfer tube.

The first configuration (Figure 5.2.1a) uses ball bearings which have a diameter much smaller than the transfer tube. The goal of this configuration is to produce an almost fluid like media which will conform to the shape of the tube. However, by using small solid media rather than a fluid, the media is still non-compressible and rigid. The

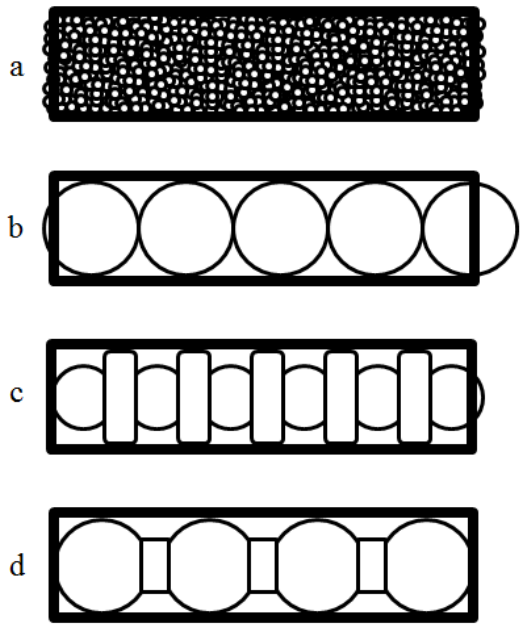

Figure 5.2.1: Solid media configurations: a) many small ball bearings b) bearings and tubes equal in diameter c) hollow cylindrical bushings with smaller ball bearings d) ball bearings with smaller bushings for alignment.

second configuration (Figure 5.2.1b) is the opposite approach of the first configuration because ball bearings are chosen with a diameter just slightly less than the diameter of the transfer tube. This configuration allows for motion only in the desired direction of actuation because the vertical position of the ball bearings is maintained by the tube. The third configuration (Figure 5.2.1c) consists of using short hollow cylindrical bushings which are linked together with ball bearings. The cylindrical bushings are chosen with diameter slightly less than the tube to maintain orientation within the transfer tube and maintain force direction. The ball bearings, which are smaller than the bushings and lock into the inner bore of the bushing, allow the cylinders to pivot and maintain alignment during tube bending. The fourth configuration (Figure 5.2.1d) is dimensionally opposite of the third. Ball bearings are chosen with diameter just less than that of the transfer tube. Bushings are chosen to be smaller than the bearings so that they can guide the ball

bearings without interfering during bending. Tubes of each of the four configurations were constructed with lengths of 1 m, however only configuration (d) successfully transmitted motion at the distal end of the tube. The following analysis was performed on this configuration to explain the results as well to gain insight toward the optimization of force transfer using this configuration.

In a first approximation, shown in Figure 5.2.1a, the dynamics of SMFT can be appreciated considering the ideal case in Figure 1a which shows a straight tube filled with *n* motion elements, which in this case are spherical ball bearings, with a diameter smaller than the internal diameter (ID) of the tube. In the frictionless condition, an actuation force (F_A) applied along the center of the spheres in the axial direction of the tube would be transmitted via motion of the bearings to the end effector delivering an output force (F_{SMFT}). In the actual case, friction exists at several places in the system including: the point of interaction between the bearings and the tube wall, the actuator and the first bearing, the interaction between bearings, and the last bearing and the end effector. At these friction points there could exist many types of friction depending on the state and type of motion, but in this case we make the worst case assumption that the bearing is not rolling and only consider dry friction. Since we are concerned with force transfer in the axial direction, we must consider the friction at each bearing and wall interaction. This can be estimated as the product of the friction coefficient and the normal force at the point of interaction. The output force F_{SMFT} would then be expressed as

$$F_{SMFT} = F_A - \sum_{i=1}^{n} F_{Fi} = F_A - \mu \sum_{i=1}^{n} mg, \qquad (5.2.1)$$

where n is the number of motion elements, μ is the coefficient of friction, F_{Fi} is the normal force between the i^{th} motion element and the tube, m is the mass of the element,

and g is gravity which in Figure 5.2.2 is assumed to be normal to the tube. To estimate the total friction force for a tube of 1 m in length, consider that each motion element is a 6.35mm plastic bearing with approximate mass of 200 mg. The coefficient of friction for low friction plastics falls between 0.1 and 0.5. Therefore the total friction force will be less than 0.5 kgf by the above estimation. However preliminary experiments demonstrate that with approximately 25 kgf applied by the actuator there is no force output at the end effector, thus all force is dissipated through friction before reaching the end effector.

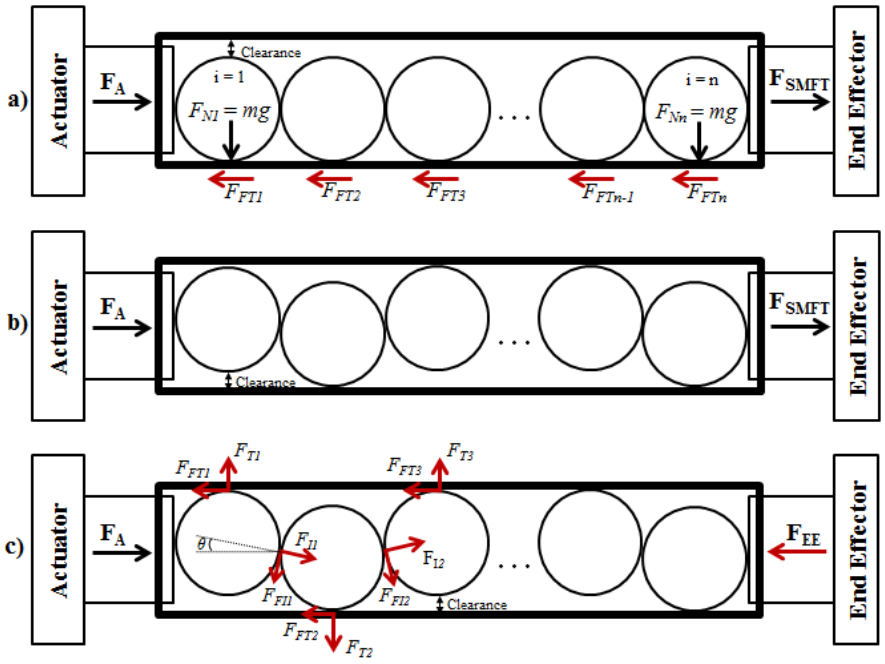

Figure 5.2.2. a) Ideal case friction is proportional only to the weight of the motion elements. b) Misalignment and due to clearance between the bearings and the tube. c) Interaction forces in equilibrium (zero output).

The difference between the approximation of Figure 5.2.2a and the experimental case is the orientation of the bearings at the time of actuation. As a result of the free space provided by clearance between the tube and motion elements, force applied by the actuator changes the alignment of the motion elements to a zigzag pattern as shown in Figure 5.2.2b. If friction is low between the walls and the motion elements, the bearings

should still slide toward the end effector. Therefore we can conclude that the friction is in fact very high. To analyze the source of friction, consider the equilibrium force diagram of Figure 5.2.2c. Each bearing *i* has an interaction force with the tube wall (F_{Ti}) and an interaction force between each proceeding bearing (F_{Ii}). The associated friction forces for these interactions are F_{FTi} and F_{FIi} respectively. The force diagram illustrates that the normal forces F_{FTi} are no longer only a product of mass and gravity (at arbitrary direction not shown in the figure), but they also contain components of the interaction forces between the motion elements. Therefore the axial force applied by the actuator (F_A) is contributing to friction force at each element and it is effectively being dissipated along the wall of the tube. This force dissipation is a proportional to the angle θ which is a result of the tube to motion element clearance. Although the coefficient of friction between materials is low, the actuation force is relatively high therefore large frictional forces exist even for relatively small values of θ. In light of this analysis, it is realized that the size, shape, and configuration of the motion elements are critical to the efficiency of power transmission and it is hypothesized that SMFT is still feasible with an optimization of the motion elements.

In response to the above preliminary studies, we selected an alternating pattern of spherical bearings and cylindrical bushings which have an outer diameter (OD) less than that of the spherical bearings. The hollow ID of the cylindrical bushings provides for a ball and cup interaction with the spherical bearings. A simplified force diagram is used to demonstrate the effectiveness of this configuration (Figure 5.2.3b) as compared to the previous one (Figure 5.2.3a). The spherical bearings effectively act as pivot points to enable bending of the tubes (Figure 5.2.4c), which is necessary for flexible routing and

the cylindrical bushings act as spacers, which by increasing the distance between spherical bearings, effectively reduces the angle of misalignment. With the addition of the cylindrical bushings, the zigzag pattern and diversion of force from the axial direction should be reduced proportional to the length of the bushings.

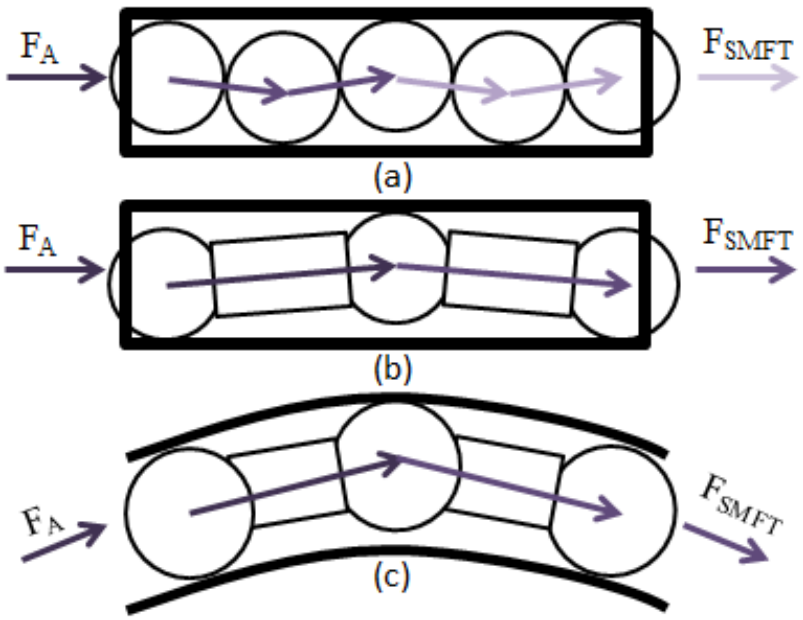

Figure 5.2.3. Simplified force diagrams. a) Misalignment of motion elements. b) Alternating pattern reduces aligns reaction. c) Pivoting along spherical bearings enables flexible routing.

5.3 Prototype Specifications

The actuator chosen for this experiment was a NEMA 24 stepper motor model 24Y508 (Anaheim Automation, USA). The motor was driven by a G213V Digital Step Drive (Geckodrive USA) with fixed 10x microstepping. Operating voltage and current were 40 VDC and 7 A respectively. A custom actuation block was used to interface the motor to the SMFT via dual rack and pinion with two opposing racks and one gear. The current implementation of SMFT is a push only method, so two lines are required per end

effector. However, opposing motion of the racks requires only one gear and motor per DoF as shown in Figure 5.3.1. The output force of this actuator block was measured to be approximately 23 kgf.

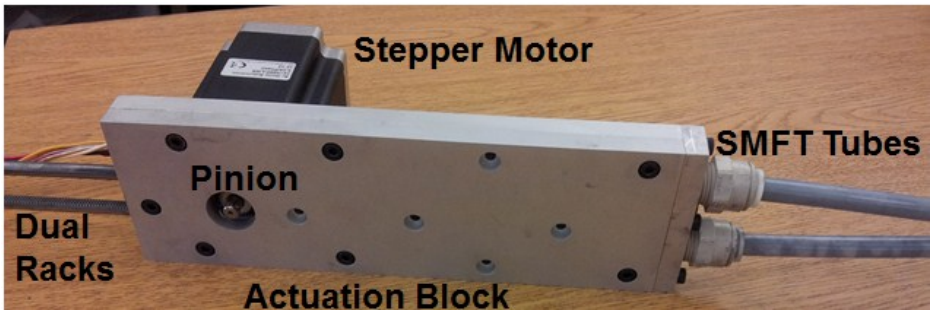

Figure 5.3.1. Actuation block which interfaces a stepper motor to the SMFT tubes using dual rack and pinion.

The end effector (Figure 5.3.2) is a single degree-of-freedom positioning stage constructed of the low friction plastic Delrin. The positioning stage consists of a ball bearing slide which is actuated directly by force applied by the SMFT. The motion elements are guided through the supply and return channels which are indicated by the arrows in Figure 5.3.2. The direction of motion indicated by the arrows corresponds to the direction of motion element travel in the forward direction. When the motor is reversed, opposing motion causes the media travel in the opposite direction pushing the stage in the reverse direction. A US digital 500 CPI optical encoder with copper wiring was used to measure the position of the ball bearing slide for these benchtop studies for its accuracy. However, an in house made MR safe 100 CPI fiber optic encoder was developed for use in the MR environment.

The SMFT tubes and motion elements were constructed from off the shelf hardware including nylon tubing, Delrin precision ball bearings, and nylon cylindrical bushings. These available components provide for approximately 0.7 mm tube to bearing

clearance, and the nominal diameters and coefficients are listed in Table 5.3.1.

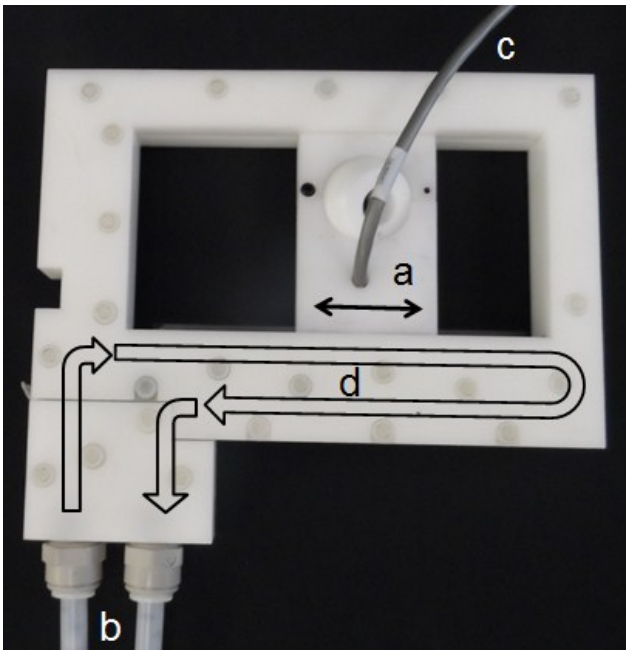

Figure 5.3.2. Single degree-of-freedom end effector composed of a) ball bearing slide positioning stage b) SMFT tubes c) encoder and cable d) supply and return channels for motion elements.

TABLE 5.3.1
COMPONENT NOMINAL VALUES

Component	***Material***	***Inner Diameter***	***Outer Diameter***
Tube	Nylon	7 mm	9.5 mm
Bearing	Delrin	---	6.35 mm
Bushing	Nylon	4 mm	6 mm

For comparison, two lengths of bushings (Figure 5.3.3), 3 mm and 20 mm, were used in the following force transmission efficiency test. Preliminary experiments revealed losses through flexing in the radial direction of the hoses. This was overcome by the use of a thicker rubber hose to surround the flexible nylon hoses. Two nylon hoses were run through a single rubber hose as shown in Figure 5.3.4. The additional weight of the rubber

hose also provided for easier routing and ensured that the hoses maintain position once routed without sacrificing flexibility.

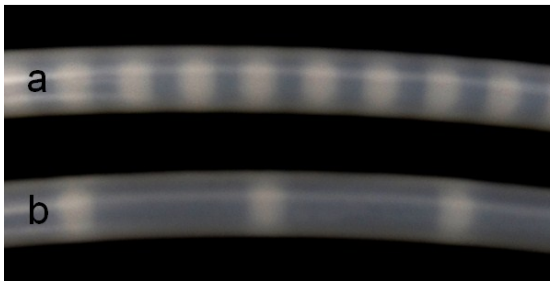

Figure 5.3.3. Two configurations of SMFT with a) 3 mm and b) 20 mm length cylindrical bushings.

Figure 5.3.4. Rubber hose was held around each pair of tubes.

5.4 Validation and Results

Force output results for seven combinations of bushing, transmission length, and curvature (a bend in the routing of the tube) are presented in Table 5.4.1. Overall transmission efficiency was greater than 56.6% for all tests demonstrating that SMFT is indeed feasible with the configuration of alternating spherical bearings and cylindrical bushings. The use of 20 mm bushings compared to 3 mm bushings gave significant improvements around 32% supporting the hypothesis that force transfer in improved by increasing the distance between the spherical bearings.

Two different tests were performed to estimate the backlash in the system. The first method entailed commanding the open-loop motion of the 1 DoF stage in a sequence of forward and backward motions of the same commanded distance. Two steps were performed in the same direction, followed by two steps in the opposite direction. This sequence was repeated five times each and the resulting motion was recorded for comparison. Comparing position data from back to back motion of the same direction to that of a changed direction it was determined that the observed backlash from motion is approximately 2.1mm for 1 m SMFT. The second method of backlash measurement was simply to record encoder data as the stage was to exert as much force as possible by hand in each direction and to measure the absolute distance traveled. The results of this measurement were approximate 5.1 mm for 1 m SMFT and 7.2 mm for 3 m SMFT.

TABLE 5.4.1
FORCE OUTPUT RESULTS

Test Condition	***Output Force (kgf)***
3 Millimeter Bushings – Straight Transmission	
1 meter	7
3 meter	4.32
20 Millimeter Bushings – Straight Transmission	
1 meter	10.5
3 meter	6.4
4 meter	4.8
20 Millimeter Bushings – 4 Meter Curved Transmission	
90˚ Bend[a]	3.9
Coiled[b]	1.2

a. Hose had a loose 90 degree bend of radius around 0.5 meters
b. Hose was tightly coiled with radius of 25 cm

To test the open-loop position accuracies a dataset of 24 points and directions were selected at random. Commanded motions from the random dataset, which included 13 direction changes, ranged from approximately 2 mm to 48 mm with an approximate average of 23 mm and each point should be reached in 1 second. These 24 relative

position commands were executed for 1 m, 3 m, and 4 m SMFT for comparison. Position was measured using a linear optical encoder (US Digital EM1, 500 CPI) and error was calculated as the absolute error between the target point and actual point after 1 second. For each test iteration, position is measured relative to the starting position of the end effector so error is not cumulative throughout the test. The range and mean absolute error for open-loop positioning are presented in Table 5.4.2 below.

TABLE 5.4.2
OPEN-LOOP POSITION RESULTS

SMFT Tube Length	***Min Error (mm)***	***Max Error (mm)***	***Mean Error (mm)***	***Mean Error (%)***
1 meter	1.6	13.7	7	29.8
3 meter	2.7	23.3	10.9	57.5

PID position control was implemented using encoder position data to provide precise positioning. Positioning accuracy was tested using a 24 point dataset. Each of the 24 points has random relative position and direction. The positioning stage was commanded to be at the desired position after 1 second. The observed range and mean absolute error after 1 second are given in Table 5.4.3 below.

TABLE 5.4.3
TIMED CLOSED-LOOP POSITION RESULTS

SMFT Tube Length	***Min Error (mm)***	***Max Error (mm)***	***Mean Error (mm)***	***Mean Error (%)***
1 meter	0.2	5.4	2.0	7.5
3 meter	0.1	5	1.9	10.5

The errors reported above represent the error after exactly 1 second travel time. The absolute steady-state error is equal to the precision of the encoder itself which in this experiment was 0.0127 mm. The settling time was calculated as the elapsed time after the 1 second commanded time for the positioning stage to remain be within ±0.5 mm of the target position. Setting time data is presented in Table 5.4.4 below.

TABLE 5.4.4
SETTLING TIME DURING CLOSED-LOOP POSITIONING

SMFT Tube Length	*Min Settling Time (s)*	*Max Settling Time (s)*	*Mean Settling Time (s)*
1 meter	0	1.3	0.4
3 meter	0	2.5	0.5

The step response was measured for 4 trials by stepping the actuator forward and backward as shown in Figure 5.4.1. The significance of changing directions is to include any negative effects of backlash in these test results. Mean rise-time was measured to be 187 ms. These results demonstrate the potential speed of SMFT as compared to pneumatics and hydraulics which can have much high reported rise times [31].

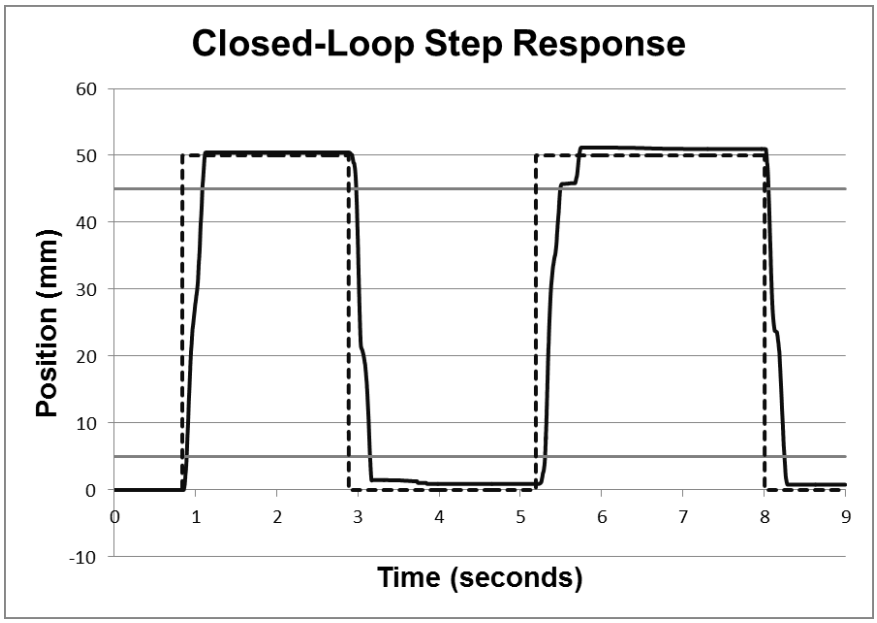

Figure 5.4.1. Closed-loop step response for 50 mm step. Dotted line is commanded position, solid line is actual position. Light grey lines indicate 10% and 90% of commanded position.

6. Generic Surgical Tool Positioning Robot

6.1 Motivation and Benefit

The motivation for developing MRI IGI capable robots has been outlined previously. Of the robots reviewed by this work, more than half of them were designed to

perform a specific intervention. However, in general the tasks performed by these robots was the same: to deliver a needle or surgical tool to a precise point in space with the correct angle of insertion. To explore and demonstrate the full potential of SMFT, a general purpose positioning robot has been developed to perform the task of tool or needle placement. The developed robot is a basic positioning system to meet the needs of a variety of interventions which require accurate or real-time positioning. This compact and lightweight design is free of the large or heavy actuators found on previous MRI compatible robots due to the remote actuation enabled by SMFT. Enabled by the technologies described in previous sections, this general purpose robot should meet several requirements of MRI guided interventions including: Compact design to occupy minimal space within the MRI machine, flexible routing of actuation tubes (enabled by SMFT), fast and precise positioning (enabled by SMFT and Stepper Motor Controller).

6.2 Configuration

The robot kinematic structure is four DoF capable of controlling rotation and translation of a surgical tool in the XY plane. The proposed configuration creates a very low profile design and more importantly allows the rotational orientation motion to be achieved created using only linear actuation by the use of passive spherical joints. Figure 6.2.1 shows a CAD prototype of the preliminary design of the robot which consists of two Cartesian stages which position a tool holder. The tool holder is held by two spherical joints to enable rotation. Opposing motion of the Cartesian stages will generate a rotation of the surgical tool around the axis of motion. The spherical joints are replaceable to allow the use of tools from diameter 5 mm to 30 mm without replacing other parts.

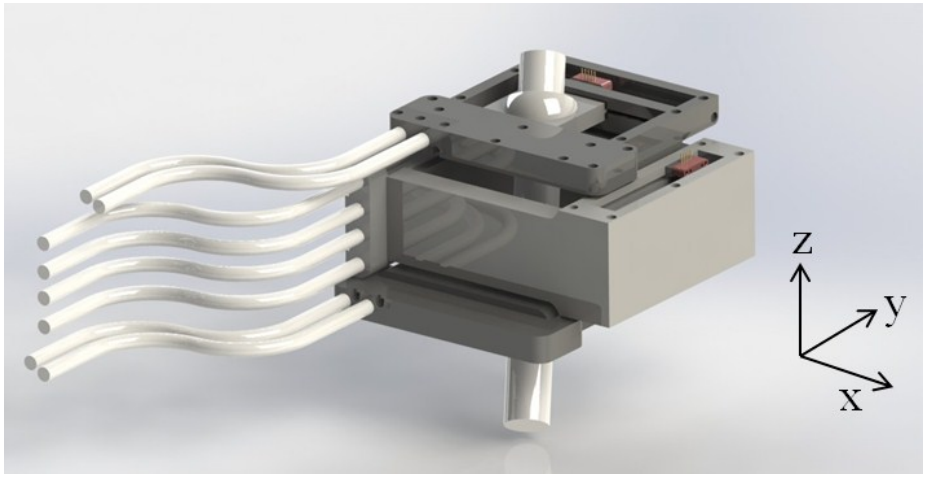

Figure 6.2.1. CAD drawing of preliminary design.

The Cartesian stages are composed from ball bearing slides which are integrated directly with the SMFT so that no motion conversion mechanism is required. Although the configuration of motion elements within the SMFT tubes consists of spherical ball bearings and cylindrical bushings, only ball bearings are used within the robot. Tight bends are made within the motion element tracks which will not allow for bushings to pass into the robot. The bends could be eliminated if the motion elements were to pass straight through, but it was desired to have all hoses enter and exit from one side of the robot. Figure 6.2.2 shows the implementation of the ball bearing slides and motion element tracks inside of the robot.

The four DoF robot consists of two Cartesian stages which are created from three main components: an upper slide, a lower slide, and a centerpiece (Figure 6.2.3). The upper and lower slides enable motion in the X direction and are held together by the centerpiece. Another ball bearing slide is located at the interface between each slide with the centerpiece to enable the motion in the Y direction. Since SMFT is push only, two lines were used for each X slide, one to push the stage forwards and one to push the stage

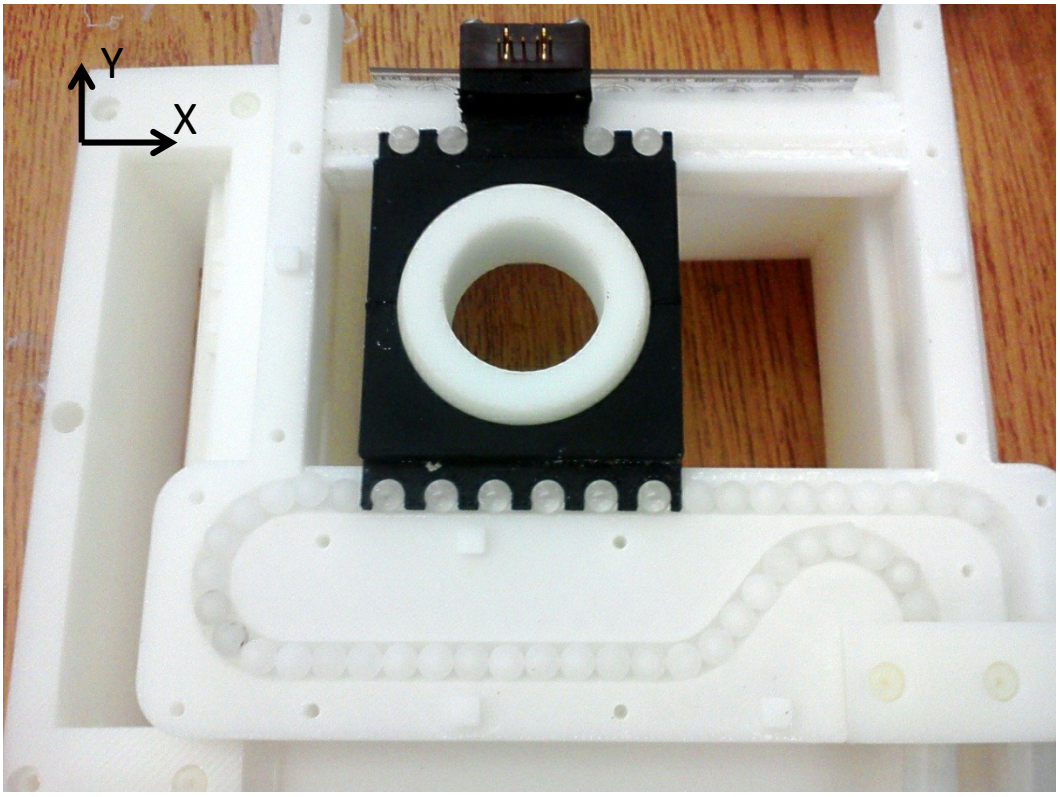

Figure 6.2.2. Preliminary prototype with top plate removed showing that XY Stages are constructed using ball bearing slides integrated directly with SMFT. Motion element tracks allow tubes to enter and exit from one side.

backwards. Four lines are used for the Y directions to increase the force and maintain alignment. This measure was taken because the entire weight of the X platform rests on the Y slide. All motion occurs relative to the centerpiece so mounting holes have been placed in the center piece so that it may be mounted to any structure for a specific operation. Linear encoders (US Digital) are used on the insides of each ball bearing slide to track position. MRI compatible fiber optic encoders are currently under development by the group to take the place of the currently installed US Digital encoders.

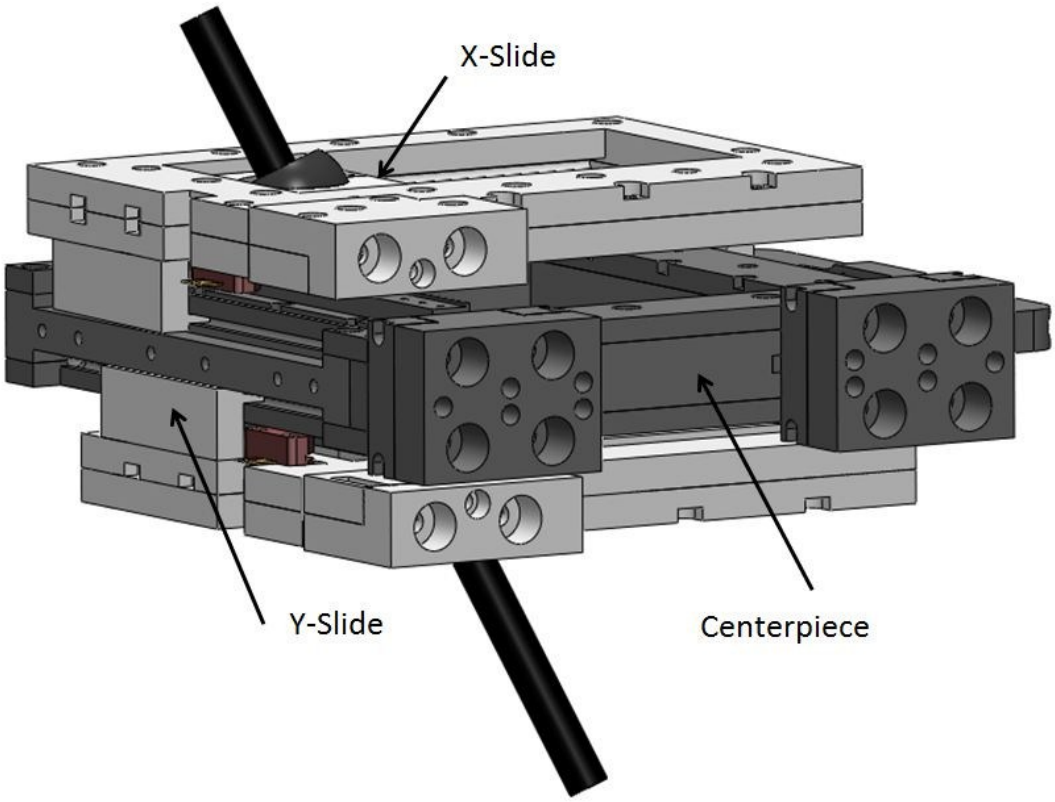

Figure 6.2.3. CAD drawing of preliminary design showing the two X-slide platforms (light grey), the centerpiece (dark grey), digital encoders (brown), and tool holder (black).

6.3 Inverse Kinematics

The kinematics of this robot are straightforward by design. By utilizing two Cartesian stages, which have a fixed distance between them, the position X_{Tool}, position Y_{Tool}, polar angle θ_{Tool} and azimuth angle φ_{Tool} of a tool can be controlled using the positions X_1, Y_1, X_2, and Y_2 of the two Cartesian stages. The definition of these coordinates with respect to the robot is shown in Figure 6.3.1. The relationship between the position of the surgical tool in relationship to the position of the two Cartesian stages is given by the following inverse kinematics.

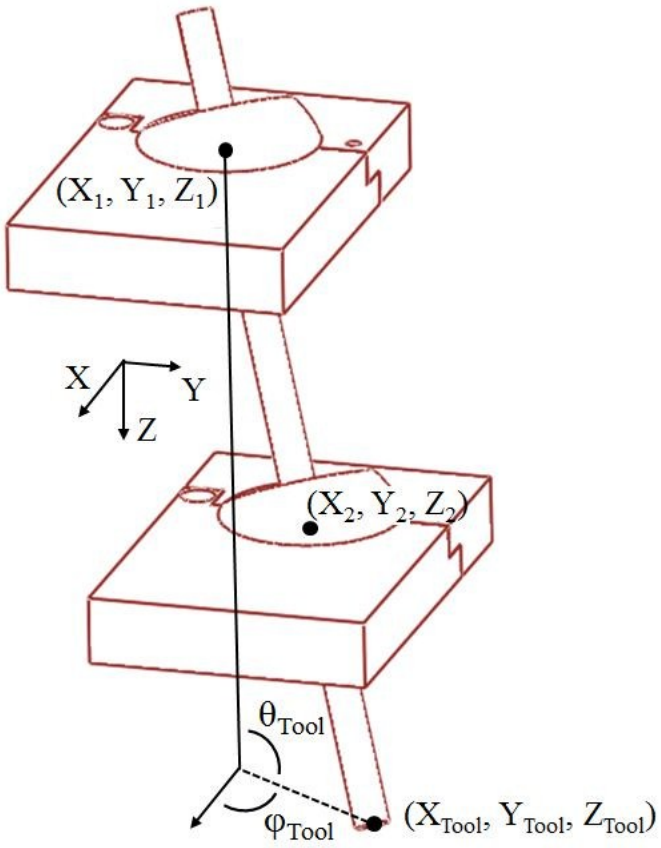

Figure 6.3.1. Definitions of coordinates and coordinate frame.

First the alignment of the tool to θ_{Tool} and φ_{Tool} is achieved based upon the relationship of the lower stage to the upper stage. The standard transformation between Cartesian and Spherical coordinates is written to relate the lower stage to the tool angles as follows,

$$X_{12} = r\sin(\theta_{Tool})\cos(\varphi_{Tool}), \tag{4.5.3.1}$$

$$Y_{12} = r\sin(\theta_{Tool})\cos(\theta_{Tool}), \tag{4.5.3.2}$$

$$and\ Z_{12} = r\cos(\theta_{Tool}). \tag{4.5.3.3}$$

Since the vertical distance between the two stages, Z_{12}, is fixed and known, r can be found using (4.5.3.3) as follows,

$$r = \frac{Z_{12}}{\cos\theta_{Tool}}. \quad (4.5.3.4)$$

These equations maintain the proper alignment between the two stages. To position the tool to the appropriate positions X_{Tool} and Y_{Tool}, the top stage is positioned using the following relationships,

$$X_1 = X_{Tool} - X_{12} \text{ and} \quad (4.5.3.5)$$

$$Y_1 = Y_{Tool} - Y_{12}. \quad (4.5.3.6)$$

The above equations fully define the relationships between the upper stage, lower stage, and position of the tool holder, but more information is required to perform a tool or needle insertion. Under MRI guidance, tracking markers can be used for registration of the robot in relation to the target point and tissue boundaries. Assume that the robot holds a sheath to guide a needle to a target beneath the skin of a patient. The coordinates (X_1, Y_1, Z_1) represent the centerpoint of the upper Cartesian stage, (X_2, Y_2, and Z_2) represent the centerpoint of the lower Cartesian stage, (X_{Tool}, Y_{Tool}, Z_{Tool}) represent the top of the sheath, (X_{Tissue}, Y_{Tissue}, Z_{Tissue}) represent the desired skin entry point, and (X_{Target}, Y_{Target}, Z_{Target}) represent the desired target point for the needle. The previously derived inverse kinematic relationships can be used to reach the target after solving for the appropriate tool angles.

The tool angles ($\theta_{Tool}, \varphi_{Tool}$) are determined by the relationship between the skin entry point and the target point. Again using spherical coordinate transformations the following relationships are determined using the Cartesian locations of the tissue and target,

$$r = \sqrt{\left(X_{Target} - X_{Tissue}\right)^2 + \left(Y_{Target} - Y_{Tissue}\right)^2 + \left(Z_{Target} - Z_{Tissue}\right)^2}, \quad (4.5.3.5)$$

$$\theta_{Tool} = \cos^{-1}\left(Z_{Target} - Z_{Tissue}\right), \quad (4.5.3.6)$$

$$and\ \varphi_{Tool} = \cos^{-1}\left(\frac{X_{Target} - X_{Tissue}}{r\sin(\theta_{Tool})}\right). \quad (4.5.3.7)$$

Now that the tool angles are established, the desired global positions of the upper and lower stage are given by,

$$X_1 = \frac{Z_{Target} - Z_1}{\cos(\theta_{Tool})}\sin(\theta_{Tool})\cos(\varphi_{Tool}), \quad (4.5.3.8)$$

$$Y_1 = \frac{Z_{Target} - Z_1}{\cos(\theta_{Tool})}\sin(\theta_{Tool})\cos(\theta_{Tool}), \quad (4.5.3.9)$$

$$X_2 = \frac{Z_{Target} - Z_2}{\cos(\theta_{Tool})}\sin(\theta_{Tool})\cos(\varphi_{Tool}), \quad (4.5.3.10)$$

$$and\ Y_2 = \frac{Z_{Target} - Z_2}{\cos(\theta_{Tool})}\sin(\theta_{Tool})\cos(\theta_{Tool}), \quad (4.5.3.11)$$

based upon the relationships derived in (4.5.3.1-4.5.3.4).

6.4 Design for Manufacture

The preliminary prototype components were designed using a Stratasys Prodigy Plus 3-D Printer. This 3-D printer constructs models using fused deposition modeling which deposits plastic material layer by layer via an extrusion head. Support material is deposited between the plastic support base and the bottom of the part as a foundation. As the part is built up, the support material is used to fill any holes in the current layer to keep a level foundation for the next layer. After the part is finished the support material is etched away in a chemical bath to remove support material. Any holes or cut features are removed during the etching process and only the desired solid features remain. Using this method of fabrication, all of the features of the part are created from liquefied raw material, therefore to optimize cost and build time during the design process, the volume

of the part should be minimized. Support material is used more sparsely than model material, so the model volume of parts designed for manufacture by 3-D printer was minimized to be as small as possible to maintain structural integrity. An example of a 3-D printed part is showin Figure 6.4.1. It can be seen from the figure that complex parts are well modeled with the 3-D printer, however the closeup in the figure demonstrates the rough surface texture which appears in the motion element tracks.

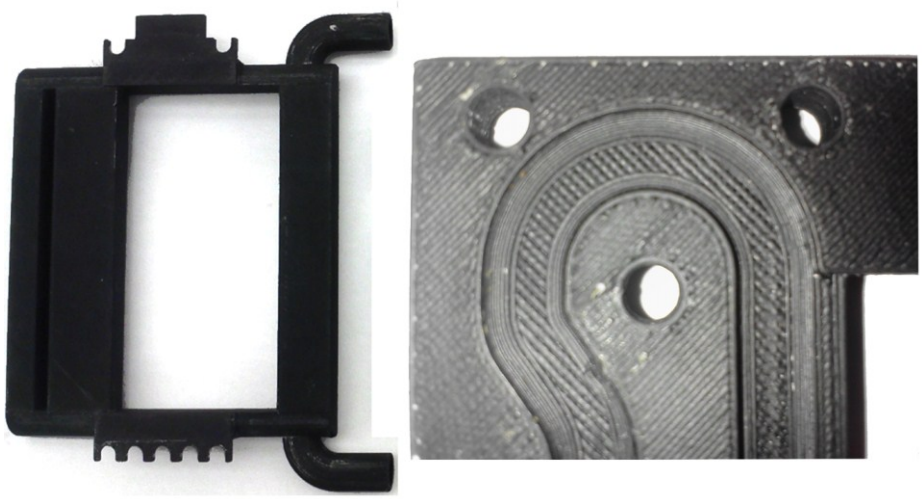

Figure 6.4.1. 3-D printed part and close-up to show surface texture.

Although the 3-D printer is an invaluable tool for rapid prototyping, it is has shown some limitations in this design including build material, surface finishes, and flexural strength. The acrylonitrile butadiene styrene (ABS) plastic prototypes produced for preliminary mock-up and experiments did not exhibit the flexural strength or low-friction properties required for a final prototype. To create a suitable final prototype, computer numeric control (CNC) milling was utilized. CNC machining, in contrary to 3-D printing, is a material removal process rather than a material additive process. Therefore, cost and machining time are determined primarily by how much material is removed from the work piece rather than the volume of the part. For this reason, the parts

for the final prototype required redesign since they were originally designed to use as minimal material as possible. A comparison between the actuation block designed for 3-D printing compared to designed for CNC is shown below. To save production costs and increase strength, the final robot prototype parts were all redesigned with as few cut features as possible to maintain functionality. However, An additional limitation was encountered switching from 3-D printing to CNC which is the inability for the CNC to create occluded features. For instance, because the 3-D printer adds material rather than drilling it, it is capable of generating complex paths or holes, such as the curved tubes in Figure 6.4.1. Since the CNC uses a milling bit to remove material, the machining face of the material requires two axes to be accessible to produce a feature and holes can only be drilled in a straight line. This means that parts with the described complex features must be produced in several pieces by the CNC process. This greatly adds to the complexity and number of parts in the design of the robot. Figure 6.4.2 and 6.4.3 below show two parts which were used for the same purpose. The first part was designed for the 3-D printer and was designed as one piece with minimal material used. The second part was designed in several pieces for the CNC process with minimal material removed and required three separate pieces.

To select the appropriate build material for the CNC machined prototype, eleven plastics were compared over five criteria. The five characteristics used in selecting a plastic included coefficient of friction, flexural modulus of elasticity, impact strength, tensile strength, and dielectric strength with significance in that order. The coefficient of friction should be extremely low to allow smooth and effortless motion between the parts and the SMFT motion elements which will provide the actuation force to the robot.

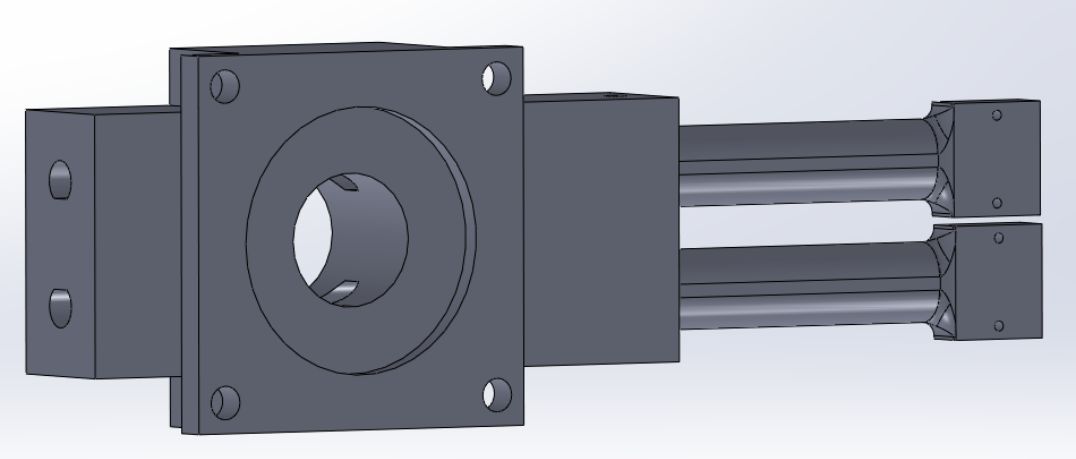

Figure 6.4.2. Actuation block designed for 3-D printing.

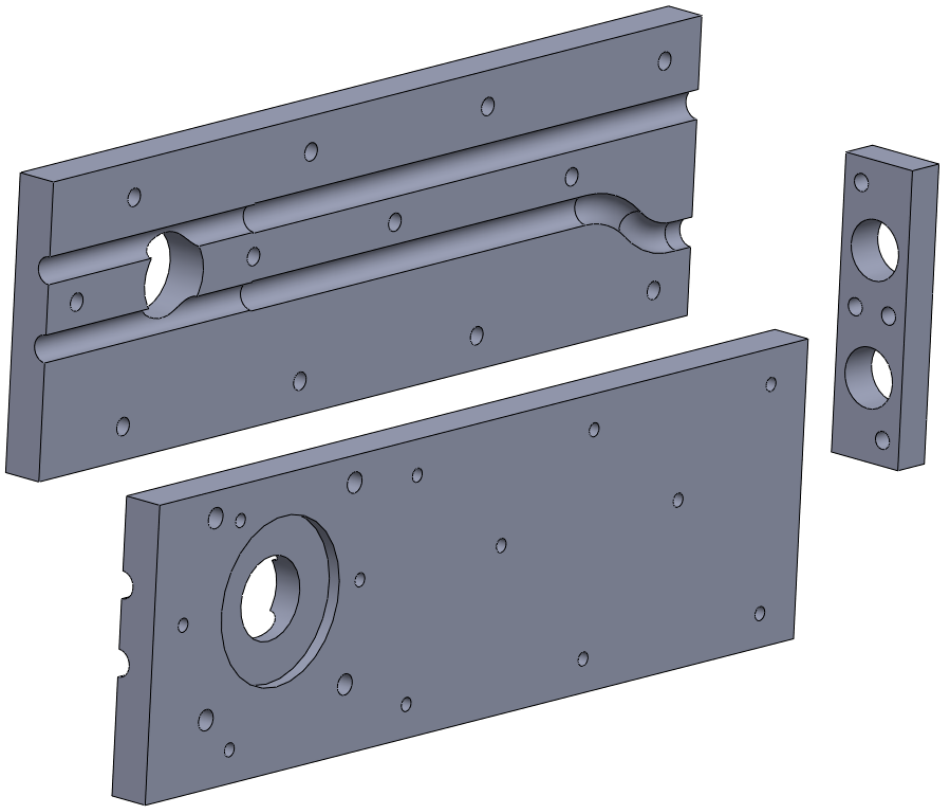

Figure 6.4.3. Actuation block designed for CNC production.

Flexural modulus of elasticity is the most important strength factor because the low profile design requires thin plastic parts which span up to 5 cm in each direction without support. Impact strength is important to prevent deformation of the impact surfaces from

operation of the robot. This is especially important in the parts of the robot which are acted upon by the motion elements. Tensile strength is less significant than the previous strength measurements because none of the components are designed to operate in tension. However, tension may occur under some external force applications during handling or operation, and tensile strength is a commonly used comparator for material strength. Dielectric strength was considered for these plastics because it is a requirement of this design that the plastic parts inside of the MR environment do not conduct electricity. Those plastics with high dielectric constants should provide better electromagnetic isolation.

The eleven plastics compared include: polyetheretherketone (PEEK), polyetherimide (Ultem), self-lubricating nylon (SLN), Delrin (specialized acetal homopolymer manufactured by DuPont), glass-filled Delrin, type II polyvinylchloride (PVC), ultra-high molecular weight plastic (UHMW), glass-filled UHMW, high-density polyethylene (HDPE), polytetrafluoroethylene (PTFE), and glass filled polycarbonate. The mentioned glass-filled materials have 20% glass added during the manufacturing process. Values for the five previously mentioned mechanical and electrical characteristics were acquired through the MatWeb online material database and compiled in the table 6.4.1 below for these twelve materials. When a range or multiple results were given, data was selected from room temperature test conditions, or a given average if available.

In order to determine the best all-around materials from each of the material properties exclusion criteria were developed to eliminate some of the materials based upon the properties in the table. A simple exclusion criterion used was to eliminate

materials based upon the averages shown at the bottom of the table. All materials with below average elasticity, impact strength, or tensile strength were first eliminated. Next all materials with above average friction were eliminated. Elimination was not performed based upon dielectric constant the data was pretty well clustered around the average. Elimination of these rows containing these exclusion data yielded only one remaining material which was Delrin.

Table 6.4.1 – Material Property Comparison

Material	Flexural Modulus of Elasticity (PSI)	Friction Coefficient	Impact Strength $\left(\frac{\text{ft·lbs}}{\text{in}}\right)$	Tensile Strength (PSI)	Dielectric Strength $\left(\frac{kV}{in}\right)$
Delrin	421,000	0.2	4.76	10,400	435
Delrin (G)	725,000	0.35	2.86	7,690	452
HDPE	116,000	0.2	1.31	1,890	300
PEEK	508,000	0.34	1.2	14,100	480
Polycarbonate (G)	900,000	0.62	2.0	12,200	765
PTFE	71,900	0.1	3.54	4,000	500
SLN	457,000	0.16	0.843	12,000	400
Type II PVC	350,000	0.6	8.45	5,500	152
UHMW	100,000	0.147	14	2,900	1000
UHMW (G)	112,000	0.14	NB[α]	4,800	2300
Ultem	480,000	0.65	1	15,200	498
Average	*408,992*	*0.32*	*3.94*	*7,254*	*469*

[α] NB indicates that no break occurred during the test.

A ranking method was also used to verify that Delrin was the best selection of the compared materials. Table 6.4.2 shows the rank of each material by category based upon the data of Table 6.4.1. A rank of 1 is the highest therefore lower is better. The normalized rank, shown in the table, is the overall rank of the material all material properties were considered equally. The modulus of elasticity and coefficient of friction

are most important however, so a weighted rank was also established in the last column. The weights for elasticity, friction, impact strength, tensile strength, and dielectric strength were selected as: 2.0, 2.0, 1.0, 0.5, and 0.5 respectively.

Table 6.4.2 – Material Property Rank

Material	Flexural Modulus of Elasticity (PSI)	Friction Coefficient	Impact Strength $\left(\frac{\text{ft·lbs}}{\text{in}}\right)$	Tensile Strength (PSI)	Dielectric Strength $\left(\frac{V}{mil}\right)$	Normalized Total Rank	Weighted Rank
Delrin	7	5	4	5	6	4	3
Delrin (G)	2	6	7	8	5	4	2
HDPE	9	5	8	12	9	9	10
PEEK	4	6	9	2	4	3	4
Polycarbonate (G)	1	7	2	3	2	1	1
PTFE	12	1	5	9	3	6	5
SLN	6	4	10	4	7	7	8
Type II PVC	8	7	3	7	10	8	7
UHMW	11	3	2	10	8	8	6
UHMW (G)	10	2	1	9	1	2	1
Ultem	5	8	1	1	3	5	9

The result of the total rank places Delrin fourth behind glass-filled polycarbonate, glass-filled UHMW, and acetal. However, the weighted rank places Delrin third behind some glass-filled composites and acetal. In addition to these five characteristics, machinability and cost must also be considered.

Although the results of Tables 6.4.1 and 6.4.2 demonstrate the results of glass filled composites, such as improved strength and electric insulation properties [108], further research indicated they may not be suitable for our application. The machinability of glass-filled composites is reported to be problematic since the glass fibers cause the

plastic to be more abrasive. Problems include delamination of the material, thermal expansion, and disruption of the fibers which causes a fuzzy surface [109]. These three effects of manufacturing glass filled materials will most likely cause tolerance or surface roughness issues which will impede the motion of SMFT motion elements within the robot. In addition to causing problems our application specifically, thermal expansion and abrasive fibers will quickly damage tooling and glass filled materials were not an option at many of the machine shops which were contacted for quotes. In light of these facts, glass-filled composites were excluded from the selection process and remaining materials and ranks are shown in Table 6.4.3.

Table 6.4.3
Mechanical Property Rank (Reduced Set)

Material	Normalized Total Rank	Weighted Rank
Delrin	2	1
HDPE	7	8
PEEK	1	2
PTFE	4	3
SLN	5	6
Type II PVC	6	5
UHMW	6	4
Ultem	3	7

With the exclusion of glass-filled composites, the top three materials for the total rank are PEEK, Delrin, and Ultem and for the weighted rank the top three materials include Delrin, PEEK, and PTFE. The final deciding factor in material selection, cost, is shown in Table 6.4.4 for each material. The cost shown represents the cost of a square sheet of material with ½ inch thickness and 12 inch length and width. As shown in the

table, the cost of PEEK, PTFE, and Ultem are significantly greater than Delrin confirming that Delrin will be used for all of the plastic manufactured parts in this design.

Table 6.4.4
Material Cost

Material	Cost (dollars per sheet)
Delrin	100
HDPE	35
PEEK	910
PTFE	545
SLN	90
Type II PVC	50
UHMW	70
Ultem	290

7. Shielding and Filtering to Reduce Artifacts

7.1 Signals and Cabling

Motor controls signals and encoder output signals must be passed outside the MRI room through cables of at least 10 m in length. The motor cables carry square wave signals with frequency of up to 20 khz and voltage as high as 60 VDC. Encoder cables carry lower voltage square waves at 5 VDC with similar frequency. Differential signaling is used in all of the transmission lines for these projects to reject external noise, and maintain signal integrity over the long transmission lengths. This is accomplished by sending each signal through a differential pair. One line contains the original signal (V_s), and one line contains the compliment of the signal ($\overline{V}_s$). Any external noise applied to the transmission line theoretically be applied to both wires in the pair. Since the pair are

complementary, using digital logic there only exists one line which is logic high and one line which is logic low for any given time. The differential value of the signals at any given time is measured as $V_D = V_s - \overline{V}_s$. Therefore, if external noise is applied to the two lines simultaneously, both wires of the pair will contain the noise, but V_D will not because the difference between the two pairs will remain the same. In the case of encoding signals this was accomplished through the use of differential sender and receiver integrated circuits AM26C31 and MC3486N by Texas Instruments. In the case of the motor signals, the differential pair is generated by the stepper driver, and supplied to the motor coils directly as the signals to the motor poles.

All of the signals used in these projects were found to be highly susceptible to crosstalk amongst themselves due to their digital square wave implementations. The very short rise time of these signals generates enough magnetic flux to induce the signal for one wire into each of its neighbors as noise. Figure 7.1.1 contains a typical motor drive signal, which is a 20 kHz square wave. A peak to peak voltage of 18 volts and cable length of 1 ft. were used in these experiments. The final prototypes will use voltages as high as 48 volts with cable lengths as long as 50 ft. However, even in these simple experiments crosstalk exists. First, a chopper drive and motor are connected using untwisted shielded cable. The shielding is only applied to the outside of the cable bundle

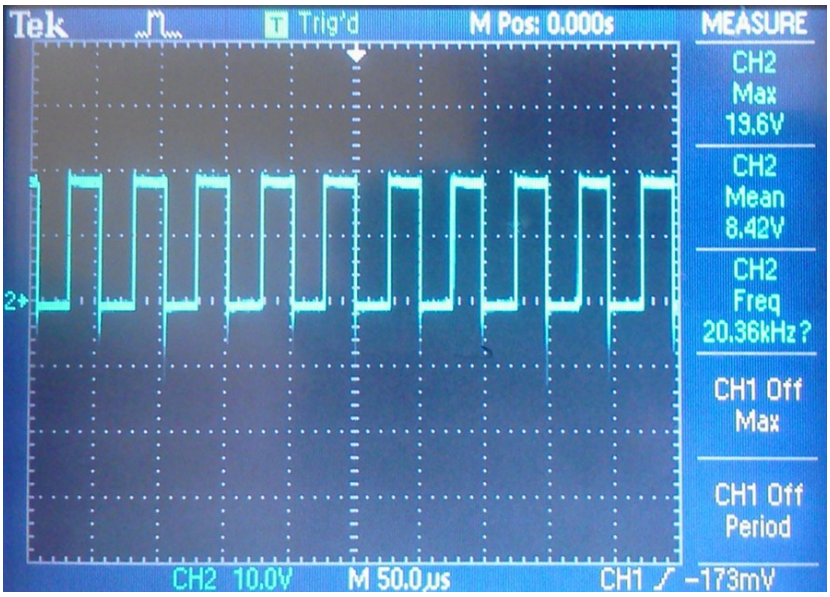

Figure 7.1.1. Motor drive signal output from chopper drive.

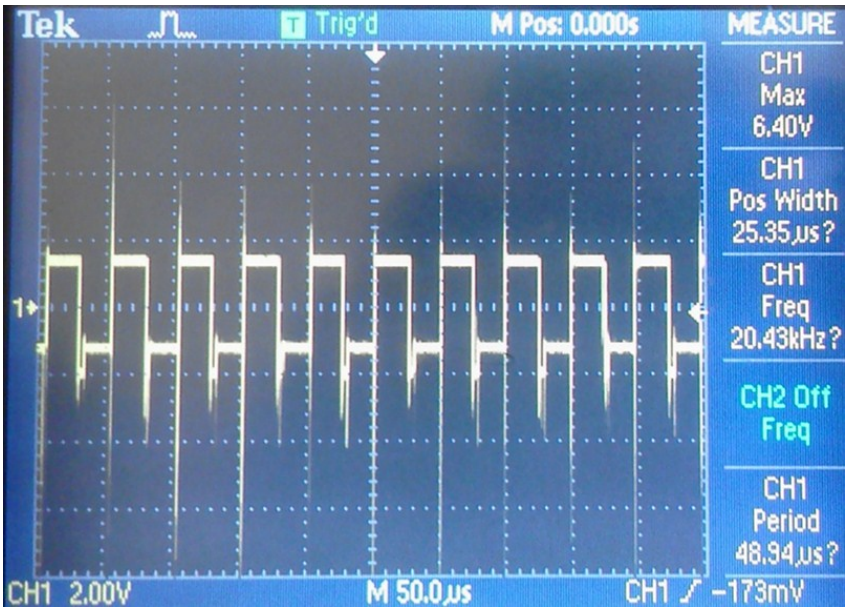

Figure 7.1.2. Crosstalk signal induced into a neighboring conductor from a motor drive signal. Induced signal is greater than 10% of the original.

as a whole, not individually. The resulting crosstalk, shown in Figure 7.1.2 appears to be the same shape as the original signal except with the addition of ringing as a result of high frequency losses. The peak to peak amplitude of the signal is in excess of 2 volts or

greater than 10 percent of the original signal. These results demonstrate significant noise is being induced into neighboring conductors.

In the next experiment, the same signal was passed through a twisted pair cable without shielding. In an attempt to reduce crosstalk, each differential pair was run as a twisted pair. Complimentary signals will have complimentary magnetic flux, by twisting the pair together along the length of the cable, the flux radiated from one of the pair is partially cancelled by the complimentary cable in the pair. Comparison of Figure 7.1.2 to Figure 7.1.3 below demonstrates the reduction in crosstalk noise from the use of a twisted differential pair.

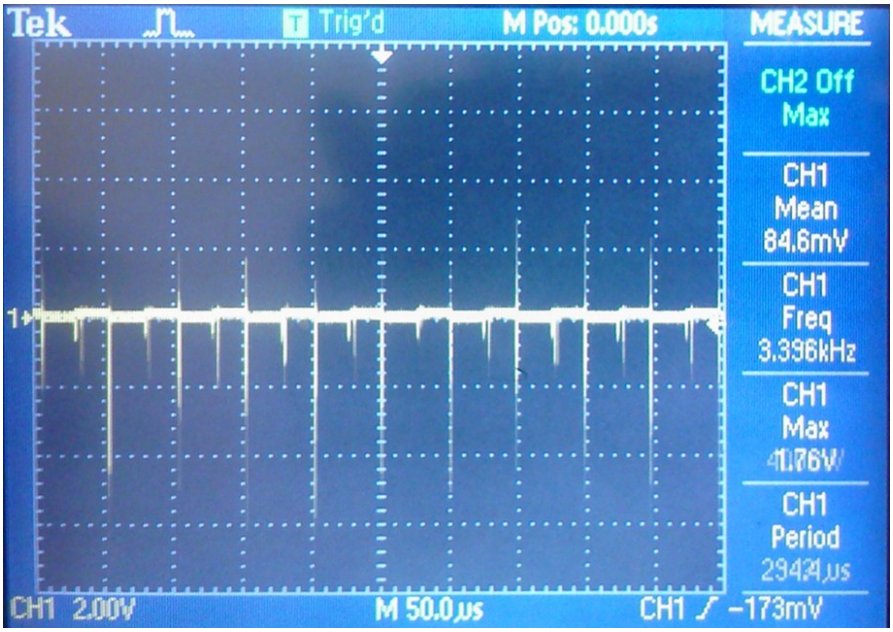

Figure 7.1.3. Crosstalk signal induced into neighboring conductor from motor drive signal is reduced by using a twisted differential pair.

Additional reduction can be achieved from shielding of the pairs. In this next experiment, each pair is shielded in a foil sheath to further reduce the remaining noise emitted from the pair. In order for the shielding to be effective, the shield must be connected to the ground of the noise source. In this experiment, crosstalk is measured in a

neighboring conductor of a neighboring pair in a shielded twisted pair cable with the shield floating and connected to ground respectively in Figure 7.1.4 and Figure 7.1.5 respectively. In the case that the shield is not grounded, the results appear almost identical to the unshielded results of Figure 7.1.3. However, with the grounded shield noise was almost completely eliminated.

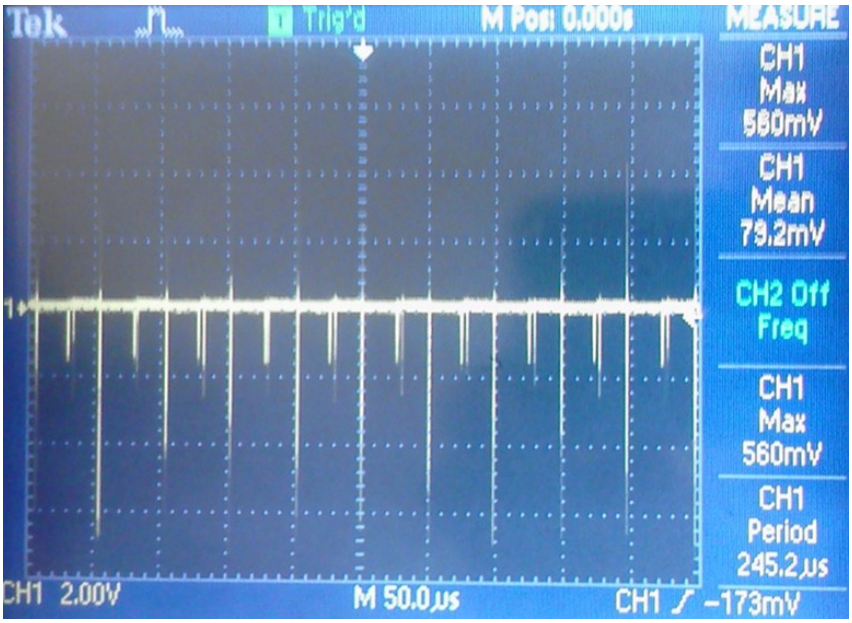

Figure 7.1.4. Crosstalk signal induced into neighboring pair when shield is not grounded.

In the case of the encoder wires, four pairs are used per cable, and for the motor wires two pairs are used per cable. The pairs are shielded individually as well as collectively with another grounded shield to reduce the noise induced into the surrounding environment which could be picked up by the MR scanner. Wire shielding is electrically continuous from the motor actuation block back to the motor driver box located outside of the MR scanner room. This implementation is shown in Figure 7.1.6 below. Copper tape was used to shield the short sections of wire between the motors and the shielded twisted pair cable. The metal actuation blocks and motor casing were also

grounded through the wire shield as shown. The copper tape is connected to the shielded twisted pair cable (yellow) through two of the four conductors in the white connector.

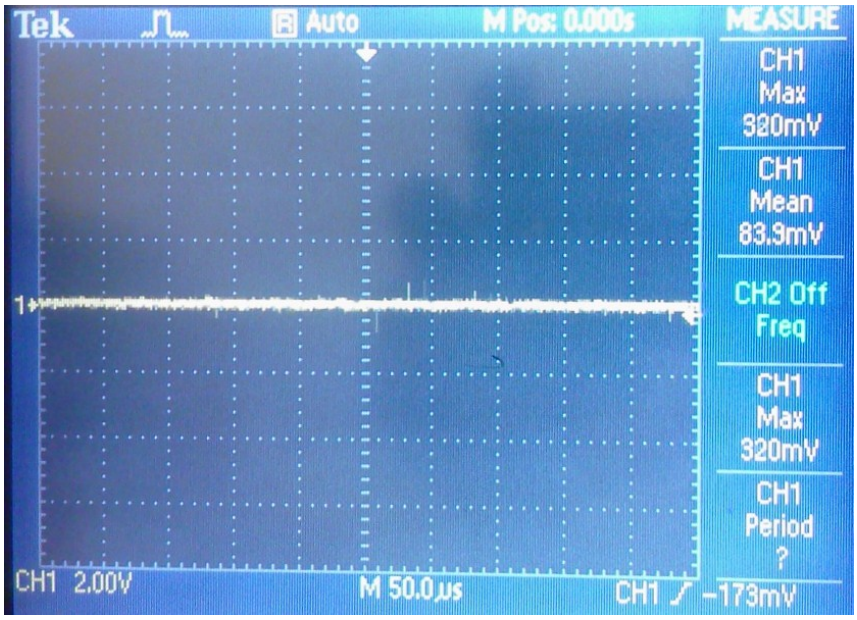

Figure 7.1.5. Crosstalk mostly eliminated using a twisted pair with shielded ground.

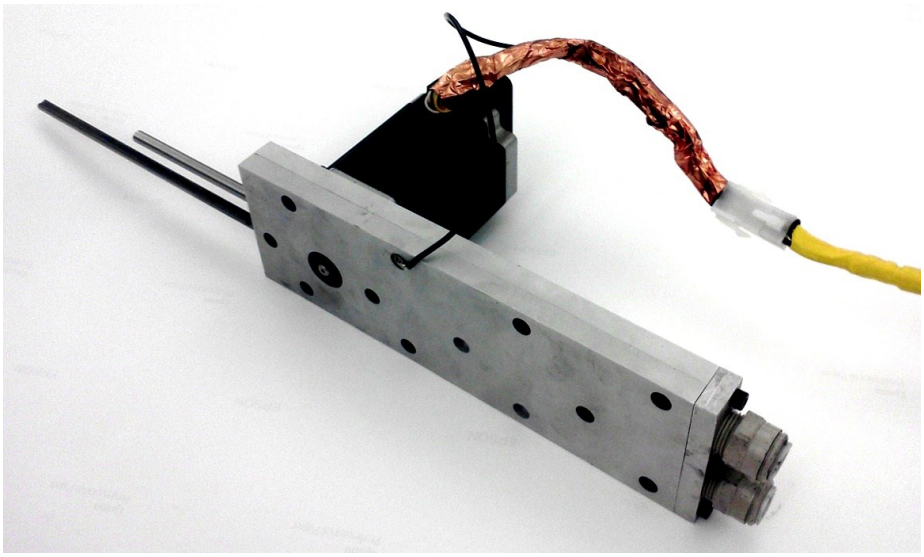

Figure 7.1.6. Motor casing, actuation block, and copper shielding tape, and wire shielding are electrically continuous to ground.

7.2 Encoder Signal Conditioning

In spite of the methods of the previous section, occasional noise was still measured in the encoder signals. Noise in the encoder signal causes inaccurate position readings which could affect accuracy, or if severe cause system instability. To overcome such noise, a simple module was developed in Verilog to essentially debounce the incoming encoder signals. Noise was measured to be in the order of nanoseconds using an oscilloscope. Since the encoder signals will never exceed a frequency of 1 MHz, a simple piece of code was generated to reject changes in the encoder signals which have a duration shorter than 1 microsecond. This was accomplished using a 64 bit shift register and a check condition to validate that all 64 bits have the same value before the register storing the encoder value is changed. This simple method, which was proven to be effective, requires 27 combinational units and 65 dedicated registers to implement on the FGPA. The hardware synthesis of such a circuit is shown in Figure 7.2.6 as a 2-bit example.

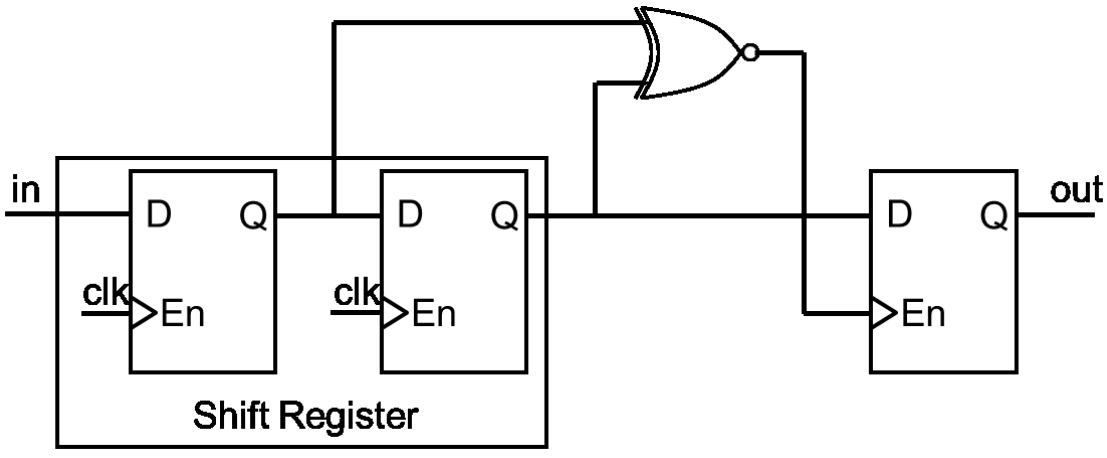

Figure 7.2.6. 2-bit example of hardware synthesis of the debounce circuit used to filter the encoder signals. Actual implementation was 64 bits.

7.3 Motor Signal Conditioning

Imaging experiments revealed that the operation of the stepper motors inside the MRI room introduced noise and artifacts to the acquired MRI images. The zipper artifacts which appear in the acquired images of Figure 7.3.1 below are typically introduced by

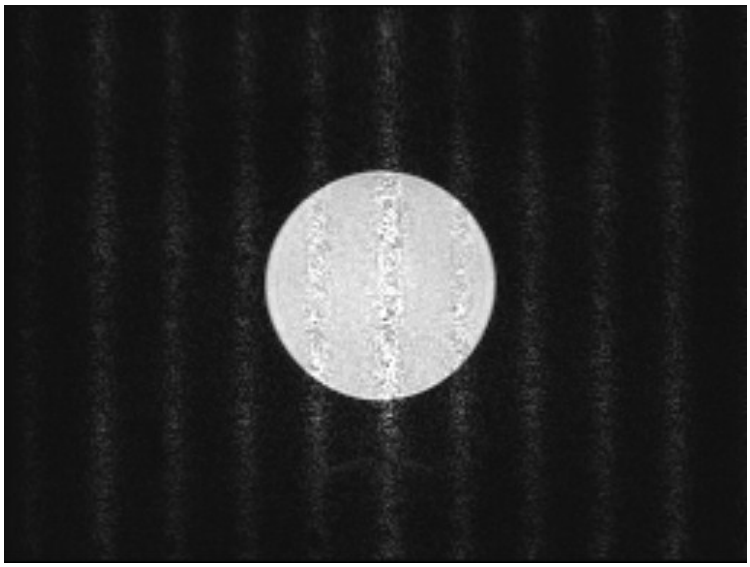

Figure 7.3.1. Zipper artifacts induced by stepper motors.

radio frequency (RF) interference [110] i.e. the operation of the motors emits electromagnetic radiation within the bandwidth of the MRI pickup coil. Filters were designed and implemented on the motor drive signals to reduce the noise.

The MRI pickup coil, which is used to acquire the signal emitted from precession of atoms as part of the MRI imaging process, has a center frequency equal to the Lamor frequency. The Lamor frequency describes the precession in response to an external magnetic field, as

$$f_{Lamor} = \gamma B, \tag{7.3.1}$$

where γ is the gyromagnetic ratio of the atomic element, and B is the magnetic field [111]. The Lamor frequency of the various elements which may be scanned using the Siemens MAGNETON Avanto 1.5 T scanner are given in Table 7.3.1 [112].

TABLE 7.3.1
LAMOR FREQUENCY FOR VARIOUS ELEMENTS

Periodic Element	Frequency (Hz)
Carbon	16.0
Sodium	16.8
Xenon	17.6
Lithium	24.7
Phosphorous	25.7
Helium	48.4
Fluorine	59.8
Hydrogen	63.6

Examination of the motor drive signals revealed that the motors operate from a PWM signal with a typical frequency range of 20 KHz to 30 KHz. These emissions are at the low end of the RF band and far from the Lamor frequency for 1.5 T MRI. The bandwidth of the pickup coil is dependent upon the pulse sequence used to collect the images, but a passband larger than 250 KHz is rare [113]. Although the operating frequency of the motor is not within the bandwidth of the MRI pickup coil, it is known from the Fourier expansion that an ideal square wave signal is an infinite sum of the odd harmonic components. The Fourier expansion of a square wave with period L [114] is given by

$$f(x) = \frac{4}{\pi}\sum_{n=0}^{\infty}\frac{1}{2n+1}\sin\left(\frac{(2n+1)\pi x}{L}\right). \tag{7.3.2}$$

It can be seen from (7.3.2) that the amplitude is reduced proportionally for each harmonic (2n+1). Therefore, harmonic of a 30 KHz square wave with frequency within the

passband of 63.6 MHz ± 250 KHz would have an amplitude reduction larger than 2000 times or -66 dB power reduction. Although the power output of this harmonic is relatively small, the MRI makes use of a high power RF amplifier to pick up precession signals during the scanning process. The precession signals, which are in the order of microwatts μW are amplified by up to 80 dB by the RF amplifier [113]. Due to this amplification it is clear that the motor drive signals should be filtered to attenuate signal within the bandwidth of the MR receiver coil.

According to Table 7.3.1, a 1.5 T MRI machine could be used to pick up frequencies between as low as 15 MHz and as high as 67.6 MHz. Although a notch filter could be used in this application, a low-pass filter was selected in order to be robust toward future high field scanners. Higher field scanners such as 3T or 7T scanners would receive frequencies in the range of 30 MHz to 128 MHz and 70 MHz to 294 MHz respectively according to (7.3.1). For best performance, it is desired that the attenuation at 15 MHz be 80 dB or higher to compensate for the amplification of the RF amplifier on the 1.5 T machine, and since filter response is typically 20 dB per decade for each order of the filter [115], a filter order of 2 or higher is required. A passive Butterworth filter topology was selected for its flat passband which is desired to prevent adding any unwanted gain to the motor control signals which could cause heating problems.

Even though the Butterworth filter theoretically provides a flat passband, the selection of the filter cutoff frequency is very important to maintaining this feature. Any low pass filter will reduce the power of certain harmonics in the square wave drive signals which will distort the square wave and could cause excessive ringing or overshoot as described by the Gibbs Phenomenon. Undesired phase delay could also result from the

choice of cutoff frequency. These potential problems are demonstrated by Figure 7.3.2 below which shows the potential effect of filtering at different cutoff frequencies. It is desired therefore, to select the highest cutoff frequency which will still meet the attenuation requirements. The use of higher order filters would allow for selection of a higher cutoff frequency.

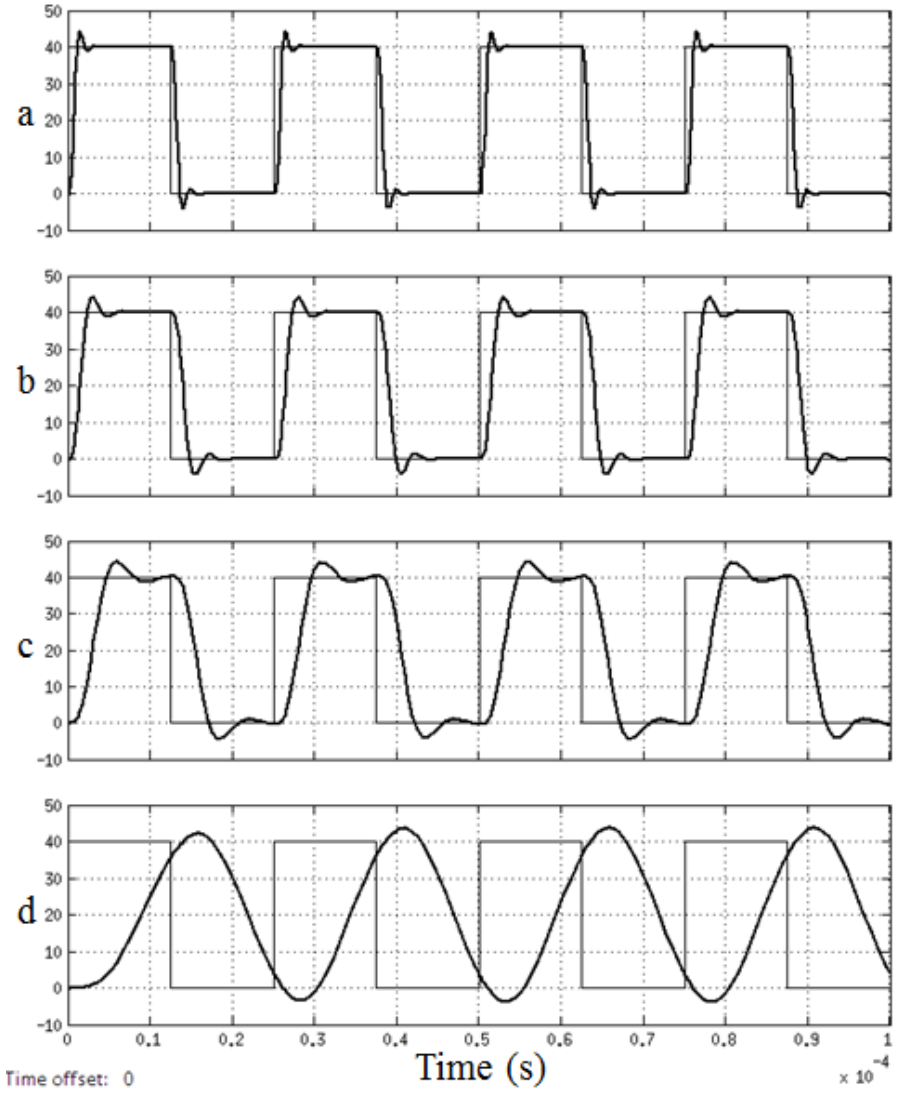

Figure 7.3.2. Simulation of filtered square waves for cutoff frequencies of a) 600 KHz b) 300 KHz c) 150KHz and d) 50 KHz using a fourth order Butterworth low pass filter.

A typical Butterworth filter implementation using RC ladder circuits is shown in Figure 7.3.3 below. The order of the filter depends on the numbers of inductors or capacitors. The values of these components, are well documented in lookup tables for a normalized filter circuit which can be denormalized according to the following scaling factors [116]

$$C_D = \frac{C_N}{R_O \omega_0} \tag{7.3.3}$$

$$and\ L_D = \frac{R_O L_N}{\omega_0}, \tag{7.3.4}$$

where C_D and C_N refer to the denormalized and normalized capacitor values, L_D and L_N refer to the denormalized and normalized inductor values respectively, R_O refers to output resistance, and ω_0 refers to the cutoff angular frequency. These relationships are important tools for the selection of components to fit the electrical needs of the circuit.

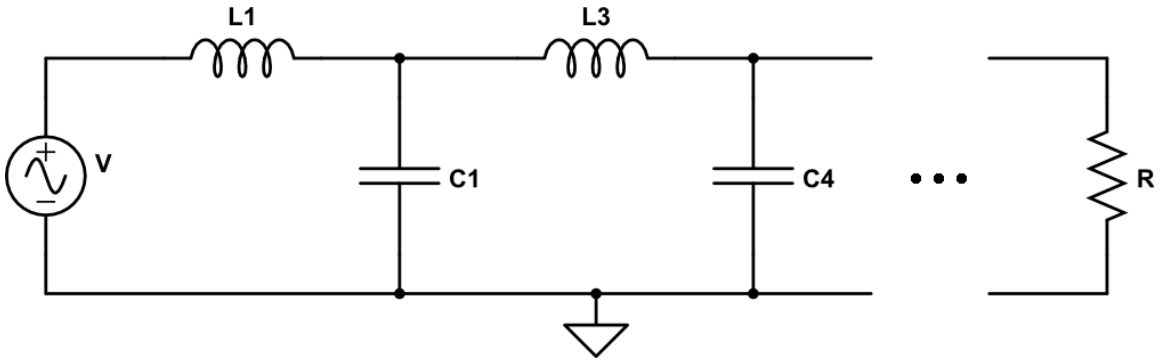

Figure 7.3.3. Generic RC ladder circuit used to implement Butterworth low-pass filter.

One constraint with the motor driver circuit compared to the filter above is that there is no specific ground wire in the motor driver circuit. The motor drive signals consist of four signals which are sent as two pairs. Each pair acts on a motor coil with alternating current, that is while one of the pair is high, the other acts as ground. This proved to be a major complication in the design of an appropriate filter. The schematic of

a pair of motor signals to drive one motor coil is shown in Figure 7.3.4. Figure 7.3.5 shows the substitution of a two pole Butterworth filter into the design.

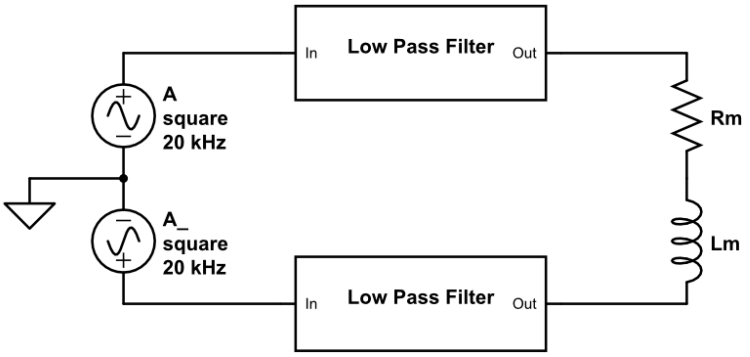

Figure 7.3.4. Diagram of motor driver as AC voltage sources, low pass filters, and stepper motor which is modeled as a resistor Rm and inductor Lm.

It can be seen that the components C1, C2, R1, and R2 will be passing current away from the motor and straight to ground which will reduce current applied to the motor and directly reduce the performance. Also, since most stepper motor drivers perform current sensing it is important to minimize the current lost through these elements to prevent adverse effects. It can also be seen from the above figure that the circuits are coupled by the motor coil i.e. inserting the filter on the A driver output affects the ability the A_Bar driver output to pull the coil low. An equivalent circuit is shown in Figure 7.3.6 to describe the case when current flows through the motor from A to A_Bar. In this case A_Bar is assumed to be ground. Components with equal value in the circuit have been renamed to have the same name.

The proper components were chosen following several constraints. The first constraint is that R must be larger than Rm to maintain the proper output impedence of the filter. Since Rm was measured to be between 0.5 ohms to 10 ohms depending on the motor, this constraint was easy to fulfill. The second constrain is that C passes as little

current as possible to ground so that current flows through the motor coil and not to ground. The current through a capacitor is described by the equation

$$i(t) = C\frac{dV}{dt}\ , \tag{7.3.5}$$

where i is current, V is voltage, C is capacitance, and t is time. The maximum change in voltage over time is dependent upon the inductance of L, however in the worst case we can assume it to be the rise time of the motor drive signal A. The maximum voltage of the driver is 40 VDC with the current power supply and the rise time was measured to be 20 ns. If the RMS current passed through the capacitor should be in the order of

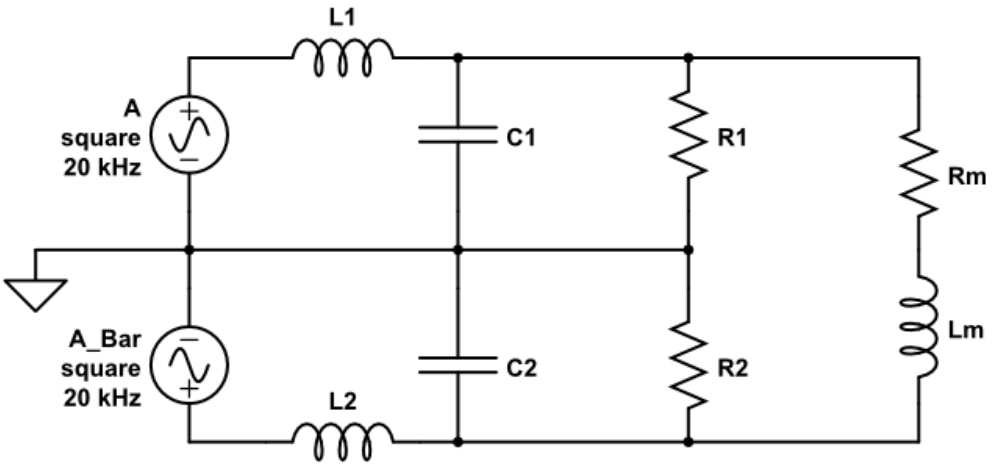

Figure 7.3.5. A second order filter placed on each side of the motor coil.

milliamps, the capacitance cannot exceed 1.4 nF according to (7.3.5). Based upon these two constraints, and commercial availability, components were selected Using the normalized component values from the lookup tables, and the relationships of (7.3.3) and (7.3.4) charts can be generated to aid in the selection process. The following chart, Figure 7.3.7 was generated for a second order filter with 150 KHz cutoff frequency.

Filters with varying cutoff frequency and order were tested using one NEMA 24 motor in the 1.5 T MRI. The approximate cutoff frequency, order, and theoretical

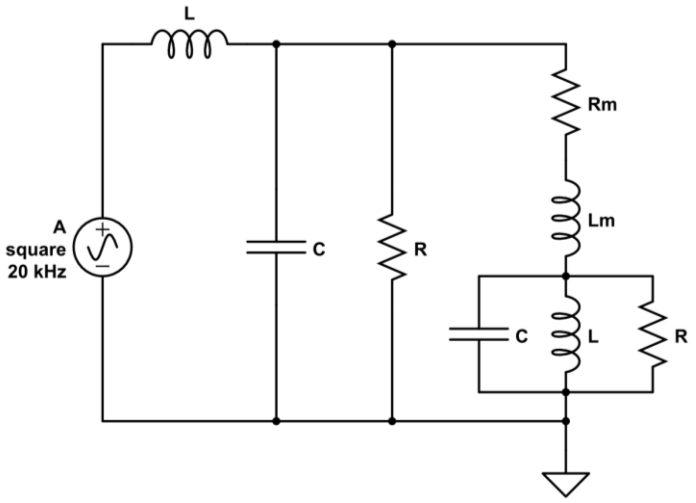

Figure 7.3.6. Equivalent circuit when current is flowing from A to A_Bar and A_Bar is assumed to be equivalent to ground.

attenuation of each filter is listed in Table 7.3.2. Note that the first order filter consists an inductor placed in series at the beginning of the transmission cable for each motor control signal. Also the cutoff frequency of the first order filter is far below the operating frequency of the motors, this was required to maintain proper attenuation in the MHz

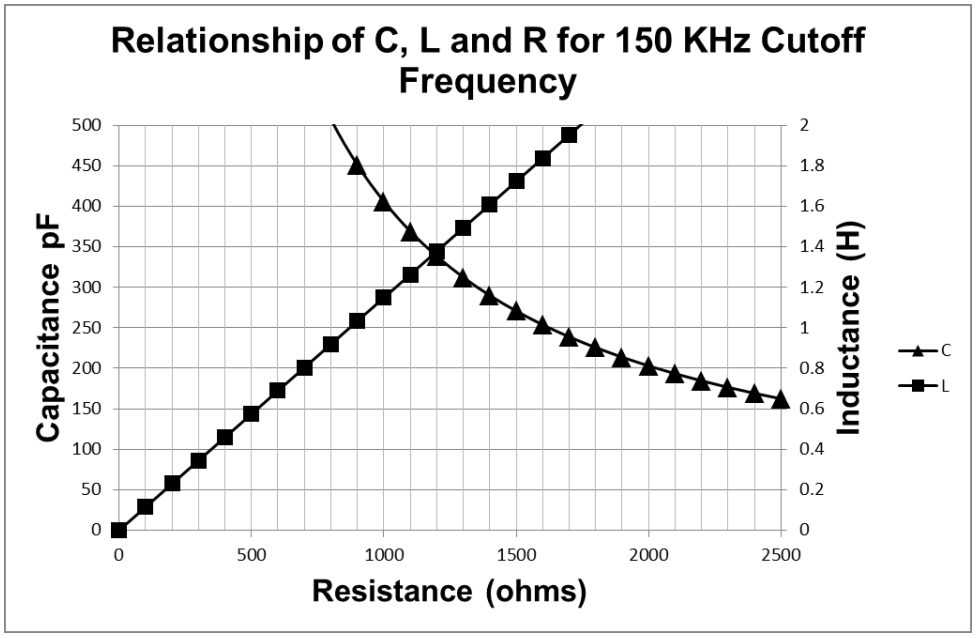

Figure 7.3.7. The relationship of C, L and R was used to select commercially available components to achieve a cutoff frequency of 150 KHz.

frequency bands. The roll-off of the first order filter is low and there was no apparent change in motor operation with or without the first order filter.

TABLE 7.3.2
FILTERS TESTED

Order	Approximate Cutoff Frequency (KHz)	Approximate Theoretical Attenuation at 60 MHz (dB)
1	1	>80
2	150	>80
3	250	>120
4	300	>160

Imaging tests were performed using a single NEMA 24 motor located 4 meters away from the MRI scanner. The motor drive signal cable was passed through the waveguide in the wall of the MRI room around the perimeter of the room to the motor. Figure 7.3.8 shows the location of the motor and cable routing which was maintained for each of the experiments performed within this section.

SNR reduction for each of the filters is plotted in Figure 7.3.9. Average SNR over 30 consecutive frames was calculated using the methods described in Section 7.4. The MRI images were taken of a contrast agent bottle phantom using a body coil and T2 weighting with a repetition time of 41.86 ms and echo time 1.41 ms. The scanning frequency was 63.6 MHz and a pixel bandwidth of 930 Hz per pixel over 256 pixels, which means the overall bandwidth was less than 250 KHz. These experiments were performed with the motor idle at 40 volt operation. The mean SNR for the baseline scan was measure to be 536. In addition to the surprisingly low SNR measurements achieved by using the filters, two surprising outcomes are apparent from the figure. First, the best

Figure 7.3.8. Robot in the MRI scanner with actuation of 1 DoF. The motor location and wire routing were maintained for all compatibility experiments.

SNR results occurred from the use of the first order filter rather than the higher order filters. Second, according to these results, the second order filter actually created more noise than was present without any filter at all. It is apparent from the SNR results that these high order filters are not properly attenuating the high RF frequencies measured by the MRI pickup coil.

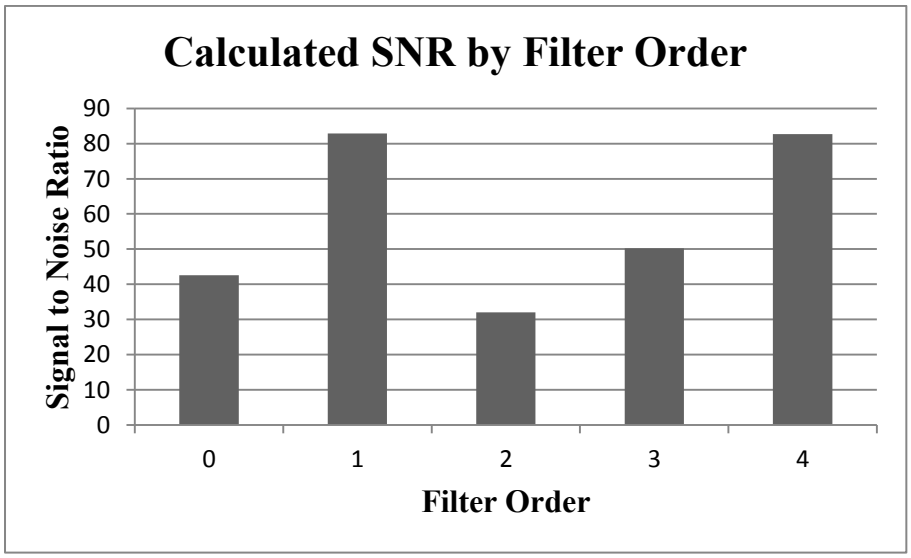

Figure 7.3.9. SNR results for each of the tested filters listed by order.

To find the source of the noise, the output of the filters based upon various inputs was inspected using a function generator. Figure 7.3.10 shows the input of a 3 MHz

square wave (yellow) and the resulting output (blue) for the 3rd order filter. It is apparent from the figure that the 3 MHz wave is indeed attenuated, but a high frequency output still exists which is estimated to be approximately 100 MHz. The circuit diagram of the third order filter and the theoretical magnitude Bode plot are shown in Figure 7.3.11 and Figure 7.3.12 respectively. The theoretical attenuation at 100 MHz is greater than 140 dB therefore the expected magnitude of the 100 MHz signal should be on the order of nanovolts, not millivolts. These results prove that in fact the filter is not effective at attenuating high RF band frequencies, in fact results show that that this filter begins acting as a high pass filter at high frequencies.

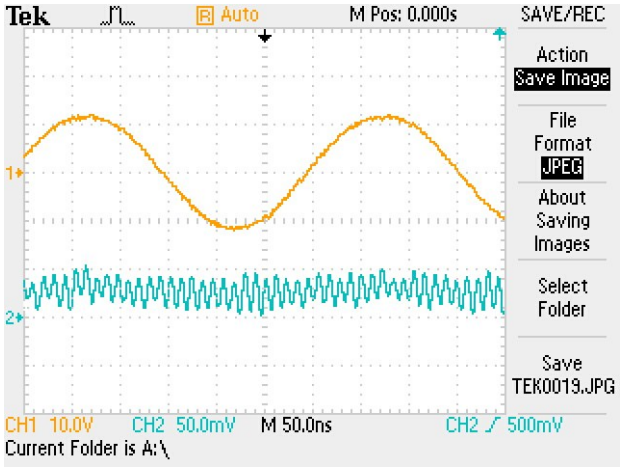

Figure 7.3.10. Input 3 MHz sine wave (yellow) and output sine wave of approximately 100 MHz (blue) for the third order low-pass filter.

One theoretical explanation for this is that the inductors and capacitors used in these filters have a self-resonating frequency which is lower than 60 MHz. The impedance of the actual physical components is not ideal. In fact, the impedance curve which should approach zero at infinite frequency for a capacitor, and should approach infinity for an ideal inductance has an inflection point about the self-resonating frequency. Since the impedance curve is mirrored around the self-resonating frequency, it can be

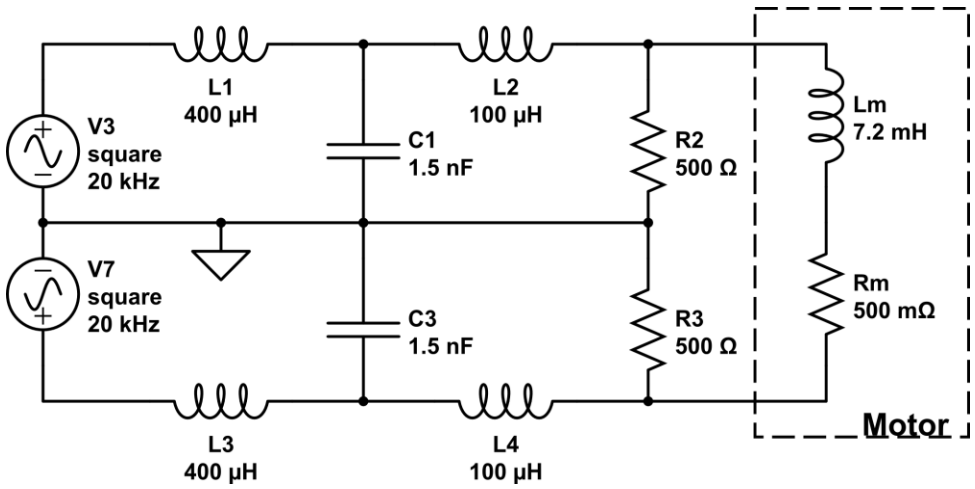

Figure 7.3.11. Circuit diagram of the third order filter with actual component values.

said that beyond this frequency the capacitor begins acting as an inductor and the inductor begins acting as a capacitor. This is demonstrated by the example impedance curves from a datasheet for a ceramic capacitor (KEMET Electronics Corporation) shown in Figure 7.3.13. It is also seen from the figure that the impedance of the actual capacitor is never zero, and the minimum impedance increases as capacitor size decreases. Due the previously mentioned capacitor size constraint which requires the use of 0.0014 uF or smaller capacitors, the filter will never perform at theoretical value.

Choice of inductive components is equally as important and inspection of datasheets for devices with similar current ratings revealed that the self-resonating frequency was lower for components of higher inductance. This corresponds to the trend seen in the SNR results because as the filter order was increased, lower value inductors were utilized. These realizations lead to the following experiments which were conducted to test the effectiveness of filtering in multiple stages rather than increasing the order of the filter. The fourth order filter of the previous experiments was used as the primary stage, and two second stage options were tested. The first option was a new second order

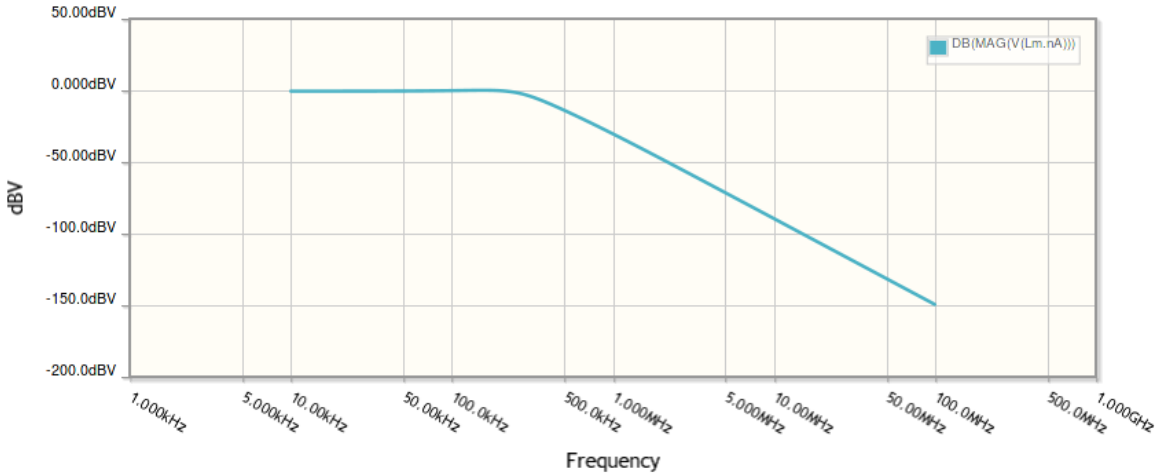

Figure 7.3.12. Theoretical frequency response of the third order filter.

filter with a cutoff frequency of 1 MHz and the second option was to use the first order filter of the previous experiments as the second stage. Average SNR calculated from 30 consecutive frames are shown in Figure 7.3.14. These measurements were made using the same protocol and settings as the previous experiments.

These results were obtained under four conditions resulting from changing the operating volts between 20 volts and 40 volts, as well as operating the motor at idle or running a continuous motion sequence. Both combinations tested showed a performance increase over the single stage filter confirming that multiple stage filtering can improve results. Also in these results, the first order filter again outperforms the second order filter used the same inductors as the first order filter, but with the addition of a capacitor, it is confirmed that the capacitors are a problem in the design. A network analyzer (Agilent 5061A) was used to inspect the fourth order low pass filter and the two-stage options and the frequency response from 300 KHz to 300 MHz is shown in Figure 7.3.15.

It is clear from the results of the S21 that in fact none of the filters were operating in their ideal theoretical conditions. Inspection of the S21 results reveals that the performance of each filter at 63 MHZ corresponds to the MRI SNR results with the 1st

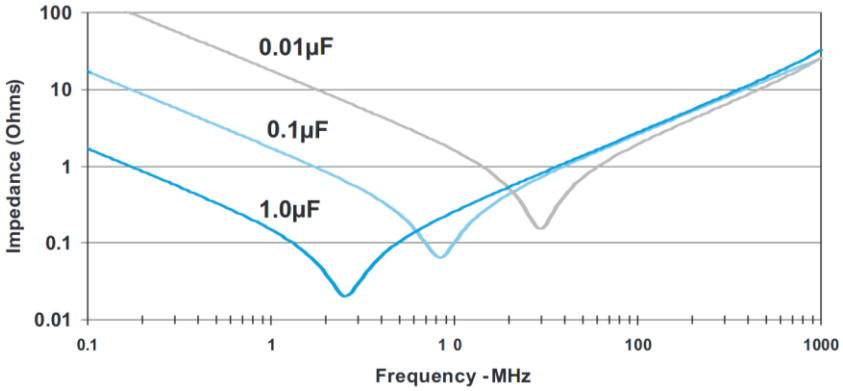

Figure 7.3.13. Impedance response depending on frequency for a ceramic capacitor.

order second stage providing the best filtering around the frequency of the MRI scan. However, since the slopes of the curves do not follow that of an ideal low-pass filter beyond, the S21 results indicate that this may be by chance, so it should be concluded that the actual impedance characteristics of the components in these tested filters played a greater role than the configuration or order of the filters. However, due to the frequency, current, and voltage requirements of this circuit, a passive Butterworth solution filter made of components with the appropriate self-resonating frequencies is not likely to be found. For reasons previously discussed, capacitance must be kept low and output resistance should be relatively high. Due to these constraints inductance must be high and in the circuits tested thus far inductance ranged between 100 uH to 1.2 mH. However, self-resonating frequency of an inductor decreases with size [117]. The various inductors used in these experiments were tested using the network analyzer it was confirmed that the measured self-resonating frequencies, which ranged from 500 KHz to 4 MHz for 100 uH to 1.2 mH respectively, corresponded to the size of the inductor.

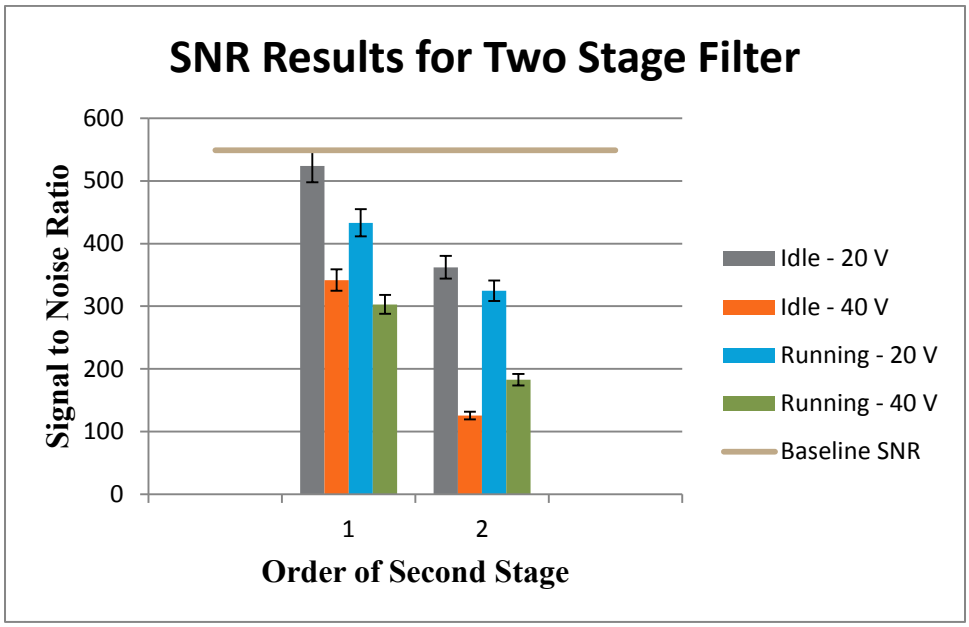

Figure 7.3.14. SNR results of a second order filter with the addition of 1) a first order second stage and 2) a second order second stage

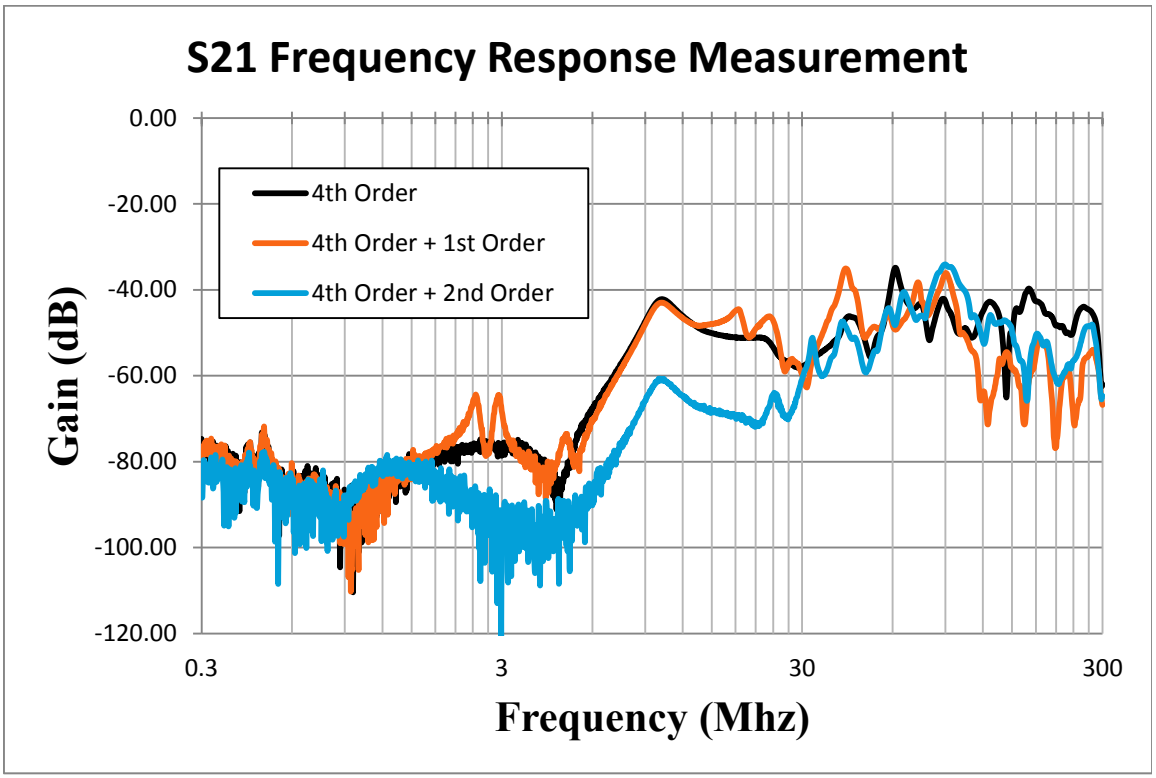

Figure 7.3.15. Frequency response of the single stage first order filter and the two-stage options tested in the MRI experiments.

Although perfect attenuation of the interfering RF signals could not be obtained using these filters, these experiments produced filters which attenuated the signal by 30 dB or greater throughout the frequency range which is received by the MRI pickup coil. It should be noted that noise to the MRI images can still be reduced further by the use of lower motor voltages, or better shielding. The results of the previously mentioned Figure 7.1.14 demonstrate significant SNR gains from the reduction of motor voltage from 40 volts to 20 volts. Using the fourth order filter in series with the first order filter achieved an average SNR reduction of 4.6% with the motor idling and 21% with the motor running a motion sequence. Select MRI images acquired during these experiments are presented in Figure 7.3.16 for side-by-side comparison.

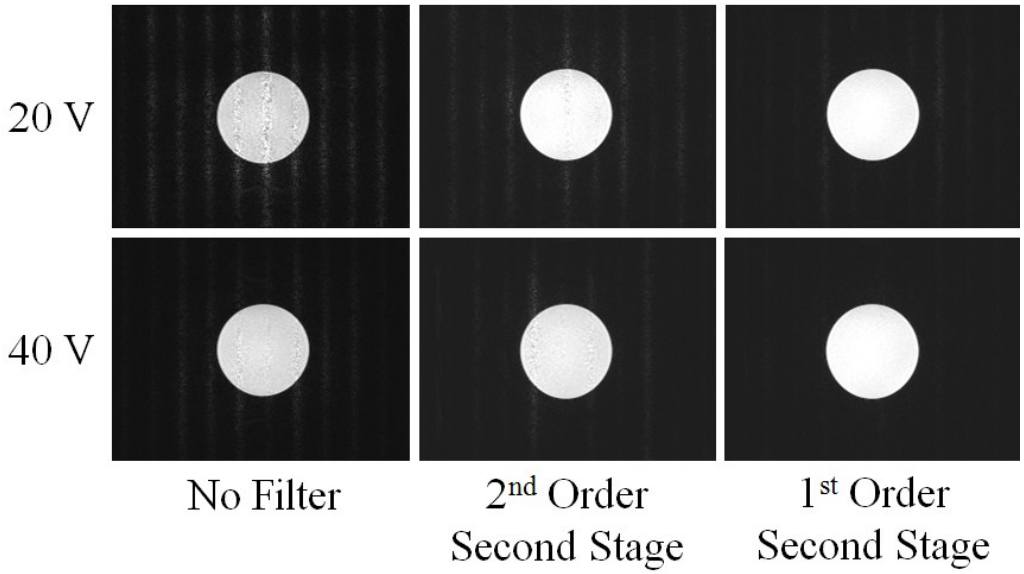

Figure 7.3.16. Side-by-side comparison of different filter and voltage combinations.

7.4 Signal to Noise Ratio Calculation

In the validation of MRI compatible technologies it is necessary to quantify the effects of the device in question on image quality. This is accomplished through the calculation and comparison of signal to noise ratio (SNR). According to the NEMA MS

1-2008 standard for SNR calculation [118], four methods can be used to calculate SNR effectively. The fourth method was chosen for all experiments within because it is the only method suitable for calculating SNR using a single image. Using this method, signal is measured as the mean pixel value within the signal producing phantom, and noise is measured from the four corners of the image, which should not contain signal or artifacts. The SNR ratio is then calculated as

$$SNR = \frac{Signal * 0.66}{Noise}, \tag{7.4.1}$$

where the constant 0.66 is a correction factor used to convert the Rayleigh distribution found in the magnitude of the MRI image to a Gaussian distribution [118].

To streamline this process and provide for easy assessment of SNR in all experimental images, a graphical user interface (GUI) was developed using C#. This software is capable of opening a single file, or directory of files obtained from the MRI scan session stored in the Digital Imaging and Communications in Medicine (DICOM) format and calculating SNR based on adjustable parameters. The GUI, shown in Figure 7.4.1, was developed from the existing open source software "DICOM Image Viewer" and modified to include sliders which allow quick and easy adjustment of the signal region size, left/right and up/down position as well as the size of the noise region. The image is updated with an overlay of the current signal region (green) and noise region (red) as well as the SNR calculated using these parameters. Buttons allow for moving forward and backward in the image directory, viewing DICOM header tags, and exporting the image in the portable network graphics (PNG) format.

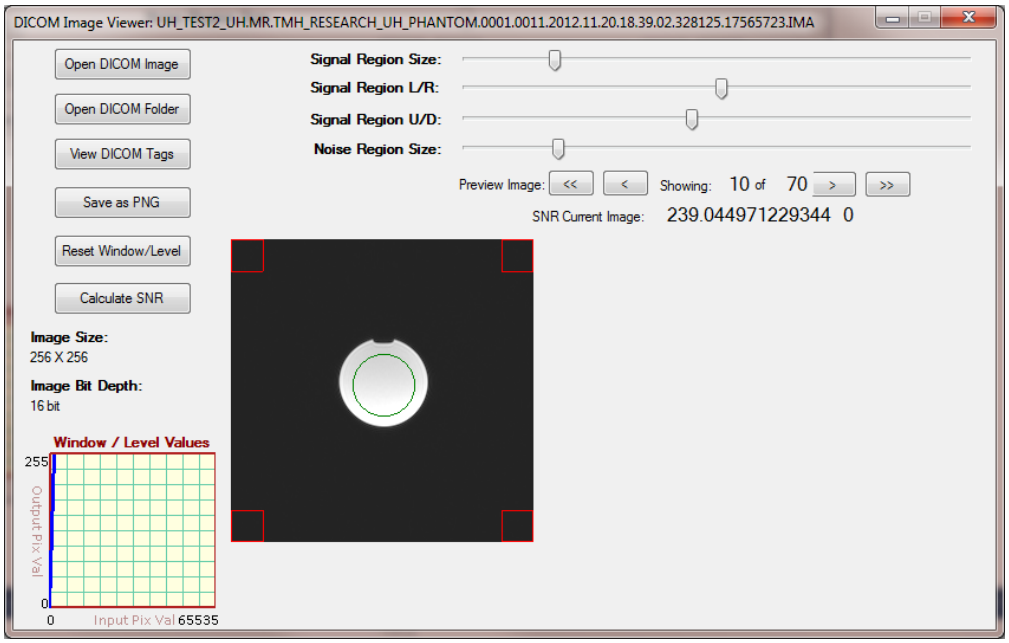

Figure 7.4.1. GUI to calculate SNR for DICOM images acquired during experiments.

8. Conclusion

This work contained several devices which were designed to be MRI compatible and several compatibility tests were performed. Image distortion was quantified by the test of SNR and compared to baseline scans. Standard deviation between consecutive frames in the baseline scans was calculated to be 5%, which provides a good measure for uncertainty. For all of the devices tested in this work, measured SNR reduction due to materials alone was less than or equal to this value. Therefore it is concluded that in regard to materials, the design approaches in this dissertation were adequate for producing MRI compatible systems. The operation of electronic systems inside of the MRI room, however, did cause noticeable interference and artifacts. These artifacts were systematically analyzed within this dissertation and shielding and filtering solutions were provided and tested. It is concluded from this dissertation that a twisted pair cabling, grounded wire shielding, and filtering can provide significant improvements. Experiments revealed that grounding the wire shield increased SNR by more than 35% for the motion phantom, and that preliminary filter designs improved SNR reduction from 92% without a filter to 38% for a 40 volt motor signal and from 73% to 5% for a 20 volt motor signal. The SNR reduction of the 20 volt idle test is equal to the uncertainty of the MRI baseline results, but slight artifacts are still present to the human eye. Challenges and constraints toward building a filter which is capable of filtering the appropriate signals out of the motor driver signals at the required current and voltage, however it is believed that in light of the analysis provided better results are achievable in future work.

Although the methods presented within this work have not yet produced image test results which are completely noise and artifact free, several comparison should be

realized between the systems tested in this dissertation and the piezoelectric motors or USM which are used in the majority of MRI compatible robot designs today. Preliminary works using USM reported SNR reduction of 40%-60% [36-38] and later publications reported that SNR reduction could be reduced to around 5% [41] using Nanomotion motors with filtered drive signals. These SNR results are comparative to the worst and best case results achieved within this work. However, the drive systems themselves have significant differences which must be noted. First of all the stepper motors used in have a nominal torque greater than 3 Nm, which is three times larger than the highest rated Shensei motor, and the HR2 motors used to achieve 5% SNR results have a nominal linear force of 7N, but the actuation blocks in this dissertation had a measured output of over 200 N without the use of a gearbox. Therefore the stepper motors can provide more force and scalability with the same performance in regard to image quality. In addition to these performance benefits stepper motors and drivers are built to industry standards and are easy to acquire at a relatively much lower cost and are interchangeable. Therefore only clear benefit that USM provides over the use of standard electromagnetic motors in MRI is that they can be constructed without the use of magnetically susceptible materials. However, with proper mounting electromagnetic motors can be safely secured in the MRI environment which is proven by the ViewRay MRI guided radiation therapy system (ViewRay Incorporated) which makes use of over 180 Maxon brushless DC servo motors in its three multileaf collimators to deliver radiation under MRI guidance [119] .

Mechatronic developments, which are not strictly coupled to MRI compatible robotics, were also presented in this work such as the new method of linear force transmission, SMFT, which can be flexibly routed in the workspace similar to pneumatic

or hydraulic lines. Unlike pneumatic and hydraulic lines, the force transmission is not subject to fluid dynamics. This novel technology has shown promising preliminary results including closed-loop positioning of a manipulator with a reported 2 mm mean error over a 3 m transmission. The reported 187 ms rise-time of this method of force transmission demonstrates potential for better tracking performance than currently achieved with hydraulic and pneumatic linear actuation experiments [31]. This method of transmission is beneficial to MRI because it can be produced out materials which do not generate or transmit RF signals to the MRI machine. However, it is not limited to use in MRI and may also be more suitable fluidic systems in low force applications which would benefit from enhanced stiffness or accuracy and do not require force amplification. Due to the stiffness of SMFT, no brakes are necessary when used with a self-braked motor such as stepper motors or USM. The stepper motors used in these experiments were all controlled using a hybrid feedforward and feedback control system which was implemented on an FGPA. Although non-linear control methods were reviewed, it was determined that standard PID control was sufficient given the feedback information available in these systems. The FPGA implementation provided enhanced performance and sampling time over processor based approaches, which resulted in a noticeable reduce in sensitivity of tuning parameters and excellent tracking results. Observed maximum tracking error was only three times greater than the precision of the motor itself during the tracking of a sigmoid function and a chirp signal.

Research in MRI compatible robotics typically present a high-level solution to achieving desired actuation requirements inside of the highly constrained MRI environment by use and integration of many commercially available off-the-shelf

components such as actuators, controllers, and filters. This particular work, however, has explored lower level research into all of the interdisciplinary components which come together to form an MRI compatible design. The in-depth study of each of the interdisciplinary core technologies presented in this work provided broader insight, yet specific solutions required to achieve results through a true engineering process. The core technologies presented within have each shown merit of their own, and the results will be disseminated to their appropriate fields, with the additional value of the development of a high performance robotic system from the combination of these technologies. Future work will consist of perfection of the filtering methods discussed within to eliminate the remaining artifacts to enable the completion of the MRI compatible positioning robot. However, the most notable future outcomes and impact of this work will come from the future development, refinement, and commercial application of the novel SMFT technology.

9. Works Cited

[1] J. E. A. Wickham, "The New Surgery," *British Medical Journal (Clinical Research Edition)*, vol. 295, pp. 1581-1582, 1987.

[2] P. C. McAfee, S. R. Garfin, W. B. Rodgers, R. T. Allen, F. Phillips, and C. Kim, "An Attempt at Clinically Defining and Assessing Minimally Invasive Surgery Compared with Traditional “Open” Spinal Surgery," *SAS Journal*, vol. 5, pp. 125-130, 2011.

[3] G. Perigli, C. Cortesini, E. Qirici, D. Boni, and F. Cianchi, "Clinical Benefits of Minimally Invasive Techniques in Thyroid Surgery," *World Journal of Surgery*, vol. 32, pp. 45-50, 2008.

[4] C. A. Grimbergen, J. E. N. Jaspers, J. L. Herder, and H. G. Stassen, "Development of Laparoscopic Instruments," *Minimally Invasive Therapy & Allied Technologies*, vol. 10, pp. 145-154, 2001.

[5] K. T. den Boer, J. L. Herder, W. Sjoerdsma, D. W. Meijer, D. J. Gouma, and H. G. Stassen, "Sensitivity of Laparoscopic Dissectors," *Surgical Endoscopy*, vol. 13, pp. 869-873, 1999.

[6] D. P. Perrin, N. V. Vasilyev, P. Novotny, J. Stoll, R. D. Howe, P. E. Dupont, I. S. Salgo, and P. J. del Nido, "Image Guided Surgical Interventions," *Current Problems in Surgery*, vol. 46, pp. 730-766, 2009.

[7] K. Ponnusamy, C. Mohr, and M. J. Curet, "Clinical Outcomes with Robotic Surgery," *Current Problems in Surgery*, vol. 48, pp. 577-656, 2011.

[8] D. B. Camarillo, T. M. Krummel, and J. K. Salisbury Jr, "Robotic Technology in Surgery: Past, Present, and Future," *The American Journal of Surgery*, vol. 188, pp. 2-15, 2004.

[9] P. Kazanzides, J. Zuhars, B. Mittelstadt, B. Williamson, P. Cain, F. Smith, L. Rose, and B. Musits, "Architecture of a Surgical Robot," presented at Systems, Man and Cybernetics, 1992., IEEE International Conference on, 1992.

[10] G. R. Sutherland, P. B. McBeth, and D. F. Louw, "Neuroarm: An Mr Compatible Robot for Microsurgery," *International Congress Series*, vol. 1256, pp. 504-508, 2003.

[11] T. E. Ahlering, D. Woo, L. Eichel, D. I. Lee, R. Edwards, and D. W. Skarecky, "Robot-Assisted Versus Open Radical Prostatectomy: A Comparison of One Surgeon's Outcomes," *Urology*, vol. 63, pp. 819-822, 2004.

[12] M. K. Oehler, "Robot-Assisted Surgery in Gynaecology," *Australian & New Zealand Journal of Obstetrics & Gynaecology*, vol. 49, pp. 124-129, 2009.

[13] A. Al-Bassam, "Robotic-Assisted Surgery in Children: Advantages and Limitations," *Journal of Robotic Surgery*, vol. 4, pp. 19-22, 2010.

[14] H. National Institutes of, *Magnetic Resonance Imaging*. [Bethesda, MD: U.S. Dept. of Health and Human Services, Public Health Service, National Institutes of Health, 1988.

[15] S. Maria Filomena, "Basic Physics of Mr Signal and Image Generation," in *Advanced Image Processing in Magnetic Resonance Imaging*, *Signal Processing and Communications*: CRC Press, 2005, pp. 3-37.

[16] N. V. Tsekos, E. Christoforou, and A. Ozcan, "A General-Purpose Mr-Compatible Robotic System," *Engineering in Medicine and Biology Magazine, IEEE*, vol. 27, pp. 51-58, 2008.

[17] F. A. Jolesz, "Invited. Interventional and Intraoperative Mri: A General Overview of the Field," *Journal of Magnetic Resonance Imaging*, vol. 8, pp. 3-7, 1998.

[18] N. V. Tsekos, A. Khanicheh, E. Christoforou, and C. Mavroidis, "Magnetic Resonance–Compatible Robotic and Mechatronics Systems for Image-Guided Interventions and Rehabilitation: A Review Study," *Annual Review of Biomedical Engineering*, vol. 9, pp. 351-387, 2007.

[19] P. R. Eby and C. Lehman, "Mri-Guided Breast Interventions," *Seminars in Ultrasound, CT, and MRI*, vol. 27, pp. 339-350, 2006.

[20] X. Yang and E. Atalar, "Mri-Guided Gene Therapy," *FEBS Letters*, vol. 580, pp. 2958-2961, 2006.

[21] K. J. Mortele, K. Tuncali, V. Cantisani, S. Shankar, E. vanSonnenberg, C. Tempany, and S. G. Silverman, "Mri-Guided Abdominal Intervention," *Abdominal Imaging*, vol. 28, pp. 756-774, 2003.

[22] V. Seifert, M. Zimmermann, C. Trantakis, H. E. Vitzthum, K. Kühnel, A. Raabe, F. Bootz, J. P. Schneider, F. Schmidt, and J. Dietrich, "Open Mri-Guided Neurosurgery," *Acta Neurochirurgica*, vol. 141, pp. 455-464, 1999.

[23] E. R. McVeigh, M. A. Guttman, R. J. Lederman, M. Li, O. Kocaturk, T. Hunt, S. Kozlov, and K. A. Horvath, "Real-Time Interactive Mri-Guided Cardiac Surgery: Aortic Valve Replacement Using a Direct Apical Approach," *Magnetic Resonance in Medicine*, vol. 56, pp. 958-964, 2006.

[24] C. Keroglou, I. Seimenis, N. V. Tsekos, C. Pitris, E. Eracleous, and E. G. Christoforou, "Consideration of Geometric Constraints Regarding Mr-Compatible Interventional Robotic Devices," presented at Biomedical Robotics and Biomechatronics (BioRob), 2010 3rd IEEE RAS and EMBS International Conference on, 2010.

[25] T. C. Cosmus and M. Parizh, "Advances in Whole-Body Mri Magnets," *Applied Superconductivity, IEEE Transactions on*, vol. 21, pp. 2104-2109, 2011.

[26] C. Rickers, R. T. Seethamraju, M. Jerosch-Herold, and N. M. Wilke, "Magnetic Resonance Imaging Guided Cardiovascular Interventions in Congenital Heart Diseases," *Journal of Interventional Cardiology*, vol. 16, pp. 143-147, 2003.

[27] R. Gassert, E. Burdet, and K. Chinzei, "Mri-Compatible Robotics," *Engineering in Medicine and Biology Magazine, IEEE*, vol. 27, pp. 12-14, 2008.

[28] R. Gassert, A. Yamamoto, D. Chapuis, L. Dovat, H. Bleuler, and E. Burdet, "Actuation Methods for Applications in Mr Environments," *Concepts in Magnetic Resonance Part B: Magnetic Resonance Engineering*, vol. 29B, pp. 191-209, 2006.

[29] M. F. Dempsey, B. Condon, and D. M. Hadley, "Mri Safety Review," *Seminars in Ultrasound, CT, and MRI*, vol. 23, pp. 392-401, 2002.

[30] R. Gassert, R. Moser, E. Burdet, and H. Bleuler, "Mri/Fmri-Compatible Robotic System with Force Feedback for Interaction with Human Motion," *Mechatronics, IEEE/ASME Transactions on*, vol. 11, pp. 216-224, 2006.

[31] Y. Ningbo, C. Hollnagel, A. Blickenstorfer, S. S. Kollias, and R. Riener, "Comparison of Mri-Compatible Mechatronic Systems with Hydrodynamic and

Pneumatic Actuation," *Mechatronics, IEEE/ASME Transactions on*, vol. 13, pp. 268-277, 2008.

[32] G. S. Fischer, I. Iordachita, C. Csoma, J. Tokuda, S. P. DiMaio, C. M. Tempany, N. Hata, and G. Fichtinger, "Mri-Compatible Pneumatic Robot for Transperineal Prostate Needle Placement," *Mechatronics, IEEE/ASME Transactions on*, vol. 13, pp. 295-305, 2008.

[33] N. Zemiti, I. Bricault, C. Fouard, B. Sanchez, and P. Cinquin, "Lpr: A Ct and Mr-Compatible Puncture Robot to Enhance Accuracy and Safety of Image-Guided Interventions," *Mechatronics, IEEE/ASME Transactions on*, vol. 13, pp. 306-315, 2008.

[34] D. Stoianovici, A. Patriciu, D. Petrisor, D. Mazilu, and L. Kavoussi, "A New Type of Motor: Pneumatic Step Motor," *Mechatronics, IEEE/ASME Transactions on*, vol. 12, pp. 98-106, 2007.

[35] G. R. Sutherland, I. Latour, and A. D. Greer, "Integrating an Image-Guided Robot with Intraoperative Mri," *Engineering in Medicine and Biology Magazine, IEEE*, vol. 27, pp. 59-65, 2008.

[36] G. Fischer, A. Krieger, I. Iordachita, C. Csoma, L. Whitcomb, and G. Fichtinger, "Mri Compatibility of Robot Actuation Techniques – a Comparative Study

Medical Image Computing and Computer-Assisted Intervention – Miccai 2008," vol. 5242, *Lecture Notes in Computer Science*, D. Metaxas, L. Axel, G. Fichtinger, and G. Székely, Eds.: Springer Berlin / Heidelberg, 2008, pp. 509-517.

[37] T. Suzuki, L. Hongen, E. Kobayashi, and I. Sakuma, "Ultrasonic Motor Driving Method for Emi-Free Image in Mr Image-Guided Surgical Robotic System,"

presented at Intelligent Robots and Systems, 2007. IROS 2007. IEEE/RSJ International Conference on, 2007.

[38] A. Krieger, I. Iordachita, S. Sang-Eun, N. B. Cho, P. Guion, G. Fichtinger, and L. L. Whitcomb, "Development and Preliminary Evaluation of an Actuated Mri-Compatible Robotic Device for Mri-Guided Prostate Intervention," presented at Robotics and Automation (ICRA), 2010 IEEE International Conference on, 2010.

[39] H. Elhawary, A. Zivanovic, M. Rea, B. Davies, C. Besant, D. McRobbie, N. de Souza, I. Young, and M. Lampérth, "The Feasibility of Mr-Image Guided Prostate Biopsy Using Piezoceramic Motors inside or near to the Magnet Isocentre

Medical Image Computing and Computer-Assisted Intervention – Miccai 2006," vol. 4190, *Lecture Notes in Computer Science*, R. Larsen, M. Nielsen, and J. Sporring, Eds.: Springer Berlin / Heidelberg, 2006, pp. 519-526.

[40] A. A. Goldenberg, J. Trachtenberg, W. Kucharczyk, Y. Yang, M. Haider, L. Ma, R. Weersink, and C. Raoufi, "Robotic System for Closed-Bore Mri-Guided Prostatic Interventions," *Mechatronics, IEEE/ASME Transactions on*, vol. 13, pp. 374-379, 2008.

[41] G. S. Fischer, G. Cole, and S. Hao, "Approaches to Creating and Controlling Motion in Mri," presented at Engineering in Medicine and Biology Society,EMBC, 2011 Annual International Conference of the IEEE, 2011.

[42] J.-S. Plante, K. Tadakuma, L. M. DeVita, D. F. Kacher, J. R. Roebuck, S. P. DiMaio, F. A. Jolesz, and S. Dubowsky, "An Mri-Compatible Needle Manipulator Concept Based on Elastically Averaged Dielectric Elastomer

Actuators for Prostate Cancer Treatment: An Accuracy and Mr-Compatibility Evaluation in Phantoms," *Journal of Medical Devices*, vol. 3, pp. 031005, 2009.

[43] A. Yamamoto, K. Ichiyanagi, T. Higuchi, H. Imamizu, R. Gassert, M. Ingold, L. Sache, and H. Bleuler, "Evaluation of Mr-Compatibility of Electrostatic Linear Motor," presented at Robotics and Automation, 2005. ICRA 2005. Proceedings of the 2005 IEEE International Conference on, 2005.

[44] J. Vogan, A. Wingert, J. S. Plante, S. Dubowsky, M. Hafez, D. Kacher, and F. Jolesz, "Manipulation in Mri Devices Using Electrostrictive Polymer Actuators: With an Application to Reconfigurable Imaging Coils," presented at Robotics and Automation, 2004. Proceedings. ICRA '04. 2004 IEEE International Conference on, 2004.

[45] W. W. Roeck, S.-H. Ha, S. Farmaka, and O. Nalcioglu, "A Variable Torque Motor Compatible with Magnetic Resonance Imaging," *Review of Scientific Instruments*, vol. 80, pp. 046108, 2009.

[46] N. von Sternberg, Y. Hedayati, E. Yeniaras, E. Christoforou, and N. V. Tsekos, "Design of an Actuated Phantom to Mimic the Motion of Cardiac Landmarks for the Study of Image-Guided Intracardiac Interventions," presented at Robotics and Biomimetics (ROBIO), 2010 IEEE International Conference on, 2010.

[47] K. Chinzei, N. Hata, F. A. Jolesz, and R. Kikinis, "Surgical Assist Robot for the Active Navigation in the Intraoperative Mri: Hardware Design Issues," presented at Intelligent Robots and Systems, 2000. (IROS 2000). Proceedings. 2000 IEEE/RSJ International Conference on, 2000.

[48] A. Melzer, B. Gutmann, T. Remmele, R. Wolf, A. Lukoscheck, M. Bock, H. Bardenheuer, and H. Fischer, "Innomotion for Percutaneous Image-Guided Interventions," *Engineering in Medicine and Biology Magazine, IEEE*, vol. 27, pp. 66-73, 2008.

[49] L. Ming, A. Kapoor, D. Mazilu, and K. A. Horvath, "Pneumatic Actuated Robotic Assistant System for Aortic Valve Replacement under Mri Guidance," *Biomedical Engineering, IEEE Transactions on*, vol. 58, pp. 443-451, 2011.

[50] A. Kapoor, B. Wood, D. Mazilu, K. A. Horvath, and L. Ming, "Mri-Compatible Hands-on Cooperative Control of a Pneumatically Actuated Robot," presented at Robotics and Automation, 2009. ICRA '09. IEEE International Conference on, 2009.

[51] I. Bricault, N. Zemiti, E. Jouniaux, C. Fouard, E. Taillant, F. Dorandeu, and P. Cinquin, "Light Puncture Robot for Ct and Mri Interventions," *Engineering in Medicine and Biology Magazine, IEEE*, vol. 27, pp. 42-50, 2008.

[52] A. Krieger, R. C. Susil, C. Menard, J. A. Coleman, G. Fichtinger, E. Atalar, and L. L. Whitcomb, "Design of a Novel Mri Compatible Manipulator for Image Guided Prostate Interventions," *Biomedical Engineering, IEEE Transactions on*, vol. 52, pp. 306-313, 2005.

[53] A. Krieger, I. I. Iordachita, P. Guion, A. K. Singh, A. Kaushal, C. Menard, P. A. Pinto, K. Camphausen, G. Fichtinger, and L. L. Whitcomb, "An Mri-Compatible Robotic System with Hybrid Tracking for Mri-Guided Prostate Intervention," *Biomedical Engineering, IEEE Transactions on*, vol. 58, pp. 3049-3060, 2011.

[54] A. Patriciu, D. Petrisor, M. Muntener, D. Mazilu, M. Schar, and D. Stoianovici, "Automatic Brachytherapy Seed Placement under Mri Guidance," *Biomedical Engineering, IEEE Transactions on*, vol. 54, pp. 1499-1506, 2007.

[55] A. Bellini, C. Concari, G. Franceschini, and A. Toscani, "Mixed-Mode Pwm for High-Performance Stepping Motors," *Industrial Electronics, IEEE Transactions on*, vol. 54, pp. 3167-3177, 2007.

[56] C. K. Taft and R. G. Gauthier, "Stepping Motor Failure Model," *Industrial Electronics and Control Instrumentation, IEEE Transactions on*, vol. IECI-22, pp. 375-385, 1975.

[57] M. Bodson, J. S. Sato, and S. R. Silver, "Spontaneous Speed Reversals in Stepper Motors," *Control Systems Technology, IEEE Transactions on*, vol. 14, pp. 369-373, 2006.

[58] K. W. H. Tsui and N. C. Cheung, "Novel Modeling and Damping Technique for Hybrid Stepper Motor," presented at Industrial Electronics and Applications, 2007. ICIEA 2007. 2nd IEEE Conference on, 2007.

[59] M. Bodson, J. N. Chiasson, R. T. Novotnak, and R. B. Rekowski, "High-Performance Nonlinear Feedback Control of a Permanent Magnet Stepper Motor," *Control Systems Technology, IEEE Transactions on*, vol. 1, pp. 5-14, 1993.

[60] M. Defoort, F. Nollet, T. Floquet, and W. Perruquetti, "A Third-Order Sliding-Mode Controller for a Stepper Motor," *Industrial Electronics, IEEE Transactions on*, vol. 56, pp. 3337-3346, 2009.

[61] S. A. Schweid, J. E. McInroy, and R. M. Lofthus, "Closed Loop Low-Velocity Regulation of Hybrid Stepping Motors Amidst Torque Disturbances," *Industrial Electronics, IEEE Transactions on*, vol. 42, pp. 316-324, 1995.

[62] M. Zribi and J. Chiasson, "Position Control of a Pm Stepper Motor by Exact Linearization," *Automatic Control, IEEE Transactions on*, vol. 36, pp. 620-625, 1991.

[63] Y. Anzai, S. Nishikata, and F. Tatsuta, "Studies on a Sensorless Initial Rotor Position Estimating Method for Hybrid Stepping Motors," presented at Electrical Machines and Systems, 2009. ICEMS 2009. International Conference on, 2009.

[64] M. Boussak, "Implementation and Experimental Investigation of Sensorless Speed Control with Initial Rotor Position Estimation for Interior Permanent Magnet Synchronous Motor Drive," *Power Electronics, IEEE Transactions on*, vol. 20, pp. 1413-1422, 2005.

[65] N. Bianchi, S. Bolognani, J. Ji-Hoon, and S. Seung-Ki, "Comparison of Pm Motor Structures and Sensorless Control Techniques for Zero-Speed Rotor Position Detection," *Power Electronics, IEEE Transactions on*, vol. 22, pp. 2466-2475, 2007.

[66] M. Bendjedia, Y. Ait-Amirat, B. Walther, and A. Berthon, "Dsp Implementation of Rotor Position Detection Method for Hybrid Stepper Motors," presented at Power Electronics and Motion Control Conference, 2006. IPEMC 2006. CES/IEEE 5th International, 2006.

[67] K. Wonhee, S. Donghoon, and C. Chung Choo, "Microstepping Using a Disturbance Observer and a Variable Structure Controller for Permanent-Magnet

Stepper Motors," *Industrial Electronics, IEEE Transactions on*, vol. 60, pp. 2689-2699, 2013.

[68] H. Melkote and F. Khorrami, "Nonlinear Output Feedback Control for Stepper Motors: A Robust Adaptive Approach," presented at Control Applications, 1999. Proceedings of the 1999 IEEE International Conference on, 1999.

[69] P. Krishnamurthy and F. Khorrami, "Voltage-Fed Permanent-Magnet Stepper Motor Control Via Position-Only Feedback," *Control Theory and Applications, IEE Proceedings* -, vol. 151, pp. 499-510, 2004.

[70] M. Zribi, H. Sira-Ramirez, and A. Ngai, "Static and Dynamic Sliding Mode Control Schemes for a Permanent Magnet Stepper Motor," *International Journal of Control*, vol. 74, pp. 103-117, 2001.

[71] F. Nollet, T. Floquet, and W. Perruquetti, "Observer-Based Second Order Sliding Mode Control Laws for Stepper Motors," *Control Engineering Practice*, vol. 16, pp. 429-443, 2008.

[72] A. Rubaai and R. Kotaru, "Adaptation Learning Control Scheme for a High-Performance Permanent-Magnet Stepper Motor Using Online Random Training of Neural Networks," *Industry Applications, IEEE Transactions on*, vol. 37, pp. 495-502, 2001.

[73] T. Boltz, W. Pavlicek, R. Paden, M. Renno, A. Jensen, and M. Akay, "An Anthropomorphic Beating Heart Phantom for Cardiac X-Ray Ct Imaging Evaluation," *Journal of Applied Clinical Medical Physics*, vol. 11, 2009.

[74] M. Li, D. Mazilu, and K. A. Horvath, "Robotic System for Transapical Aortic Valve Replacement with Mri Guidance," *Med Image Comput Comput Assist Interv*, vol. 11, pp. 476-84, 2008.

[75] E. Yeniaras, J. Lamaury, N. V. Navkar, D. J. Shah, K. Chin, D. Zhigang, and N. V. Tsekos, "Magnetic Resonance Based Control of a Robotic Manipulator for Interventions in the Beating Heart," presented at Robotics and Automation (ICRA), 2011 IEEE International Conference on, 2011.

[76] E. Yeniaras, N. Navkar, M. A. Syed, and N. V. Tsekos, "A Computational System for Performing Robot-Assisted Cardiac Surgeries with Mri Guidance," presented at Proceedings of the 15th International Transformative Systems Conference, Dallas,USA, 2010.

[77] E. Yeniaras, J. Lamaury, Z. Deng, and N. V. Tsekos, "Towards a New Cyber-Physical System for Mri-Guided and Robot-Assisted Cardiac Procedures," presented at Proceedings of 10th IEEE International Conference on Information Technology and Applications in Biomedicine (ITAB), Corfu, Greece, 2010.

[78] N. V. Navkar, E. Yeniaras, D. J. Shah, N. V. Tsekos, and D. Zhigang, "Extracting Geometric Features of Aortic Valve Annulus Motion from Dynamic Mri for Guiding Interventions," presented at Biomedical Imaging: From Nano to Macro, 2011 IEEE International Symposium on, 2011.

[79] N. V. Navkar, D. Zhigang, D. J. Shah, and N. V. Tsekos, "A Framework for Integrating Real-Time Mri with Robot Control: Application to Simulated Transapical Cardiac Interventions," *Biomedical Engineering, IEEE Transactions on*, vol. 60, pp. 1023-1033, 2013.

[80] N. C. von Sternberg, Y. S. Hedayati, H. M. Zaid, E. Yeniaras, E. Christoforou, and N. V. Tsekos, "An Actuated Phantom for Developing and Studying Mri-Guided Interventions in Dynamic Environments," presented at Biomedical Robotics and Biomechatronics (BioRob), 2012 4th IEEE RAS & EMBS International Conference on, 2012.

[81] E. Yeniaras, Z. Deng, M. A. Syed, M. G. Davies, and N. V. Tsekos, "A Novel Virtual Reality Environment for Preoperative Planning and Simulation of Image Guided Intracardiac Surgeries with Robotic Manipulators," in *MMVR*, vol. 163, J. D. Westwood, S. W. Westwood, L. Felländer-Tsai, R. S. Haluck, H. M. Hoffman, R. A. Robb, S. Senger, and K. G. Vosburgh, Eds.: IOS Press, 2011, pp. 716-722.

[82] S. E. Goodnick, "Active Damping Keeps Steppers Spinning," *Machine Design*, vol. 67, pp. 76-80, 1995.

[83] T.-C. Chen and Y.-C. Su, "High Performance Algorithm Realization on Fpga for Stepper Motor Controller," 2008.

[84] K. Wonhee and C. Chung Choo, "Novel Position Detection Method for Permanent Magnet Stepper Motors Using Only Current Feedback," *Magnetics, IEEE Transactions on*, vol. 47, pp. 3590-3593, 2011.

[85] K. Wonhee, S. Donghoon, and C. Chung Choo, "Microstepping with Nonlinear Torque Modulation for Permanent Magnet Stepper Motors," *Control Systems Technology, IEEE Transactions on*, vol. 21, pp. 1971-1979, 2013.

[86] R. Gassert, E. Burdet, and K. Chinzei, "Opportunities and Challenges in Mr-Compatible Robotics," *Engineering in Medicine and Biology Magazine, IEEE*, vol. 27, pp. 15-22, 2008.

[87] G. Ganesh, R. Gassert, E. Burdet, and H. Bleuler, "Dynamics and Control of an Mri Compatible Master-Slave System with Hydrostatic Transmission," presented at Robotics and Automation, 2004. Proceedings. ICRA '04. 2004 IEEE International Conference on, 2004.

[88] M. Hara, J. Duenas, T. Kober, D. Chapuis, O. Lambercy, H. Bleuler, and R. Gassert, "Design and Compatibility of a High-Performance Actuation System for Fmri-Based Neuroscience Studies," presented at Intelligent Robots and Systems (IROS), 2010 IEEE/RSJ International Conference on, 2010.

[89] M. Oura, Y. Kobayashi, J. Okamoto, and M. G. Fujie, "Development of Mri Compatible Versatile Manipulator for Minimally Invasive Surgery," presented at Biomedical Robotics and Biomechatronics, 2006. BioRob 2006. The First IEEE/RAS-EMBS International Conference on, 2006.

[90] N. V. Tsekos, J. Shudy, E. Yacoub, P. V. Tsekos, and I. G. Koutlas, "Development of a Robotic Device for Mri-Guided Interventions in the Breast," presented at Bioinformatics and Bioengineering Conference, 2001. Proceedings of the IEEE 2nd International Symposium on, 2001.

[91] B. T. Larson, N. V. Tsekos, and A. G. Erdman, "A Robotic Device for Minimally Invasive Breast Interventions with Real-Time Mri Guidance," presented at Bioinformatics and Bioengineering, 2003. Proceedings. Third IEEE Symposium on, 2003.

[92] B. T. Larson, A. G. Erdman, N. V. Tsekos, E. Yacoub, P. V. Tsekos, and I. G. Koutlas, "Design of an Mri-Compatible Robotic Stereotactic Device for

Minimally Invasive Interventions in the Breast," *J Biomech Eng*, vol. 126, pp. 458-65, 2004.

[93] N. V. Tsekos, A. Ozcan, and E. Christoforou, "A Prototype Manipulator for Magnetic Resonance-Guided Interventions inside Standard Cylindrical Magnetic Resonance Imaging Scanners," *J Biomech Eng*, vol. 127, pp. 972-80, 2005.

[94] E. G. Christoforou, A. Ozcan, and N. V. Tsekos, "Robotic Arm for Magnetic Resonance Imaging Guided Interventions," presented at Biomedical Robotics and Biomechatronics, 2006. BioRob 2006. The First IEEE/RAS-EMBS International Conference on, 2006.

[95] E. G. Christoforou and N. V. Tsekos, "Robotic Manipulators with Remotely-Actuated Joints: Implementation Using Drive-Shafts and U-Joints," presented at Robotics and Automation, 2006. ICRA 2006. Proceedings 2006 IEEE International Conference on, 2006.

[96] E. Christoforou, E. Akbudak, A. Ozcan, M. Karanikolas, and N. V. Tsekos, "Performance of Interventions with Manipulator-Driven Real-Time Mr Guidance: Implementation and Initial in Vitro Tests," *Magn Reson Imaging*, vol. 25, pp. 69-77, 2007.

[97] A. E. Sonmez, A. Ozcan, W. M. Spees, and T. Nikolaos, "Robot-Facilitated Scanning and Co-Registration of Multi-Modal and Multi-Level Sensing: Demonstration with Magnetic Resonance Imaging and Spectroscopy," presented at IEEE International Conference on Robotics and Automation, Shanghai, China, 2011.

[98] A. E. Sonmez, A. G. Webb, W. M. Spees, A. Ozcan, and N. V. Tsekos, "A System for Endoscopic Mechanically Scanned Localized Proton Mr and Light-Induced Fluorescence Emission Spectroscopies," *J Magn Reson*, vol. 222, pp. 16-25, 2012.

[99] S. Hao, M. Zervas, G. A. Cole, C. Furlong, and G. S. Fischer, "Real-Time Mri-Guided Needle Placement Robot with Integrated Fiber Optic Force Sensing," presented at Robotics and Automation (ICRA), 2011 IEEE International Conference on, 2011.

[100] Y. Bo, U. X. Tan, A. B. McMillan, R. Gullapalli, and J. P. Desai, "Design and Control of a 1-Dof Mri-Compatible Pneumatically Actuated Robot with Long Transmission Lines," *Mechatronics, IEEE/ASME Transactions on*, vol. 16, pp. 1040-1048, 2011.

[101] S. Sang-Eun, N. B. Cho, G. Fischer, N. Hata, C. Tempany, G. Fichtinger, and I. Iordachita, "Development of a Pneumatic Robot for Mri-Guided Transperineal Prostate Biopsy and Brachytherapy: New Approaches," presented at Robotics and Automation (ICRA), 2010 IEEE International Conference on, 2010.

[102] B. Vigaru, D. Petrisor, A. Patriciu, D. Mazilu, and D. Stoianovici, "Mr Compatible Actuation for Medical Instrumentation," presented at Automation, Quality and Testing, Robotics, 2008. AQTR 2008. IEEE International Conference on, 2008.

[103] R. J. Dickinson and R. I. Kitney, "Miniature Ultrasonic Probe Construction for Minimal Access Surgery," *Phys Med Biol*, vol. 49, pp. 3527-38, 2004.

[104] K. A. Horvath, M. Li, D. Mazilu, M. A. Guttman, and E. R. McVeigh, "Real-Time Magnetic Resonance Imaging Guidance for Cardiovascular Procedures," *Semin Thorac Cardiovasc Surg*, vol. 19, pp. 330-5, 2007.

[105] M. Muntener, A. Patriciu, D. Petrisor, D. Mazilu, H. Bagga, L. Kavoussi, K. Cleary, and D. Stoianovici, "Magnetic Resonance Imaging Compatible Robotic System for Fully Automated Brachytherapy Seed Placement," *Urology*, vol. 68, pp. 1313-7, 2006.

[106] G. R. Sutherland, I. Latour, and A. D. Greer, "Integrating an Image-Guided Robot with Intraoperative Mri: A Review of the Design and Construction of Neuroarm," *IEEE Eng Med Biol Mag*, vol. 27, pp. 59-65, 2008.

[107] N. V. Tsekos, E. Christoforou, and A. Ozcan, "A General-Purpose Mr-Compatible Robotic System: Implementation and Image Guidance for Performing Minimally Invasive Interventions," *IEEE Eng Med Biol Mag*, vol. 27, pp. 51-8, 2008.

[108] M. Adam Khan and A. Senthil Kumar, "Machinability of Glass Fibre Reinforced Plastic (Gfrp) Composite Using Alumina-Based Ceramic Cutting Tools," *Journal of Manufacturing Processes*, vol. 13, pp. 67-73, 2011.

[109] G. Santhanakrishnan, R. Krishnamurthy, and S. K. Malhotra, "High Speed Steel Tool Wear Studies in Machining of Glass-Fibre-Reinforced Plastics," *Wear*, vol. 132, pp. 327-336, 1989.

[110] M. L. Lipton, *Totally Accessible Mri: A User's Guide to Principles, Technology, and Applications*: Springer, 2010.

[111] S. C. Bushong, *Magnetic Resonance Imaging : Physical and Biological Principles*. St. Louis, Mo.: Mosby, 2003.

[112] Siemens, "Room Planning Guide," 2005.

[113] J. T. Vaughan and J. R. Griffiths, *Rf Coils for Mri*: Wiley, 2012.

[114] J. H. Heinbockel, *Mathematical Methods for Partial Differential Equations*. Victoria, B.C.: Trafford, 2003.

[115] J. D. Lenk, *Simplified Design of Filter Circuits*: Newnes, 1999.

[116] F. Kuo, *Network Analysis and Synthesis, 2nd Ed*: Wiley India Pvt. Limited, 2006.

[117] J. Laskar, S. Chakraborty, A. V. Pham, and M. M. Tantzeris, *Advanced Integrated Communication Microsystems*: Wiley, 2009.

[118] NEMA, "Determination of Signal-to-Noise Ratio (Snr) in Diagnostic Magnetic Resonance Imaging," vol. MS 1-2008. USA: National Electrical Manufacturers Association, 2008

[119] D. Setters, "Three Multileaf Collimators [Press Release]," Maxon Precision Motors, 2013, pp. 1-3.